UiT
THE ARCTIC
UNIVERSITY
OF NORWAY

Faculty of Science and Technology
Department of Geosciences

Structural assessment and characterization of the unstable rock slopes at Mellomfjellet, Nordreisa

—

Bernt Kristian Flekstad Vik

GEO-3900 Master's thesis in Geology

May 2019

UNIVERSITY OF TROMSØ

Abstract

The aim of this study has been to structurally assess and characterize the unstable rock slopes (URS) at Mellomfjellet using an interdisciplinary approach of structural geological analysis, geomorphological mapping, photogrammetry and remote sensing. The URS are located on the west-facing slopes of Mellomfjellet and display a dramatic geomorphology with deep ice filled fractures and clearly displaced blocks in the glacially eroded Reisadalen in Northern Troms.

Geological mapping of Mellomfjellet showed that the bedrock consists predominantly of amphibolite. The area was divided into two domains (MF1 and MF2) where MF1 comprised of a foliation (strike/dip; 169°/15°±18.9°) and three joint sets: J1 (029°/72°±16. 3°), J2 (286°/83°±21.8°) and J3 (075°/67°±12.3°). MF2 comprised of a foliation (183°/11°±14.3°) and three joint sets: J1 (022°/82°±14.7°), J2 (108°/88°±15.3°) J3 and (071°/52°±12.7°). Joint set J3 was for both domains found in relation to two E – W-trending morphological depressions. The mapped joint sets correlated well with joint sets determined from drone photogrammetry, and InSAR displacement showed structural trends, delineated by mapped bedrock structures and morphological elements.

The kinematic analysis from MF1 showed that flexural toppling along J1 was a partly feasible failure mechanism. Planar failure along the foliation was feasible for some of the foliation and therefore a bi-planar compound slide comprising of J1 and the foliation is proposed as the main failure mechanism. At MF2 flexural toppling along J1 is the main failure mechanism and slide topple is proposed, as there is feasibility for planar sliding along some of the foliation. The mapped bedrock structures align with regional structural geological trends and are interpreted to govern the failure mechanisms and delineation of the URS at Mellomfjellet.

Worst-case scenarios for each domain where delineated based on geomorphological features in order to assess consequences connected to the URS. The scenarios ranged from 1 to 3 Mm3 in volume and the run-out modeling showed that no settlement was reached and therefore the risk is low for both scenarios.

Acknowledgements

This thesis concludes my Master of Science degree in geology at the Department of Geosciences at UiT Arctic University of Norway. Dr. Louise Vick (UiT) and Dr. Martina Böhme (NGU) supervised the thesis.

First, I want to thank my supervisor Louise Vick for the help and guidance in this thesis. I have appreciated your constructive and honest feedback and the interest you have shown for the project. Especially, I want to thank you for teaching us engineering geology and that you provided a chance for an internship abroad.

Secondly, I want to thank my co-supervisor Martina Böhme for valuable help during the process. She guided through the run-out modelling and gave valuable insights in field of URS.

Especially thanks to fellow student Gaute Sikveland for the field work during fall and for keeping up the spirit during the year. In addition, I would like to thank my family for supporting me.

Tromsø, May 2019

Bernt Kristian Flekstad Vik

Table of Contents

1 Introduction

1.1 Background

Norway is a country of alpine mountains and deep fjords and valleys. The alpine nature of the topography, carved out by glaciers, makes the landscape prone to geohazards such as landslides. Landslides pose a risk to lives and infrastructure. Over the last century, several catastrophic rock slope failures have occurred in Norway, causing serious damage and loss of life (Furseth, 2006). These events highlight the importance of increasing the knowledge of landslides, to be able mitigate and protect society from the consequences.

In Troms more than >130 rock slope instabilities are mapped, several which pose a serious hazard for society (NGU, 2018). The arctic conditions are well suited for studying unstable rock slopes (URS) as the lack of vegetation exposes complex surface morphologies. The landslide database in Troms includes a wide range of observed deformation styles (NGU, 2018). By combining structural geology, geomorphology, engineering geology and remote sensing to characterize a slope, the hazard they pose can be assessed (Jaboyedoff et al., 2011). Detailed landslide mapping of the unstable areas provides insights into failure mechanisms and scenarios.

This thesis is part of a Geological Survey of Norway (NGU) mapping project, which aims to systematically classify both hazard and risk for all URS in Troms. URS are being mapped, and run-out areas, possible tsunamis and other secondary effects estimated. A consequence analysis for each unstable rock slope is or has been undertaken for the purposes of hazard and risk classification (Hermanns et al., 2012). If necessary, due to high risk, URS will be periodically or permanently monitored.

1.2 Thesis aim

The aim of this master thesis is to structurally assess and characterize the URS at Mellomfjellet. An interdisciplinary approach with the aid of structural geology analysis, geomorphological mapping, photogrammetry and remote sensing methods will be used. A hazard assessment that includes simple run-out analyses of different failure scenarios is performed.

The main workflow includes the following steps:

- Map the bedrock lithology and discontinuities as well as geomorphology and drainage of the URS.
- Execute a structural analysis to find the spatial variation in the mapped discontinuities to divide into structural domains. Perform a kinematic analysis to evaluate possible failure mechanisms.
- Use interferometric synthetic aperture radar (InSAR) for displacement assessment.
- Unmanned aerial vehicle photo capture of the northern back-scarp for further detailed structural assessment of discontinuities in Coltop3D.
- Comparing local structure to regional trends for a broader understanding of the structural geology.
- Estimation of volumes using “sloping local base level” (SLBL) and run-out analyses using Flow-R software for the different scenarios.
- Hazard assessment using the NGU hazard and risk classification.
- Discuss movement mechanisms and possible driving forces of the unstable area.

2 Study area

2.1 Site location

Mellomfjellet is located in the north-south trending valley of Reisadalen, 20 km from Storslett in Nordreisa municipality (Figure 1). The unstable area of the mountain is located between approx. 200 and 500 m asl on the west-facing aspect. The field area covers 1.7 km^2 and encompasses in situ bedrock above and below the rock slope failure. A newly built power-line runs below the unstable area to the west and farms are located along the river in the valley. The closest farm is located 1.2 km downslope of the back-scarp. The unstable area has been divided into Mellomfjellet 1 (MF1) and Mellomfjellet 2 (MF2) for assessment purposes, as the morphological expression is different. MF1 has a discontinuous back-scarp striking both 345° and 025°, and covers a larger area than MF2. MF2 is bounded by a continuous back-scarp striking 025°, with multiple dislocated blocks. Upslope of the main unstable area at MF1 there are a back-scarp-parallel tension crack that tend to be deep and is snow-filled in summer.

2.2 Climate

The changing relief of Troms governs the local climate. Reisadalen, situated east of the Lyngen Alps, experience less precipitation (400 – 600°mm) than the coastal Tromsø (1100 mm). There is a seasonality to the precipitation, where winter and spring at Mellomfjellet experience less precipitation (average 30 mm/month) than the summer and fall (average 60 mm/month; Appendix B). The temperature regime in Reisadalen is sub-arctic with cold winters (average - 8.7° C) and cold summers (average 12.8 °C). Consequently, the area has a low permafrost limit, at c. 500 m asl, whereas it is c. 990 m asl in the coastal areas of the region (Blikra and Christiansen, 2014, Romanovsky et al., 2010). The snow arrives between October and January and lasts until May to July.

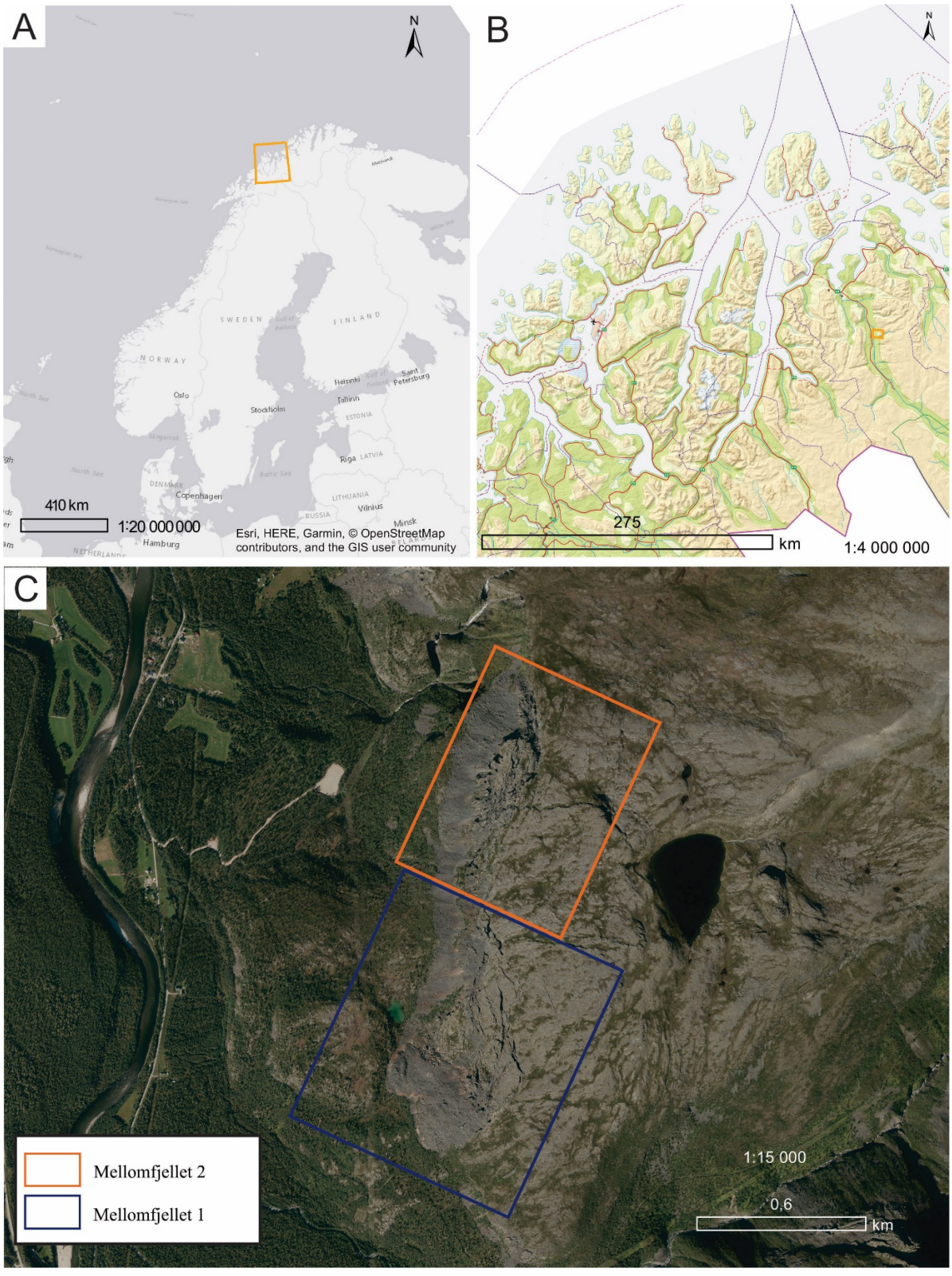

Figure 1 Location of MF1 and MF2.

2.3 Geological setting

2.3.1 Regional geology

The bedrock of North Norway consists of flat-lying Caledonian Nappes thrusted over Precambrian bedrock (Fennoscandian Shield) as a result of the collision between the Laurentia and Baltica tectonic plates in the early to mid-Palaeozoic (Andresen, 1988). The transition between Caledonide rocks and older basement is marked by topographic changes from the strandflat at the coast, to the fjord systems, to the gentle and rounded paleo surface basement of inner Troms.

Reisadalen Valley runs from the coast of Troms and into the rounder paleo surfaces of inner Troms and displays both strandflat/fjord topography at the coast and gently rounded paleo surfaces inland.

2.3.2 The Caledonides of Troms

The Caledonian rocks of Norway are subdivided into four allochthon units based on their inferred origin: the Lower, Middle, Upper and Uppermost Allochthon (Andresen, 1988). The Lower and Middle allochthons are considered to have a Baltic origin, while the Upper and Uppermost are Iapetus- and Laurentia-derived (Andresen, 1988). These allochthon events resulted in the formation of a series of imbricated nappe stacks (Figure 2; Faber and Stünitz, 2018).

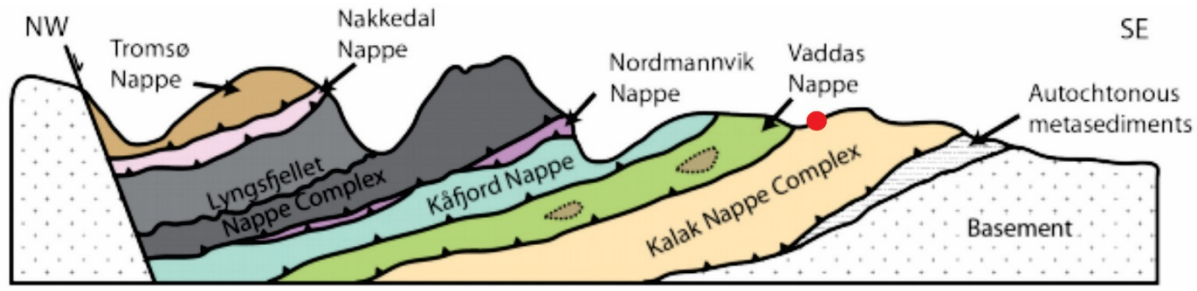

Figure 2 Schematic cross section across the Caledonide nappes in Troms (after Augland et. al 2014, Faber 2018). Mellomfjellet (indicated by red dot) is within the Kalak Nappe Complex and close to the Vaddas Nappe.

Multiple nappes outcrop in Troms and are delineated by predominantly NW-dipping major thrust faults (Zwaan 1988). Within Troms, the lowermost Caledonian rocks are the rocks of the

middle allochthonous Kalak Nappe Complex (KNC), which is immediately overlain by the upper allochthon rocks of the Vaddas Nappe.

2.3.3 Kalak nappe complex

The Baltica derived rocks of the KNC consist mainly of amphibolite facies schist, meta-psammites, and paragneisses. The KNC consists of several allochthonous thrust sheets with Proterozoic basement rocks, clastic metasedimentary rocks, and plutonic rocks. The Caledonian metamorphic grade is generally increasing upwards from greenschist facies at its base to amphibolite facies in the middle and upper units (Koehl et al., 2017). Mellomfjellet is located close the thrust fault between the KNC and the Vaddas Nappe and is a metamorphosed igneous body assumed thrusted in Late Ordovician to Early Ordovician (Zwaan, 1984).

There are two published bedrock maps for the area with different scales, one 1:50 000 map and one 1:250 000 map. The 1:250 000 map indicate that the lithology is amphibolite (metamorphosed gabbro) and meta-diabase (Zwaan, 1988). The 1:50 000 map indicates that the lithology at MF1 and MF2 is amphibolite and hornblende schist along with a thin layer of calcitic marble (Figure 3; Zwaan and Ryghaug, 1984).

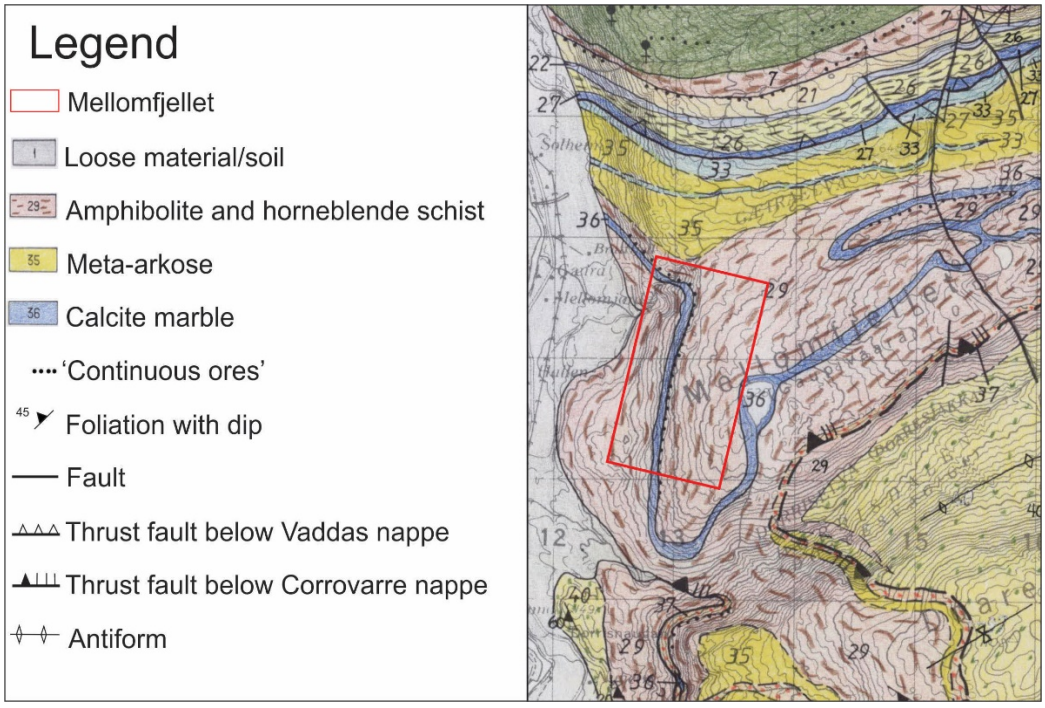

Figure 3 The 1:50 000 bedrock map at Mellomfjellet after Zwaan and Ryghaug (1984). Full map attached in Appendix A.

2.3.4 Post-Caledonian rifting

The continental margin of northern Norway is characterized by NNE – SSW and NE – SW striking lineaments, which intersect to form rhombic-shaped segments (Figure 4; Bergh et al., 2007, Indrevær et al., 2013)). There are three sets of discontinuities; a conjugate set of NNE – SSW trending extensional detachment planar faults, NE – SW trending normal faults and WNW-striking extensional Riedel shear fractures (Figure 4). The study by Indrevær et al. (2013) shows that brittle faults onshore and offshore occur predominantly as alternating NNW – SSW- and ENE – WSW-trending, steeply to moderately dipping normal fault zones. Indrevær and Bergh (2014) conclude that the fractures are linked to several post-Caledonian brittle faults that formed due to multiple rifting events in the Late Paleozoic-Mesozoic as parts of the opening of the North Atlantic Ocean. The brittle faults are suggested to be a reactivation of Precambrian and Caledonian structures such as lithological boundaries, foliations, ductile shear zones and faults (Indrevær et al., 2013).

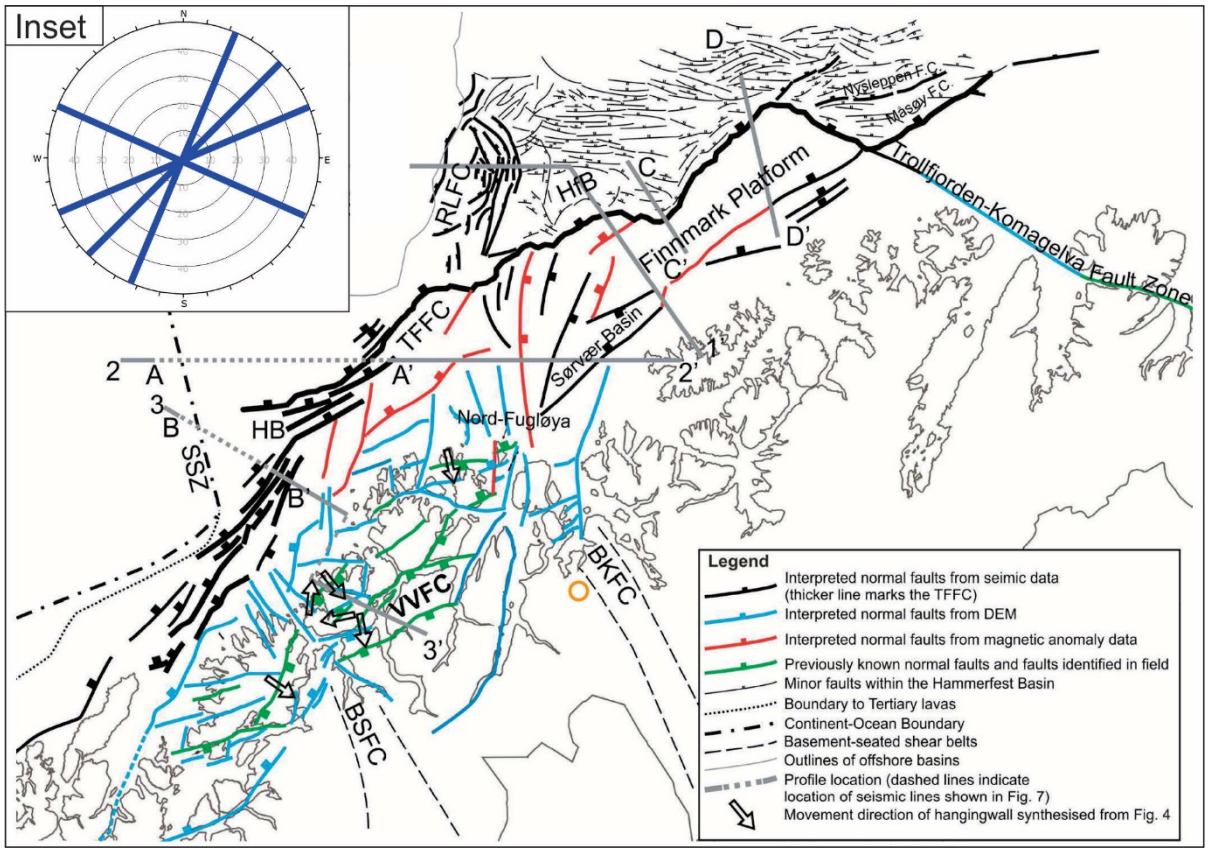

Figure 4 Regional map displaying faults onshore and offshore. Orange circle is the location of Mellomfjellet. BKFC – Bothnian-Kvænangen Fault Complex, BSFC – Bothnian-Senja Fault Complex, VVFC – Vestfjorden-Vanna Fault Complex. Inset display lineament trends. Modified after Indrevær et al. (2013).

2.4 Geomorphology and glaciation

The Quaternary glacial cycles have shaped the landscape of Troms, which is characterized by its U-shaped valleys, cirques, arête, pyramidal peaks and hanging valleys. The ice sheet once extended a significant distance out on the continental shelf. In large parts of Norway, the thickness of the ice sheet was as great as 3 km. Consequently, the current uplift rate from isostatic rebound in Troms is high, up to 1 – 1.5 mm/year (Dehls et al., 2000). The last glaciation in Reisadalen occurred approx. 10 000-year B.P. and the ice retreat is traceable in the moraines and ice front deltas deposited under colder periods post last glacial maximum (Bergstrøm, 1983). The Bergstrøm (1983) article describes the deglaciation of Reisadalen and shows a glacier free front of Mellomfjellet between the Storbakken event (>9750 B.P) and Bergmo event (>9500 B.P).

Glacial cycles influence rock mass stability. The weight of the overlying ice and its movement increases the stress levels both on the valley floor and within the valley walls (Ballantyne, 2002). The steepening of the rock slope and deepening of the valley increases the height of the slopes and therefore the shear stress acting on the rock mass (Ballantyne, 2002). Part of the resulting ice-load deformation of rock masses is elastic and stored within the rock mass as residual strain energy (Wyrwoll, 1977). When the ice melts, the glacially stressed rock releases the strain energy. The stress release generally results in propagation of the internal joint network, together with a loss of cohesion along joint planes and a reduction of internal locking stresses (Ballantyne, 2002, Wyrwoll, 1977). There are several ways that the over-steepened debuttressed rock slope adapt: large-scale catastrophic rock slope failures, large-scale rock mass deformation, or rapid adjustment of rock faces by frequent rock-fall events are common for debuttressed and over-steepened rocks slopes (Ballantyne, 2002). Evidence of glacial influence is observed in Reisadalen as there are four URS observed by NGU: Doaresgaisa, Brattfjell, Rajajoki and Mellomfjellet (NGU, 2018).

2.5 Previous work

The unstable mountains in Troms have been the subject of an ongoing study over the last decade both by universities and by NGU on behalf of The Norwegian Water Resources and Energy Directorate (NVE; Bunkholt et al., 2012, Böhme et al., 2016, Eriksen, 2013). Master theses completed at the university of Tromsø have been written concerning structure, morphology and

failure mechanisms of the URS (e.g. Bakkhaug, 2015, Bjørklid, 2017, Eriksen, 2013, Grumstad, 2017, Hannus, 2012, Hernes, 2014, Husby, 2011, Larsen, 2014, Nopper, 2015, Rasmussen, 2011, Sandnes, 2017, Skrede, 2013, Bredal, 2016).

NGU first visited Mellomfjellet in their field campaign of 2009, which involved a helicopter fly-over and a site investigation. Fly-overs have been conducted several times in the subsequent years. These field investigations, together with active movement identified by InSAR, has led the team from NGU to assign a moderate to low priority with a recommendation not to follow up with terrestrial LIDAR-scanning due to little to no consequences.

The following information is a summary of an assessment of Mellomfjellet presented in the NGU report by Henderson et al. (2010).

2.5.1 Mellomfjellet 1

- Foliation dips towards the valley at an angle of 15° – 25°. This dip is considered too low for the rock mass to be sliding along foliation-parallel discontinuities.
- Several discontinuous back-scarps are observed trending NNW-SSE and NE-SW making a wedge-shaped block (Figure 5A).
- They assume a low-angled failure surface parallel with the foliation that controls the discontinuities below the blocks (Figure 5E).
- InSAR shows that the block could be divided into two smaller blocks with respectively 7 – 9 mm/year and 2 – 3 mm/year displacement (Figure 5B).
- Recent rock falls are observed below the lower block and at a lobe lower in the slope (Figure 5G and I).
- The southern scarp clearly defines the extent of the rock slope failure and indicates that the source area is structurally controlled (Figure 5A).
- The tension crack indicate a depth of at least 50 m to a possible failure surface. This gives a volume of 8 million m^3.
- The slope towards the valley is gentle and a possible damming of the Reisaelva is unlikely.
- There are also no settlements directly below the mountainside and thus a moderate to low priority is assigned to the URS.

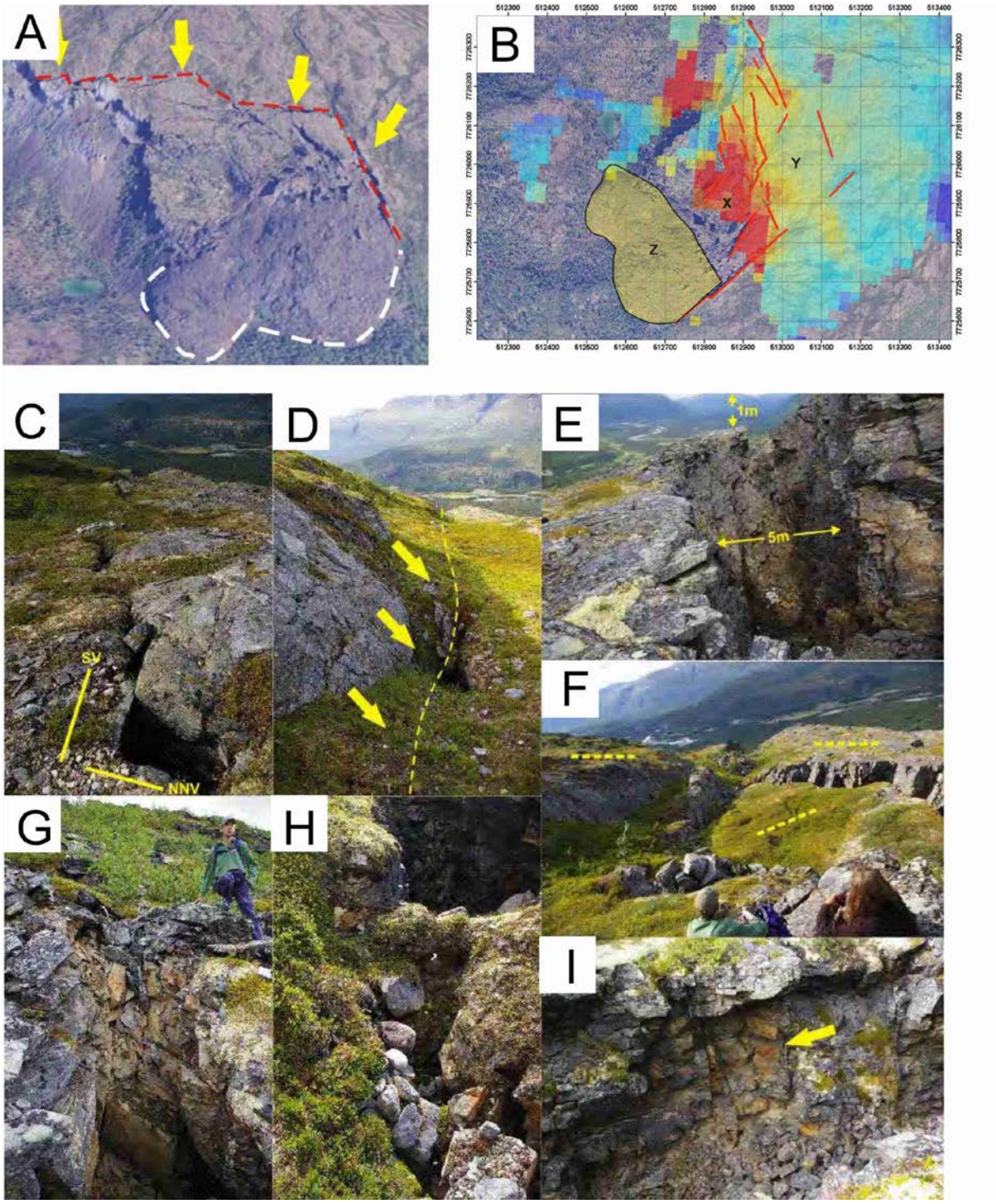

Figure 5 The figures are modified and obtained from Henderson et al. (2010). A – Aerial photo from Norway in 3D (www.norgei3d.no) that shows Mellomfjellet 1 from west. The yellow arrows display the stable slope east of the back-scarp, red line marks the back-scarp and the white line limits the talus. B – InSAR over Mellomfjellet 1. X marks area with high displacement (9 mm/year), Y an area with less displacement (2 – 3 mm/year) and Z marks an area with new rock-fall deposits. C – The two joint directions displaying most displacement towards the valley. D – A relatively old and inactive fault plane in SW direction. The yellow arrows display the movement along the fault plane. E – A NNW trending fracture with approx. 5 m horizontal and 1 m vertical displacement. This coincides with a low angled failure surface. F – Back-tilting of some blocks. G – A recent rock-fall on a SW-trending joint. H – Disturbance of the vegetation on a NNW-trending joint. I – Recent rock-fall activity on a NNW-trending joint (shown with the yellow arrow).

2.5.2 Mellomfjellet 2

- This locality is north of MF1 and is part of the same fracture system.
- The valley-parallel fractures are more prominent and trend NNE – SSW. The area is divided into two blocks where InSAR data gives up to 8 – 9 mm/y displacement in the northern parts and 2 – 3 mm/year in the southern parts (Figure 6A and B).
- The volume of the unstable slope is estimated to 9 million m^3 when the minimum depth to the possible failure surface is estimated to be 100 m.
- The distance to the valley floor is shorter and steeper and there is a farm nearby.
- A catastrophic failure could possibly dam the river and cause damage to houses and people (Henderson et al., 2010).

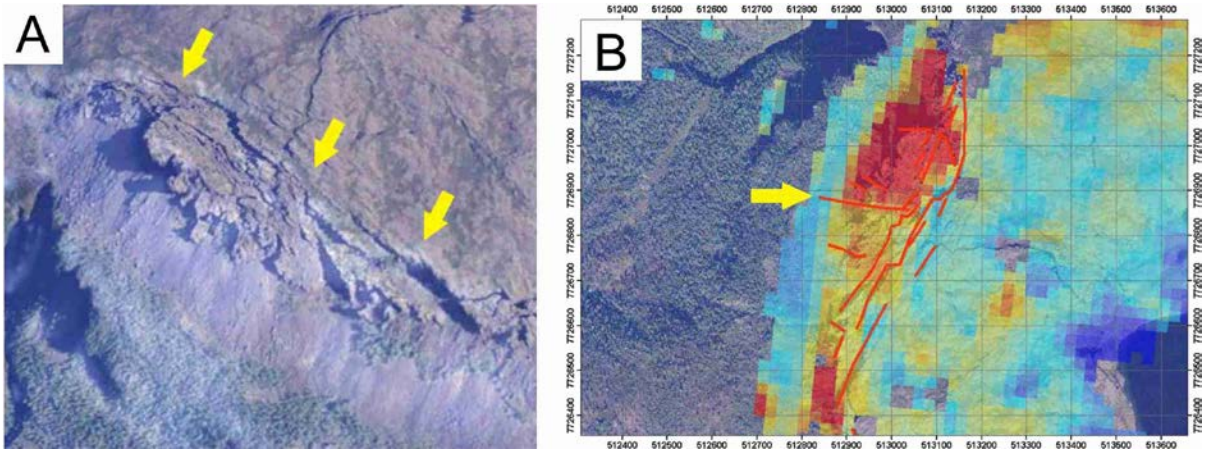

Figure 6 Figures obtained and modified from Henderson et al. (2010). A – Aerial photo from Norway in 3D (www.norgei3d.no) that shows Mellomfjellet 2 from west. Yellow arrow display the easternmost scarps. B – InSAR over Mellomfjellet 2. An E – W fracture divides the block in two (marked with a yellow arrow). The northern part displace faster than the southern part of the block.

3 Methods

3.1 Geological and geomorphological mapping

3.1.1 Field work

Fieldwork was conducted between the third and 14th of September 2018. The site investigation covered structural mapping of discontinuities, geological and geomorphic mapping of the area, several drone flights, general observations and photography. The structural data was recorded in strike and dip consistent with the right-hand rule. The focus was on examining bedrock structures like foliation and discontinuities. A vital part was to observe hydrogeological conditions in the area by mapping streams and boggy terrain. Rough terrain and unstable conditions influenced the mapping due to the limited accessibility in certain areas. The steep, high back-scarp was not easily accessed in parts and was therefore investigated using drone photogrammetry.

During the field campaign 970 structural measurements of discontinuities at 31 individual data stations where obtained. The stations include both in situ and unstable locations. A large number of measurements are necessary, as there are large variations in the in situ structural data due to the pervasive gentle folding and varying foliation orientation across the site. The roughness description is consistent with the field guide sheet from New Zealand Geotechnical Society (Appendix G). The condition of the joint surface, in terms of coating, has been noted.

A DJI Inspire 1 with a Zenmuse X3 12-megapixel camera was used for photogrammetry and video capture. High-quality aerial images from helicopter flyover (from NVE) provided advantageous overview angles of the whole study site.

A Garmin GPS Map 64st was used for positioning, and a compass with inclinometer was used for structural measurement.

Geomorphological and geological maps have been produced in ArcMap 10.5. The topographical map of Norway was obtained from www.norgeskart.no via a WMS-service. Orthophotos were obtained from www.geonorge.no via a WMS-service. The Artic DEM provides a 3m x 3m resolution over the area (Porter et al., 2016). The geographical coordinate system used is WGS 1984 UTM 33N.

3.2 Structural analysis

3.2.1 Dips

The structural data was displayed and analyzed in Dips 7.0 with stereographic projection (lower hemisphere, equal area and fisher distribution). Poles of the structural data were plotted and presented with contour lines drawn based on the concentration of poles in each 1% area of the surface of the lower hemisphere (Wyllie and Mah, 2014). Rocscience (2018) recommends that a cluster with a maximum concentration greater than 6% is very significant while 4 – 6% represents a marginally significant cluster. Clusters with less than 4% maximum concentration should be regarded with suspicion unless the overall quantity of data is very high. Spatial variation within the defined sets is displayed as a variability cone with a radius of one standard deviation (σ). Fold axes was estimated using a statistical fold analysis in Dips.

3.2.2 Kinematic analysis

Kinematic analysis is a tool for evaluating the feasibility for failure along discontinuity sets relative to the slope orientation. The procedure follows principles described in Hoek and Bray (2014) and Wyllie and Mah (2014) where the modes of failure are planar, wedge and flexural or direct toppling. The hazard assessment of large URS at NGU uses a modified model to account for the more complex structures and variable slope orientation in large rockslides (Figure 7; Hermanns et al., 2012). The lateral limit restriction for planar sliding and wedge sliding is increased to 30° and a weighted output is introduced. The flexural toppling and wedge sliding use the 45° lateral limit cut-off for the complexity of large rock slopes (Hermanns et al., 2012). A higher score (0.75) is attributed if the difference between sliding direction and slope aspect is smaller than 30° and a lower score if it is greater (0.5; Figure 7).

Hermanns et al. (2012) recommends using a friction value of 20° as a conservative value for all Norwegian rock types. Block toppling occurs only in minor rock volumes except for flexural toppling, which can affect large rock masses (Hermanns et al., 2012). Direct toppling is therefore omitted from the large-scale analysis.

Dips 7.0 from the Rocscience suite was used for kinematic analysis. Structural data, the slope direction and angle and the recommended friction angle (Hermanns) were used. The number of poles or intersections in the critical zones are automatically counted and simple statistics are provided for the kinematic feasibility for each possible failure mechanism.

The critical zone varies for the different modes of failure. For planar sliding, the discontinuity must daylight in the topography. The discontinuity needs to dip in the same direction (within the lateral limits) as the slope and be steep enough to exceed the friction angle (Wyllie and Mah, 2014). These parameters define the critical zone for planar sliding (Figure 7). The same scenario applies for wedge sliding, where the intersection line of the two intersecting planes must daylight the slope, be steeper than the friction angle and be inside the lateral restrictions. For toppling failures, the dip direction of the discontinuities dipping into the slope must be within a small angle with respect to the dip direction of the face.

Slope dip has a great impact on the feasibility for kinematic analysis and slope aspect, angle and dip were derived from ArcGIS with “Slope (Spatial Analyst)”. A steep area in each domain will provide slope dip. The results are presented in stereonets and tables summing up the statistical data for each domain. The critical zone for each failure mechanism is represented with dark colors and the partly possible failure mechanisms is represented in lighter colors.

Dips is a geometrical analysis tool that, with the aid of simple statistics, calculates the feasibility for different failure mechanisms based on given parameters. The nature of the discontinuities regarding persistence, spacing, infill or mechanical properties is not considered. Therefore, the results should be handled with care.

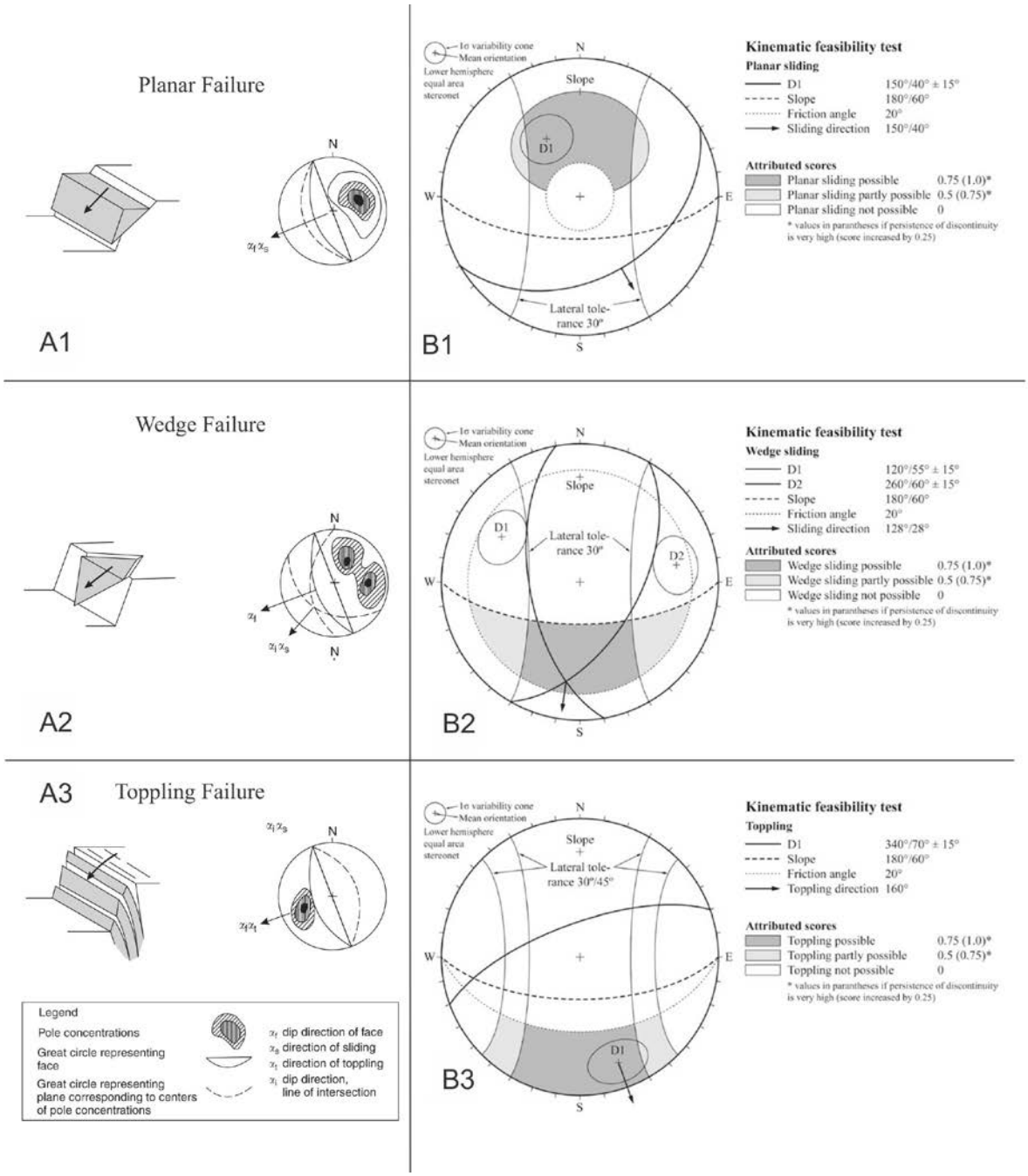

Figure 7 Sketch of different failure mechanisms and appearance in a kinematic feasibility test. A – After Wyllie and Mah (2014) and B – After Hermanns et al. (2012).

3.3 Photogrammetry

3.3.1 Structure from motion

The technology for making photogrammetry has evolved rapidly over the last decade. Unmanned aerial vehicles (UAV) surveying provides a cost and time efficient method for on-site and close-range collection of oriented data. Agisoft Photoscan is a professional tool for photogrammetry that was used to create a 3D-model of the northern back-scarp. The program uses structure from motion (SfM) photogrammetry, which automatically identifies matching features in multiple images to reconstruct camera pose and scene geometry (Figure 8). The product is a three-dimensional point cloud which could be aligned in an absolute coordinate system with known ground-control points (GCPs; Westoby et al., 2012). Details on the method can be found in Micheletti et al. (2015) and Westoby et al. (2012).

The quality and accuracy of the 3D-model depend on the following input data and the SfM processing; GPS precision, processing procedures, image overlap and quality, number and spatial distribution of GCPs, target distance, camera specifications and correction all affect the SfM results. Errors and inaccuracies in the mentioned input data may induce uncertainty to the results. The processing is highly governed by the quality of the pictures and the precision of the GCPs and insufficiencies may lead to skewness and uncertainty in the acquired point cloud.

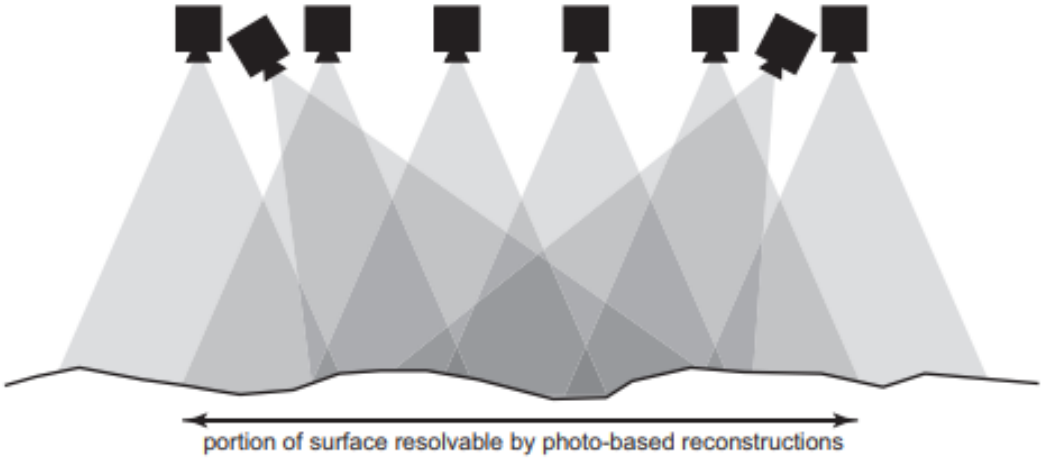

Figure 8 SfM principle. Obtained from Bemis et al. (2014).

3.3.2 UAV survey and data acquisition

The quality of the photogrammetry analysis is highly governed by the accuracy and quality of the pictures taken in the field. High quality images with enough overlap is the main goal of the image capture. Agisoft Photoscan User Manual 1.4 recommends 60% of side overlap and 80% of forward overlap. Inclination and overhang in the slope introduce the need of inclined image-capture to obtain enough overlap and cover of the whole rock-face, which is roughly 100 m long and up to 15 m high. Three flights were conducted at different heights above the slope with two or more inclinations per flight, see Appendix C for specifications. The survey resulted in 293 pictures of the back-scarp. A high contrasting set of spray-cans where used to mark the six ground control points. The standard GPS used for fieldwork was used to geographically locate the GCPs. The time frame and budget didn't allow for a high precision GPS station which is recommended for this kind of survey.

A terminal server at the University of Tromsø was used to provide extra processing power. The main processing in Agisoft Photoscan involves producing a high-quality point cloud to produce a dense cloud and DEM. The workflow and parameters used are described in Appendix C.

3.3.3 Coltop3D

Coltop3D is a software that symbolizes points in a point cloud. The software computes the orientation of each point based on neighboring points and assigns an unique color code for each spatial orientation (Figure 9; Jaboyedoff et al., 2007). The orientation data was obtained by drawing polygons around known structures which could be processed further, i.e. in Dips (Coltop3D, 2016).

This method allows to obtain information about the orientation of structures in less reachable areas, such as the back-scarp at Mellomfjellet. The results of the analysis should be treated with professional judgement to see whether the Coltop3D data coincides with the field data.

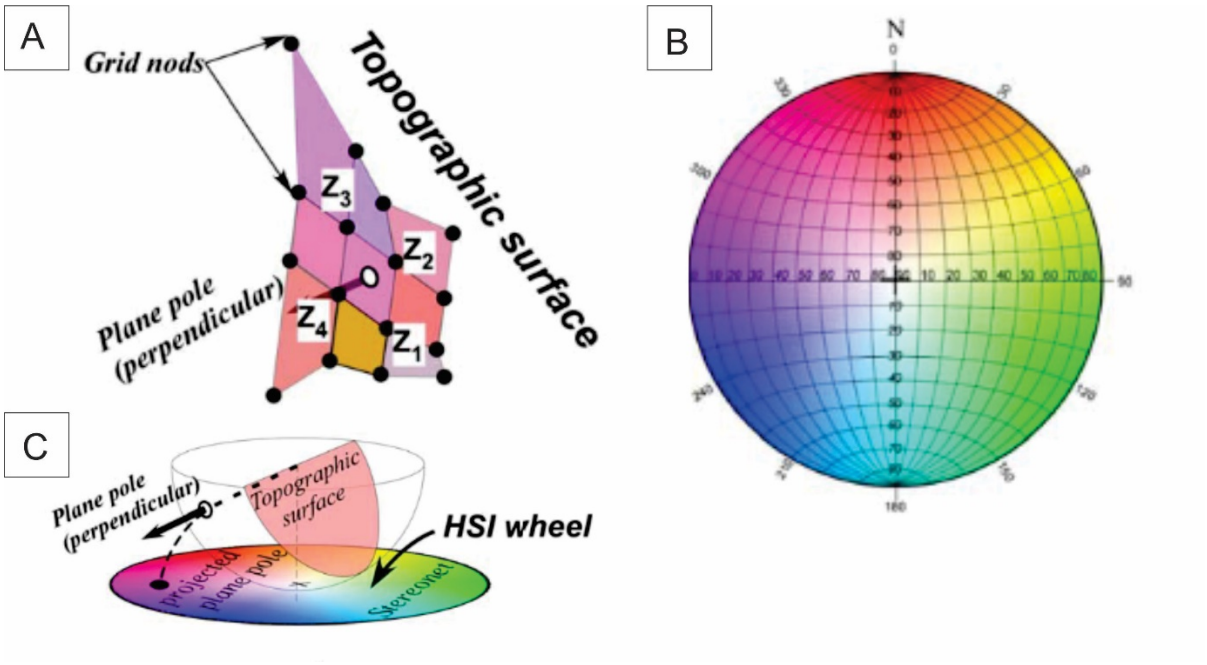

Figure 9 Coltop3D methods. A - Orientation of topographic surface. B - The HSI-wheel plotted on a stereonet. C - Relationship between the Schmidt-Lambert projection and the HSI wheel. Modified from Jaboyedoff et al. (2007)

3.4 Deformation mapping with InSAR

3.4.1 Method

Interferometric synthetic aperture radar (InSAR) is a remote sensing method used to observe changes in Earth's surface. The method uses a synthetic aperture radar (SAR) which is an active remote sensing imaging instrument (Pepe and Calò, 2017). The radar operates in the microwave regime of the electromagnetic spectrum and is therefore almost independent of meteorological conditions and sun illumination (Bamler and Hartl, 1998). High spatial resolution imagery is now easily accessed through the Sentinel 1 satellites.

The space-born satellite sends out microwave pulses obliquely across a ground swath with a side looking fashion (Figure 10A). A fraction of the initial pulse is echoed (back scattered) to the antenna and the signal is processed to create a microwave image of the observed area. InSAR uses measurement of the phase difference between two or more SAR images to create an interferometric image, which displays the difference in phases between two SAR-images (Figure 10B; Pepe and Calò, 2017). This image could be used to measure i.e. deformation (Bamler and Hartl, 1998). The InSAR data gives relative movement along the line of sight.

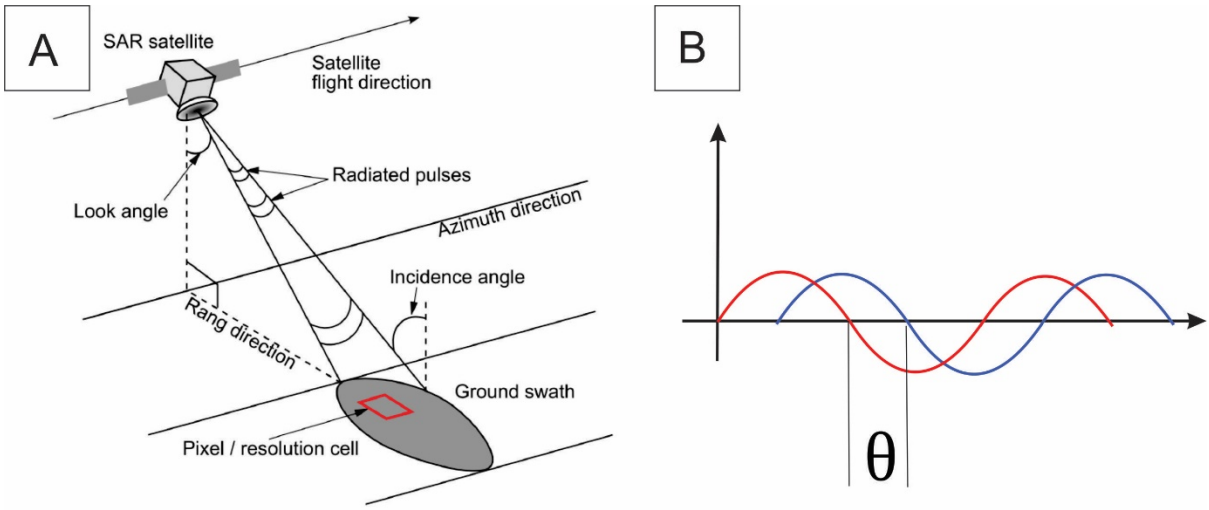

Figure 10 A – SAR imaging geometry. x - Azimuth. y - Ground range. Obtained from Eriksen (2013). B – Phase shift visualized by horizontal shift from the original wave (red) to the shifted (blue) wave.

3.4.2 Limitations

The terrain area imaged in each SAR resolution cell depends on the local topography. There are several geometrical problems with InSAR in steep mountain terrain; *foreshortening* is the effect that the pixel on the ground compress or dilates with respect to the mountain slope, resulting in loss of details, *layover* is the effect when the mountain top is closer to the radar than the foot of the mountain, resulting in reverse imaging of scatters and superimposed images, *shadowing* of the radar signal appears in areas not illuminated by the radar (Ferretti et al., 2007). Changes in the backscatter reflectivity between acquisitions reduces the quality of the coherence in the interferograms and decorrelation occurs. The change might come from snow, vegetation, and high displacement velocities (Eriksen et al., 2017). The displacement is measured in the line of sight from the satellite and therefore N – S displacement is therefore not acquired.

3.4.3 Datasets

NGU has provided several datasets originating from the Radarsat-2 and Sentinel-1 satellites. The datasets consist of ascending and descending data from both satellites as well as different processing of the datasets. Radarsat-2 is a set of polar orbiting satellites at altitude 798 km with a repeat interval of 24 days while the polar orbiting Sentinel-1 satellites orbits at an altitude of 693 km with a repeat interval of 6 days. Obtained data from the Radarsat-2 are processed with

small baseline (SBAS) which counts all pixels as equal while the Sentinel-1 processing use persistent scatter interferometry (PSI) which add more focus on pixels with powerful reflectors.

The incident angle for Radarsat-2 is 31° and for the Sentinel-1 data, it is ~43.3° from vertical, which needs to be accounted for when examining the results. The descending datasets are used as the look direction of the radar is to the right and show the expected westward displacement better than the ascending datasets.

The Radarsat-2 dataset from Mellomfjellet is averaged across 2007 – 2017 and the Sentinel-1 averages from 2015 – 2018. The Sentinel-1 data is presented as vector data and the RSAT-2 data as raster. Therefore, the Sentinel-1 data is presented with a polygon analysis and the RSAT-2 a profile analysis along with the maps.

3.5 Workflow for assessment of consequences of rock avalanches in Norway

NGU recommends using their hazard and risk classification system for large URS in Norway. It is a classification system that is built on a qualitative hazard and a quantitative consequence analysis that focuses on relevant geological data for assessing the likelihood of failure (Hermanns et al., 2012). It is a scenario-based approach as the rate of displacement and the geological conditions may vary significantly on slopes. The input data falls in three categories; one relies on geomorphological criteria, second on structural criteria, and the third is based on the activity of the slope regarding displacement rates and current or previous landslide events. The method for consequence analysis of URS follows five steps: (1) definition of scenario based on structural site investigation and displacement rates, (2) volume estimation, (3) estimation of runout, (4) assessment of potential secondary effects like displacement waves or damming of rivers, and (5) assessment of the number of people that live or stay in the runout area.

It is a classification system built for the special geographical and geological conditions in Norway that is dominated by crystalline rocks and does not accurately reflect the hazard from large rock slopes that comprise weak sedimentary rocks (Hermanns et al., 2012).

The hazard analysis is based on the following geological parameters:

- Development of the back-scarp
- Potential failure surfaces
- Development of lateral release surfaces
- Kinematic feasibility test
- Morphologic expression of the basal rupture surface
- Landslide displacement rates
- Change of displacement rates
- Increase in rock fall activity on the unstable slope
- Presence of post-glacial events along the affected slope and its vicinity

3.5.1 Volume estimation

The volume estimation method used in this thesis is based on the sloping local base level (SLBL; Jaboyedoff et al., 2004a). With the aid of a digital elevation model (DEM) of the bedrock along with an estimation of the failure surface, the volume is calculated. The SLBL-method uses the concept of base level, the lowest level to which running water can erode, and applies it to URS. The sloping base level is assumed to be the lowest erodible level of a rock slope failure.

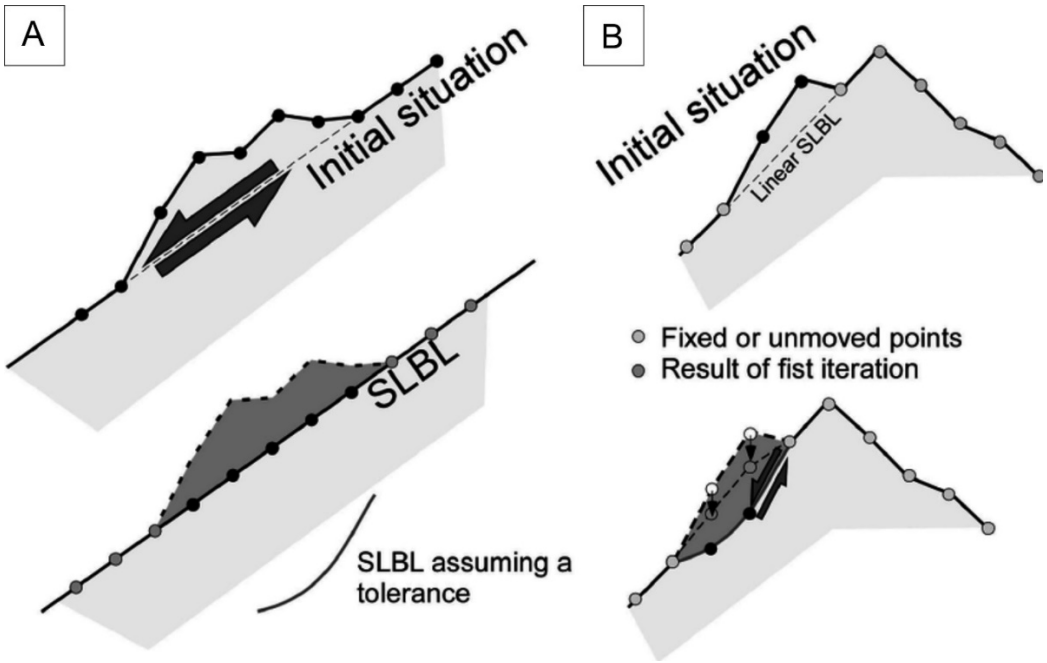

Figure 11 A – Linear SLBL with no tolerance. B – Illustration of a rotational SLBL assuming a negative tolerance. Obtained from Jaboyedoff et al. (2004b).

A mountain that bulges out of an otherwise steep slope is thought to be prone for landslide processes until an even slope is developed (Figure 11; Oppikofer et al., 2016).

An ArcGIS-tool, programmed at NGU, is used to calculate different SLBL surfaces. A DEM, a polygon of the unstable area and the curvature tolerance are necessary as input to the tool.

The curvature tolerance is calculated based on the length of the unstable area in slope direction, height difference between the highest and lowest point of the unstable area, base layer angle along back-scarp and the toe, and DEM cell size. A SLBL Excel spreadsheet is used to calculate minimum, intermediate and maximum curvature tolerance. The minimum tolerance is assumed to be the shallowest possible base layer with a planar surface from back-scarp to the toe. The maximum tolerance is an elliptical surface with a larger curvature tolerance and the intermediate is found in between. The maximum tolerance is used to show the uncertainty in the volume calculation. The constructed SLBL surfaces are validated with profiles. Finally, the difference in between the present topography and the SLBL surface is used to calculate the volume of the unstable rock slope. Details on the methods and calculations can be found in (Jaboyedoff et al., 2004b, Jaboyedoff et al., 2015, Oppikofer et al., 2016).

3.5.1.1 Limitations

There are limitations to the use of the estimated volumes. The method does not account for structures in the bedrock and assumes a singular curved sliding surface.

3.5.2 Run-out analysis

Run-out area is the area that is reachable by a landslide from its source (Oppikofer et al., 2016). There are several methods to evaluate run-out distance. The empirical relationship between angle of reach and landslide volume are used in this thesis.

3.5.2.1 Angle of reach

The empirical relationship formulated by Scheidegger (1973) between the fall-height, run-out length and volume of landslide is:

$$tan\,\alpha = \frac{H}{L} = 10^{0.62419} \cdot V^{-0.15666}$$

In this relationship, the angle of reach (α) is dependent on the volume of the landslide (V). When knowing the volume, an estimate of the angle of reach is obtainable. A study by Blikra et al. (2001) evaluated 25 landslides in Norway and more than 90% of these have a higher angle of reach than the Scheidegger curve (Figure 12). Therefore, it is assumed that the curve is a conservative approach for maximum run-out length for landslides in Norway.

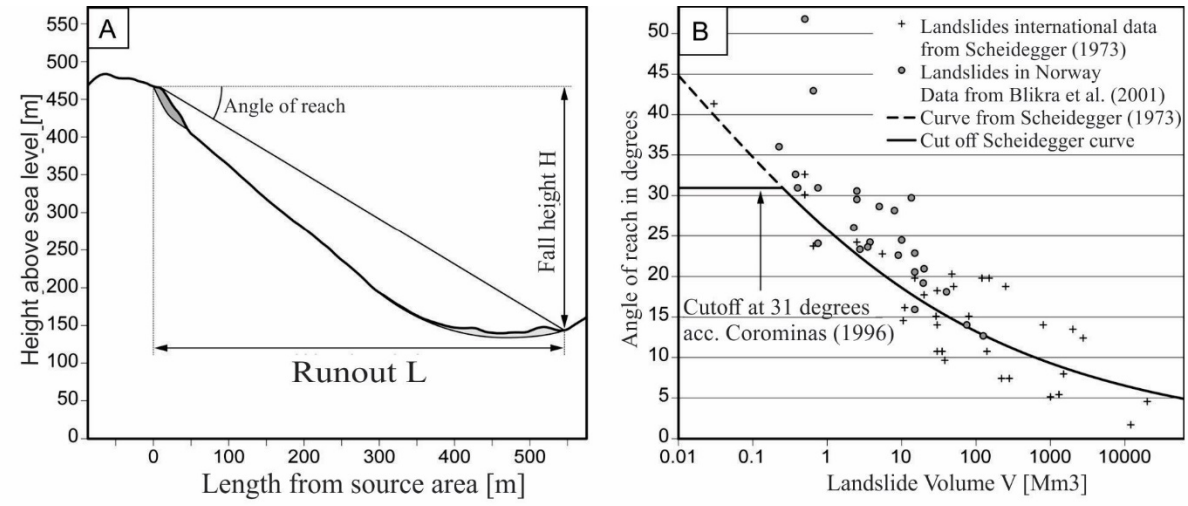

Figure 12 A – Angle of reach. B – Scheidegger curve along with data from Blikra et al. (2001). Obtained from Oppikofer et al. (2016)

3.5.2.2 Flow-R

Flow-R (www.flow-r.org) is a Matlab based run-out modelling program. It was developed at the University of Lausanne in Switzerland initially for susceptibility mapping of debris flows on a regional scale. The model is used for variations of run-out modelling from earth flows and debris flows as well as rock-falls and large rock avalanches (Horton, 2014, Horton et al., 2013). The model inputs are a DEM of the assigned area and a raster file of the unstable source area. When examining large rock avalanches, the angle of reach is also a necessary input. Output of the program is a raster with the probability of runout length and a raster with the estimated kinematic energy.

The lateral propagation is calculated with a multiple flow direction algorithm (Holmgren, 1994). It follows the principle that a flow is spreading on to one or more neighboring cells depending on the height difference between the cells (Figure 13). The model has been customized for large-scale rock avalanche by Horton (2014) to account for inertia and

thickness. Inertia is accounted for by the memory effect; a mass does not change its flow direction suddenly or by large amounts (Fischer et al., 2014). This allows for uphill travel across valleys and makes the path less influenced by small obstacles in the runout area. The change in direction from cell to cell is restrained by the opening angle (θ) and different directions have likelihoods with a triangular distribution where the likelihood to travel straight is highest. The inertia model is combined with the modified Holmgren (1994) stream model to calculate the total likelihood for an avalanche to spread from cell to cell. The runout stops if the spreading likelihood becomes less than a preset threshold.

The potential and kinematic energy for the avalanche is analyzed using a simple friction model that governs the run-out distance. The potential energy is transformed to kinetic energy. The energy is lost through internal friction and friction along the slope. The energy loss is represented with an energy line that runs from the back-scarp with downslope angle β. This angle (β) is set to be the angle of reach, so that all energy is lost when the landslide reaches the angle of reach (Oppikofer et al., 2016).

The following parameters were used: Holmgrens stream algorithm (x=1), height modification (dh= 10 m), opening angle (θ= 120°), runout cutoff (3 x 10-4) and memory effect (n = 25n cells). Details on the computation are described in Horton et al. (2013) and for the large rock avalanche in Horton (2014).

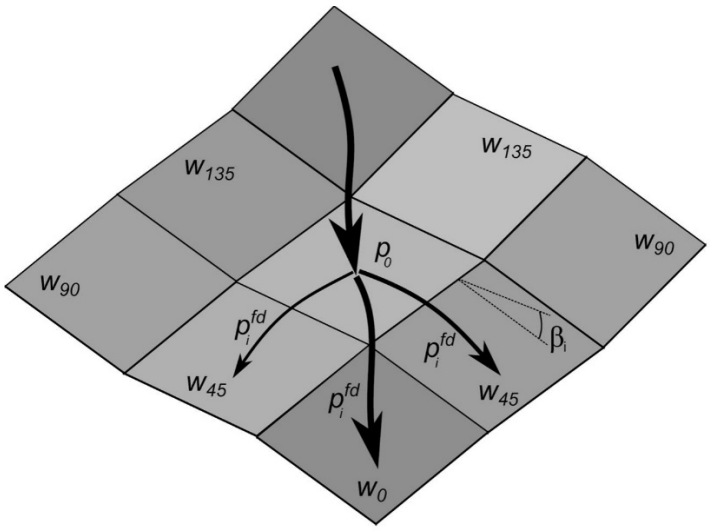

Figure 13 Principle of the multiple flow directions.

3.5.3 Risk assessment

The risk classification proposed in Hermanns et al. (2012) uses the hazard analysis described section 3.5 to give the investigated URS a hazard class (hazard score). The described volume estimation (section 3.5.1) and the following run-out modelling (section 3.5.2) provide models to estimate the potential for loss of human life. The hazard score is plotted against the potential consequences and a risk class is assigned (Figure 14). The risk classes are divided into three: low-, medium- and high-risk objects.

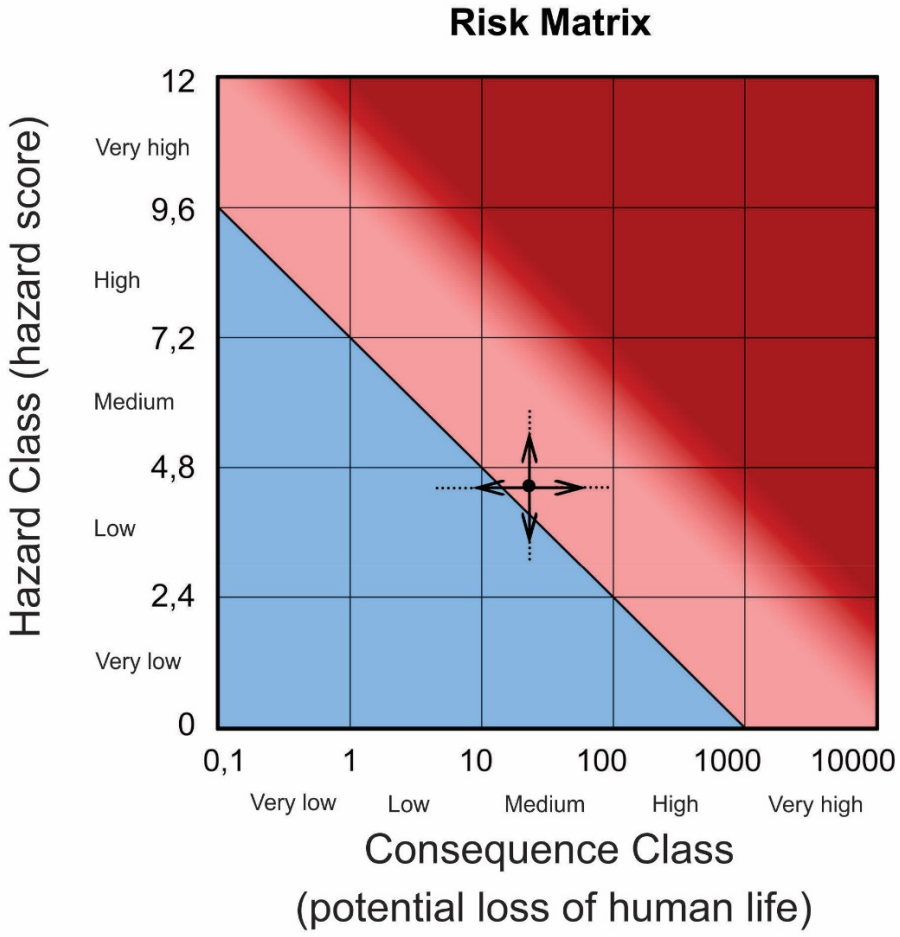

Figure 14 Risk classification matrix. Blue - Low risk, pink - moderate risk and red - high risk (Hermanns et al., 2012).

4 Results

4.1 Structural data

The structural data from Mellomfjellet are presented in Appendix D with separate maps displaying joints and foliation. Geographical locations of the different structural data are found in Appendix D and Figure 15. The majority of the field stations are situated in close proximity to the back-scarp while some are situated in the stable areas in the periphery of the unstable area. The study area was separated into two structural domains, MF1 and MF2, based on homogeneous discontinuity orientations in the different sets (Figure 15). A change in foliation was observed from MF1 to MF2 as well as a change in dip in joint set 3.

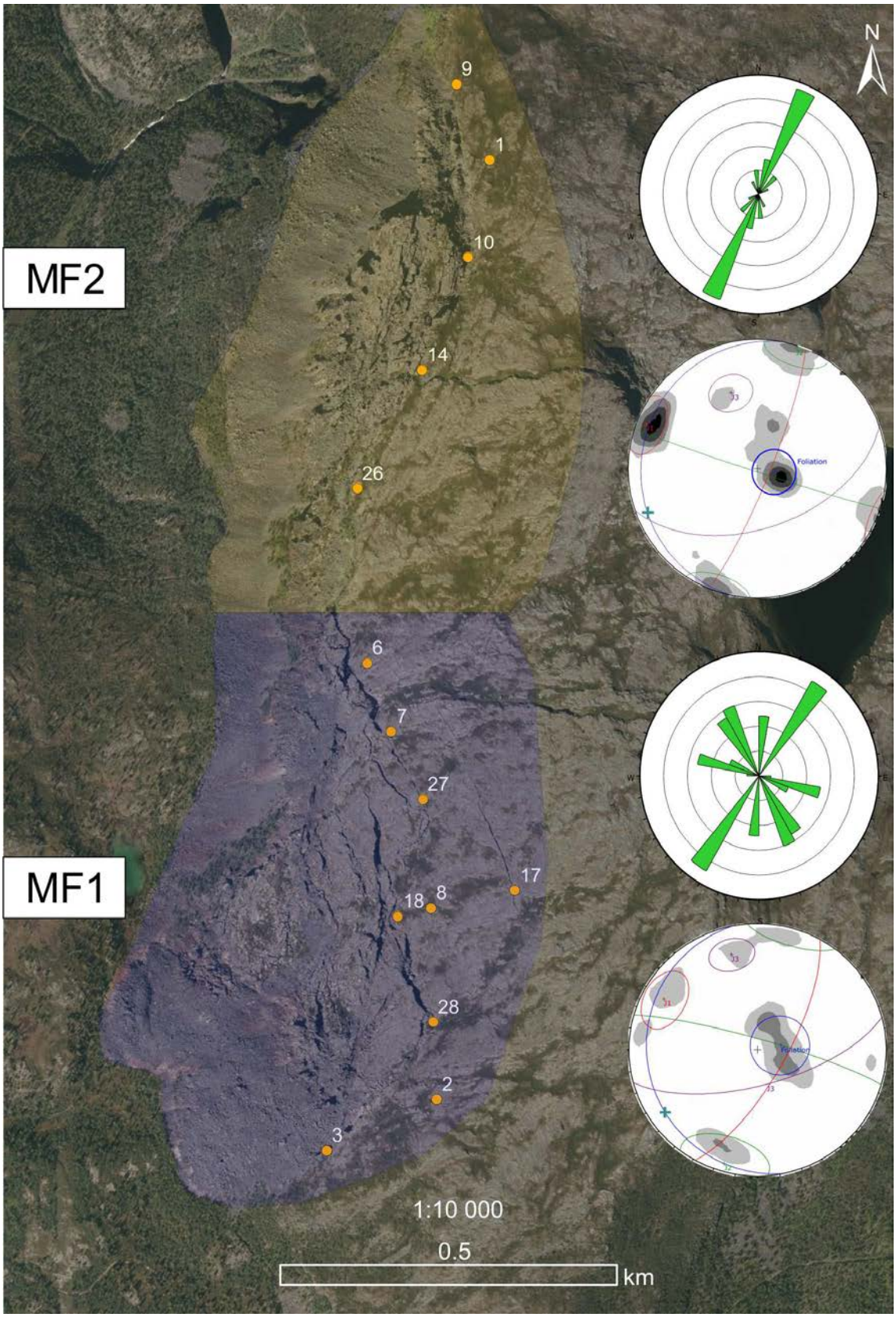

Figure 15 Structural domains at Mellomfjellet. MF1 in blue and MF2 in yellow. Roseplots of lineations and stereonets of discontinuities are shown. Field stations used in the structural analysis are presented in orange circles.

4.1.1 Mellomfjellet 1 domain

Mellomfjellet 1 domain is based on the structural data from in situ field stations close to the back-scarp (Figure 16). The structural cluster analysis resulted in four discontinuity sets. The foliation and joint set 2 (J2) are marginally significant clusters (4 – 6 %) and joint set 1 (J1) and joint set 3 (J3) are not statistically significant (Figure 16). J1 and J3 are however well documented in the field and therefore considered significant structures in the further analysis. The foliation is gently folded with a wavelength of roughly 5 m and three measured fold axes show downslope plunging (20° → 245°, 15° → 255°, 21° → 236°; Table 1). The calculated fold axis from foliation measurements at MF1 is displayed in Figure 16 and is gentler plunging than measured in the field. The back-scarp is discontinuous and trends in a zigzagging pattern along J1 and J2 following 345° and 025°.

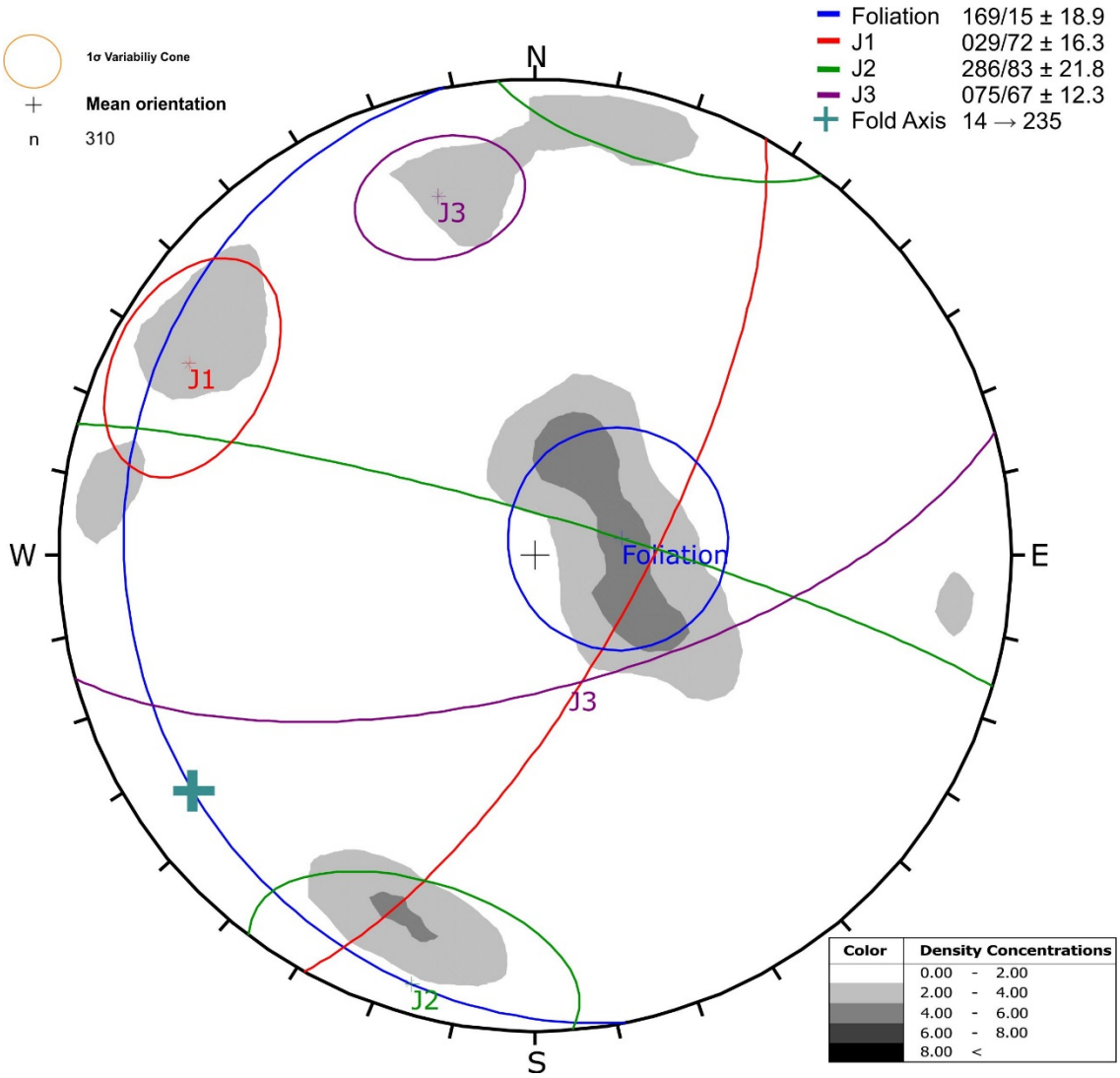

Figure 16 Stereonet displaying contours of discontinuity poles and assigned sets from MF1.

4.1.2 Mellomfjellet 2 domain

Mellomfjellet 2 is based on structures mapped close to the back-scarp and from the photogrammetry model (Figure 17, Figure 20 and Table 1). There are two statistically significant clusters; foliation and joint set one (J1; Figure 17). Joint set 2 (J2) is marginally significant and joint set 3 (J3) is not statistically significant, but well documented in field and therefore considered significant. J1, J2 and J3 are quite similar for both domains visualized in the great overlap in the standard deviation (σ) cones. The greatest difference is found in the strike of the foliation and in the dip of J3.

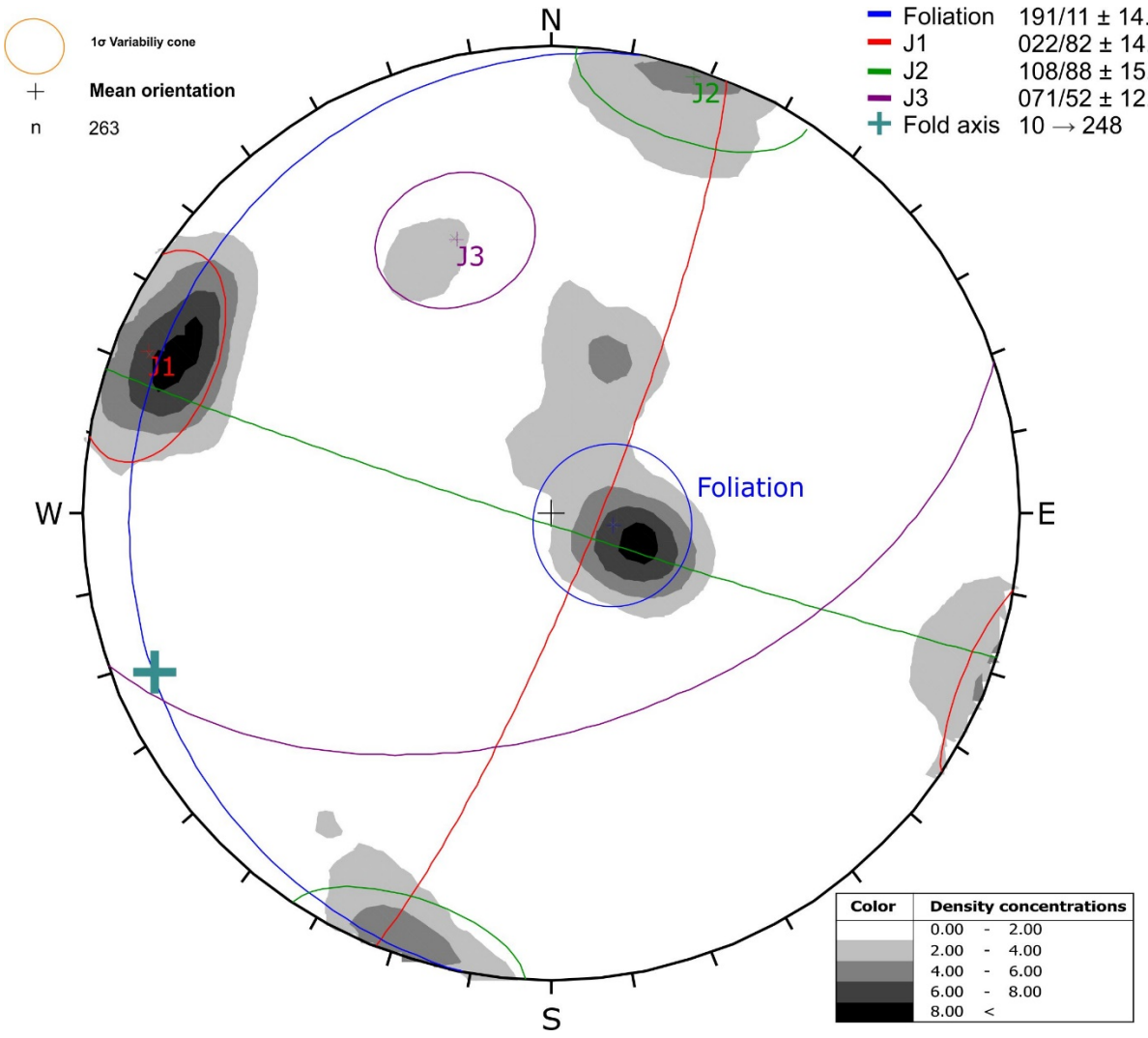

Figure 17 Stereonet displaying contours of discontinuities poles and assigned sets from MF2.

4.1.2.1 Photogrammetry

The 3D model produced for this study was based on the images acquired in the field campaign in September 2018 (Figure 18). The point density is 2770 points per m^2 and further details on the 3D model are found in Appendix C.

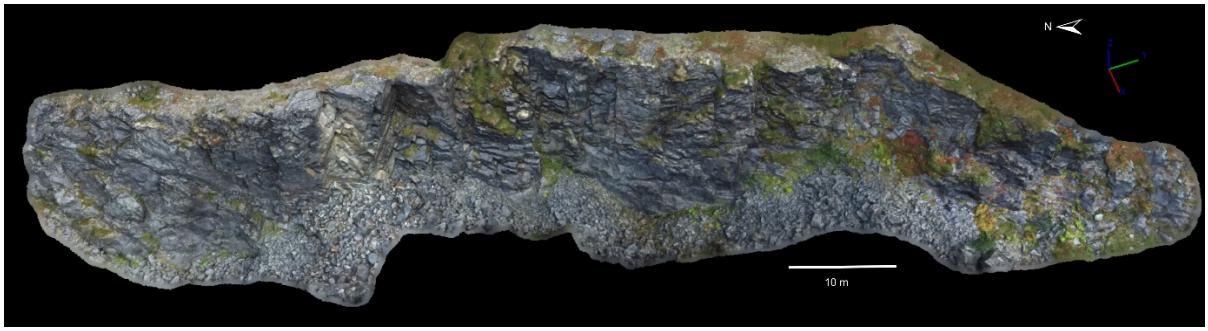

Figure 18 3D model of the back-scarp at MF2.

4.1.2.2 Coltop3D

The model shows two distinct steep joint sets and structural measurements were obtained from the known surfaces. The NS trending J1 is represented with yellow and green colors (002°/72°±11.1°) and the east-west trending J2 is represented with turquoise and pink colors (291°/88°±10.8°; Figure 19). J3 is not observed at this outcrop. The foliation data obtained (155°/22°±12.7°) was on average up to 11° steeper than the measured field average (183°/11°±14.3°). The structural data obtained from Coltop3D have similar orientations as the data measured in field (Figure 20 and Table 1).

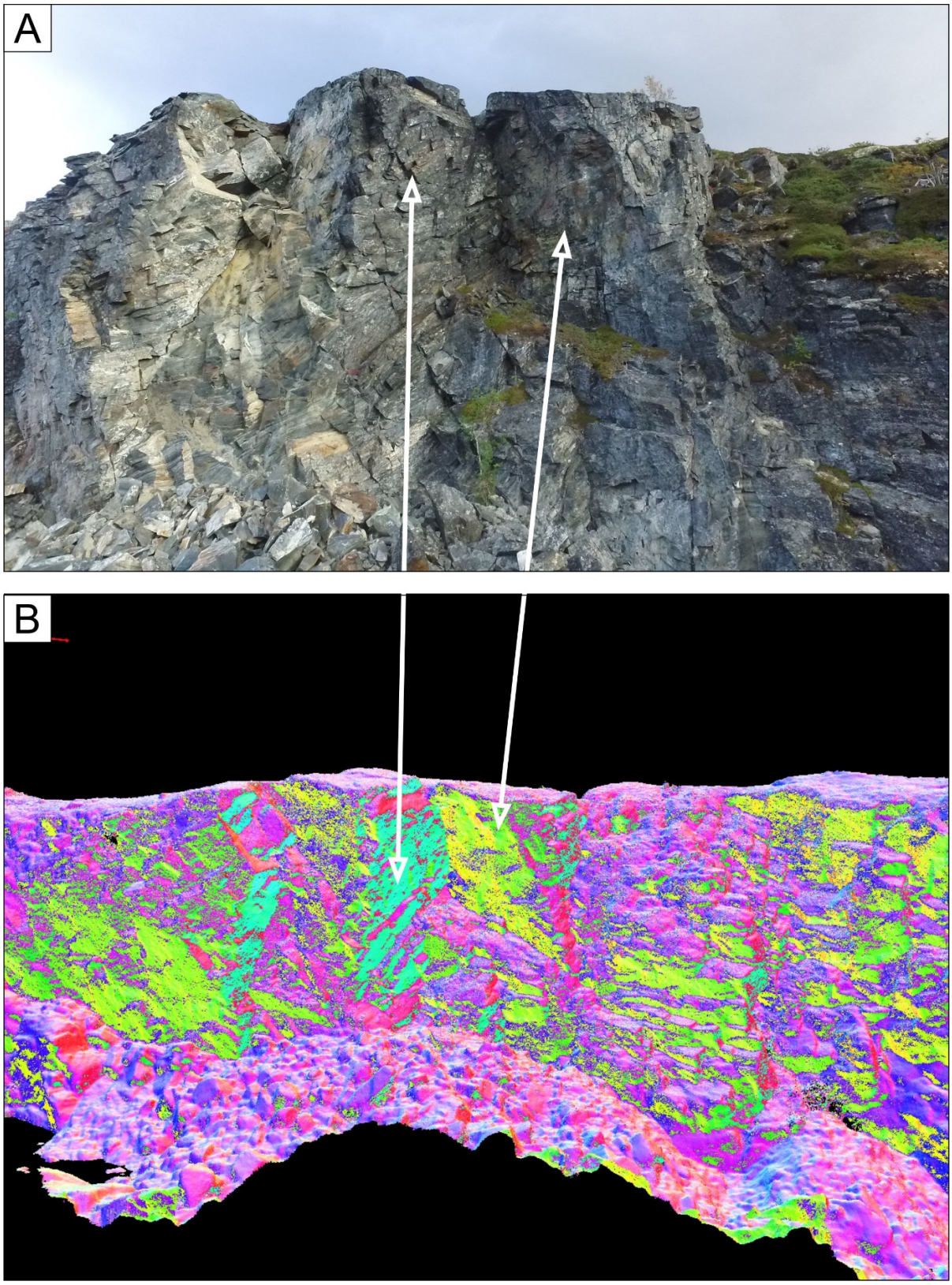

Figure 19 Coltop3D visualization. The model focuses on the recent rock-fall area visible in A that will be described in 4.3. The model looks northeast following the intersection between J1 and J2.

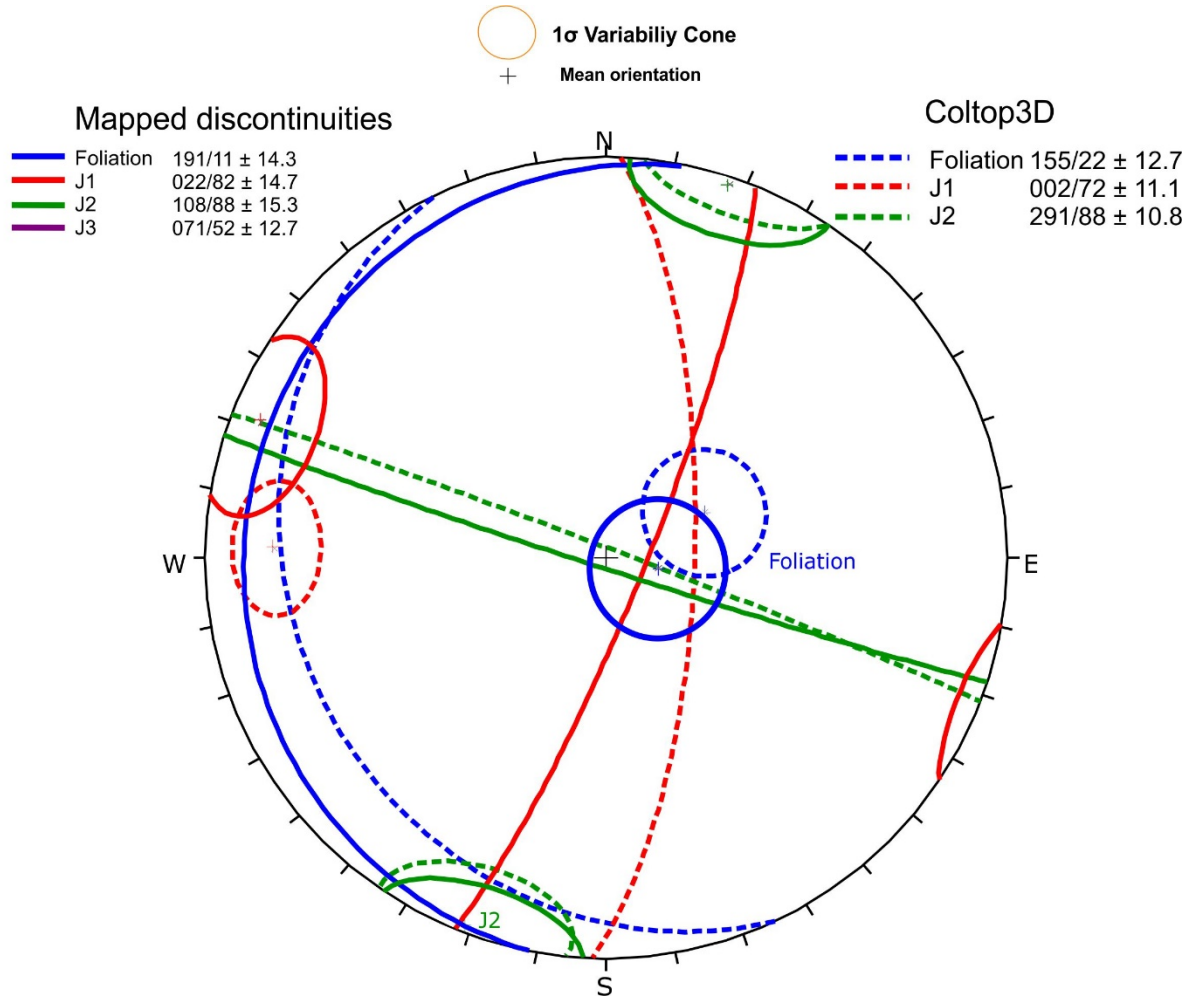

Figure 20 Structural data obtained from Coltop3D compared to mapped discontinuities at MF2.

4.1.3 Discontinuity sets

This section presents the discontinuities (Table 1 and Table 2). The structural data obtained from the photogrammetry analysis is included for easy comparison with the field data.

Table 1 Overview of joint orientation and measured fold axes in the two domains. Data obtained from Coltop3D in bold (Figure 20) and estimated fold axis in cursive.

Domain	Foliation	J1	J2	J3	Fold Axis
MF1	169°/15°±18.9°	029°/72°±16. 3°	286°/83°±21.8°	075°/67°±12.3°	20°→245°, 15°→ 255°, 21°→ 236°, *14°→ 235°*
MF2	183°/11°±14.3° **155°/22°±12.7°**	022°/82°±14.7° **002°/72°±11.1°**	108°/88°±15.3° **291°/88°±10.8°**	071°/52°±12.7°	23°→282°, *10°→ 248°*

Spacing, roughness and persistence are parameters that vary greatly across the field area. The overall fold axis estimated from MF1 and MF2 is 13° → 237°.

Table 2 Spacing, roughness, persistence, coating and iron staining based on field observations.

Set	Spacing [m]	Roughness	Persistence [m]	Coating	Iron Staining
Foliation	0.02 – 1.5	Planar smooth	-	-	Yes
J1	0.15 – 5	Planar rough to undulating rough	0.2 – 50+	Yellowish-white – up to 2mm	Yes
J2	0.1 – 3	Planar smooth to undulating rough	0.2 – 30+	Yellowish-white	Yes
J3	0.1 - 2	Planar rough to undulating stepped	1 – 30+	Yellowish-white	Yes

4.1.3.1 Foliation

The bedrock of Mellomfjellet hosts a persistent foliation. The mean orientation is 169°/15°±18.9° for MF1 and 183°/11°±14.3° for MF2, which is a gentle downslope direction. The standard deviation (σ) is high due to folding of the foliation (Figure 21A). The foliation is gently folded with a fold opening of ± 20° with a wavelength (λ) of 5 m. The fold axis plunge 10-20° downslope (Table 1). The degree of folding varies across the investigated area.

The observed roughness is planar smooth which is the smoothest set observed at Mellomfjellet. Iron staining is found at some of the surfaces.

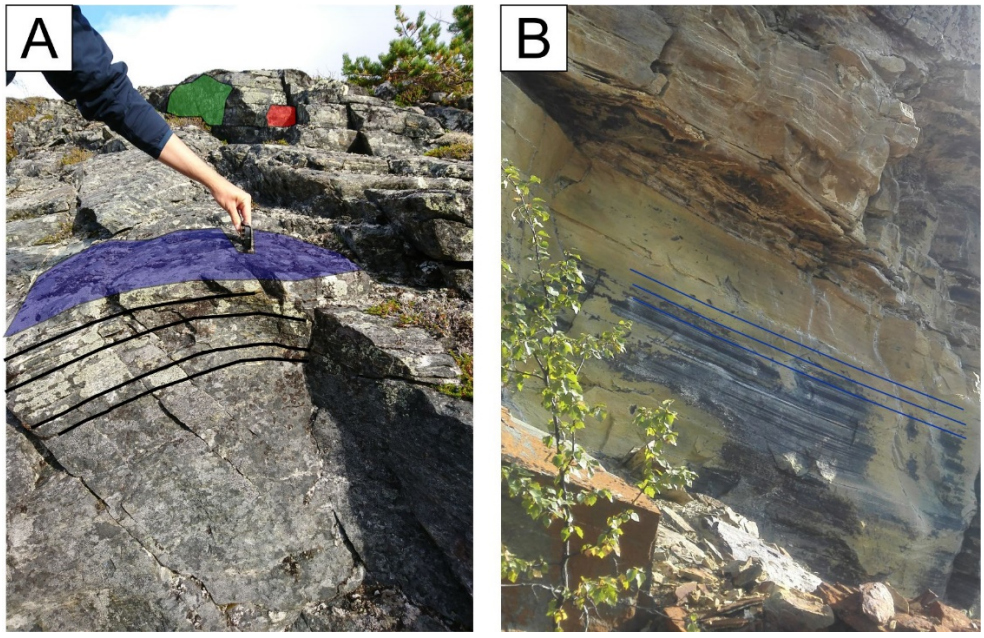

Figure 21 Photos showing the foliation at Mellomfjellet. A – Folding of the foliation at station 6. Foliation in blue, J1 in red and J2 in green. Picture looking east. B – Interlayered black and white mineral display foliation.

4.1.3.2 Joint set 1

J1 is steeply dipping to near-vertical and strikes NNE – SSW (029°/72°±16. 3°, 022°/82°±14.7° and **002°/72°±11.1°**). It is the dominant structure along with J2 and the foliation forming the back-scarp at MF1 and MF2 (Figure 22A and B). The joint set dips into the slope with an average of 72°. The surfaces display varying roughness from planar rough to undulating rough. The spacing varies from fifteen centimeters to several meters. Iron staining is observed as well as white to yellow coating up to 2 mm thick. The persistence is observed to be >50 m at MF2 (Figure 23).

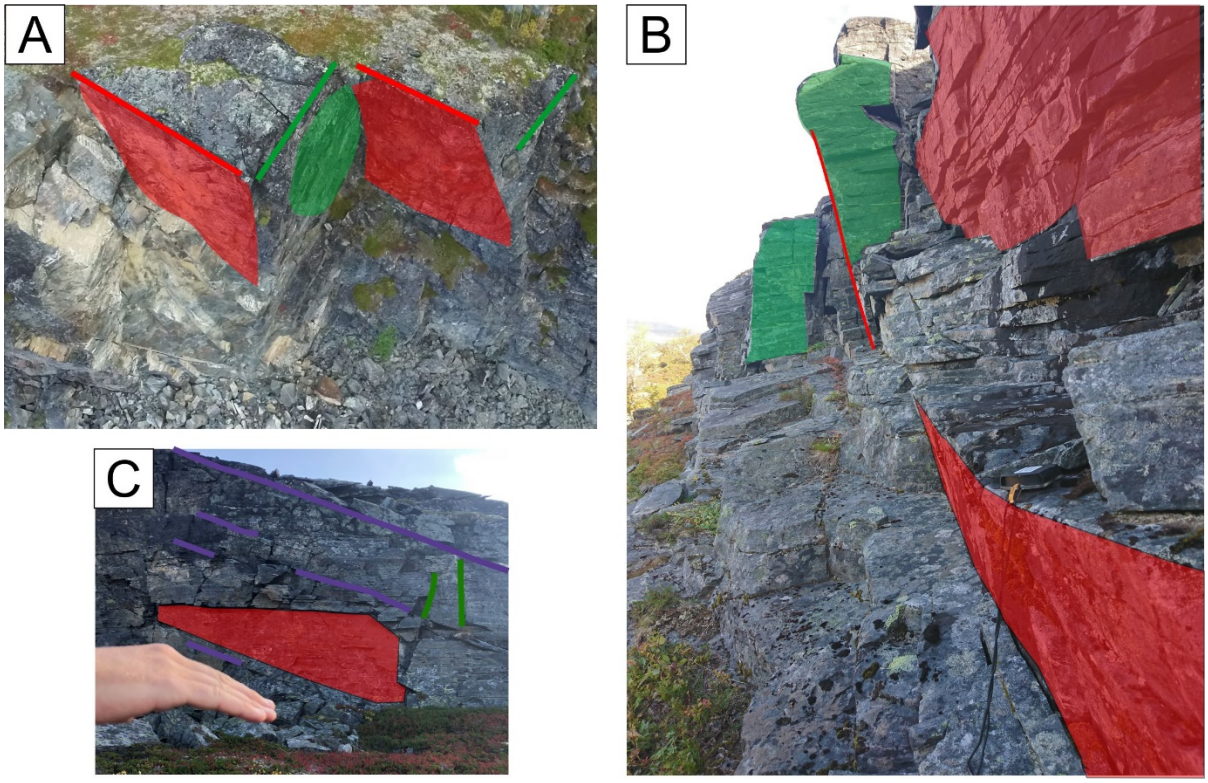

Figure 22 J1 - red, J2 - green and J3 - purple. A - Birdseye view of the MF2 back-scarp which is made up of J1 and J2.Photo looking NE. B – J1 dipping into the slope at the back-scarp. Photo taken towards north. C – Figure facing east towards the back-scarp at MF2 displaying the interaction of the joint sets. J2 shows great variability in dip.

4.1.3.3 Joint set 2

J2 is trending WNW – ESE and is steeply dipping (286°/83°±21.8, 108°/88°±15.3° and **291°/88°±10.8°**; Figure 22 and Figure 23). The persistence is observed to be very high (>30 m). Mineral coating and presence of iron staining is observed (Table 2). J2 is the most varying joint set with a variability cone of 21.2° in MF1. This has its origin from the spatial variation in the northwards and southwards dipping discontinuities.

Figure 23 J1 – red and J2 – green. Display the persistence of J1 and the interaction between J1 and J2 at the back-scarp. Photo looking east and author for scale.

4.1.3.4 Joint set 3

J3 is encountered at several of the field stations near the east west trending morphological depressions at MF1 and MF2 (Figure 32). It was well documented in the field as an E – W striking gentle dipping joint set (075°/67°±12.3° and 071°/52°±12.7°; Figure 24). However, it is not observed in the Coltop3D analysis and it is not statistically significant according to the dips structural analysis. It is the gentlest dipping joint set and it is slightly steeper at MF1 than at MF2 (Table 1 and Figure 24).

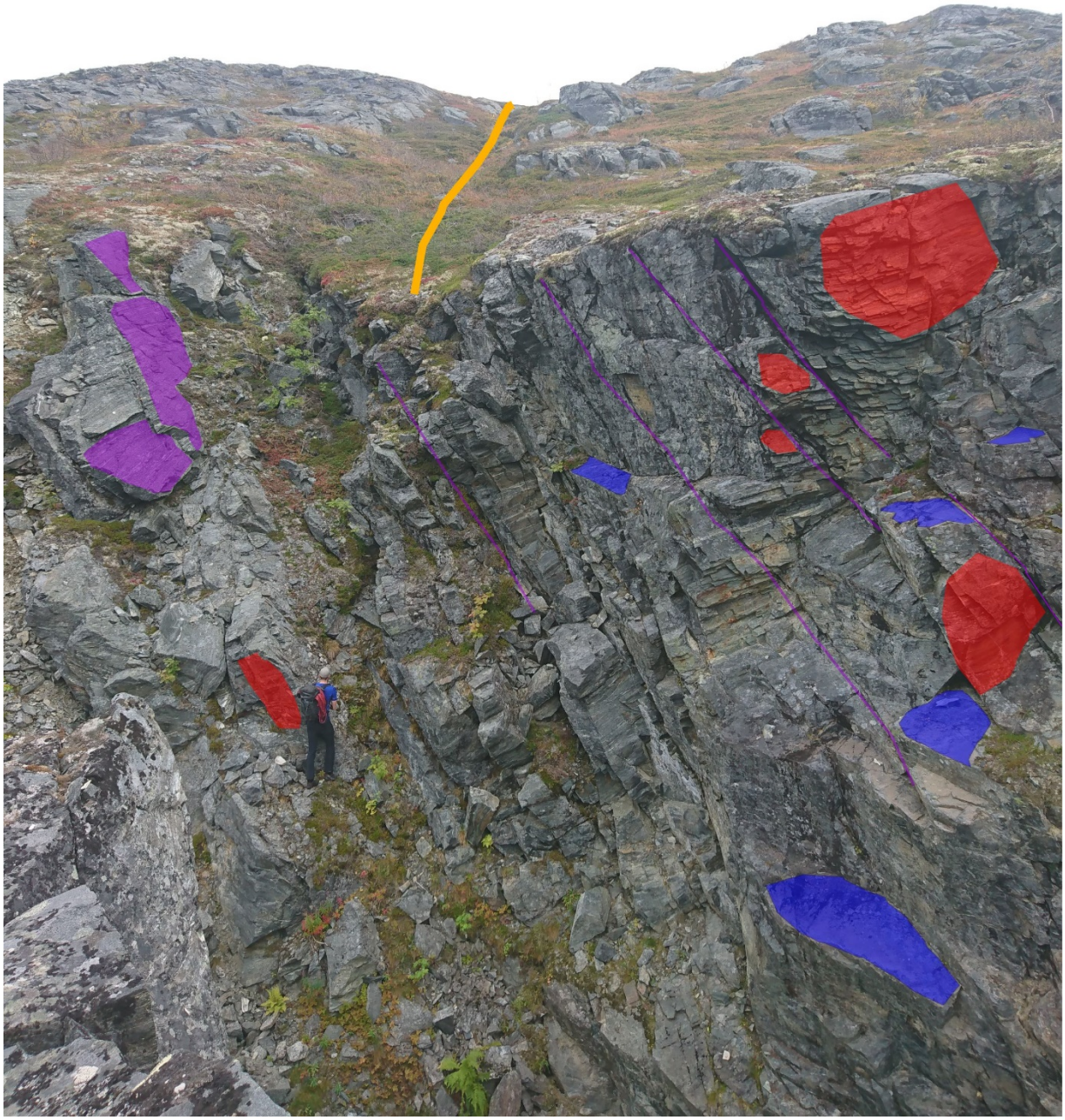

Figure 24 Foliation in blue, J1 in red, J3 in purple. Picture taken north of station 7 towards east. The orange line indicating a morphological depression. Author for scale.

4.1.3.5 Felsic intrusion

A layer of a light colored rock parallel to foliation is observed at station 20 (Figure 25). The layer outcrops at the base of the lowermost block at MF1. It is roughly 0.4 m thick with an average downslope dip of 30°. It stretches >100 m northwards from station 20 and beyond the

unstable rock slope of MF1 in the south. There is observed yellow/orange iron staining/coating on the joint surfaces below the zone. Figure 25C display a more pronounced foliation in the rock below towards the layer and continuation of the foliation in the light colored layer. In addition to the planar fabric, the layer hosts chaotic folded structures as well as loose clay/silt material. The mineralogical composition will be presented in section 4.2.

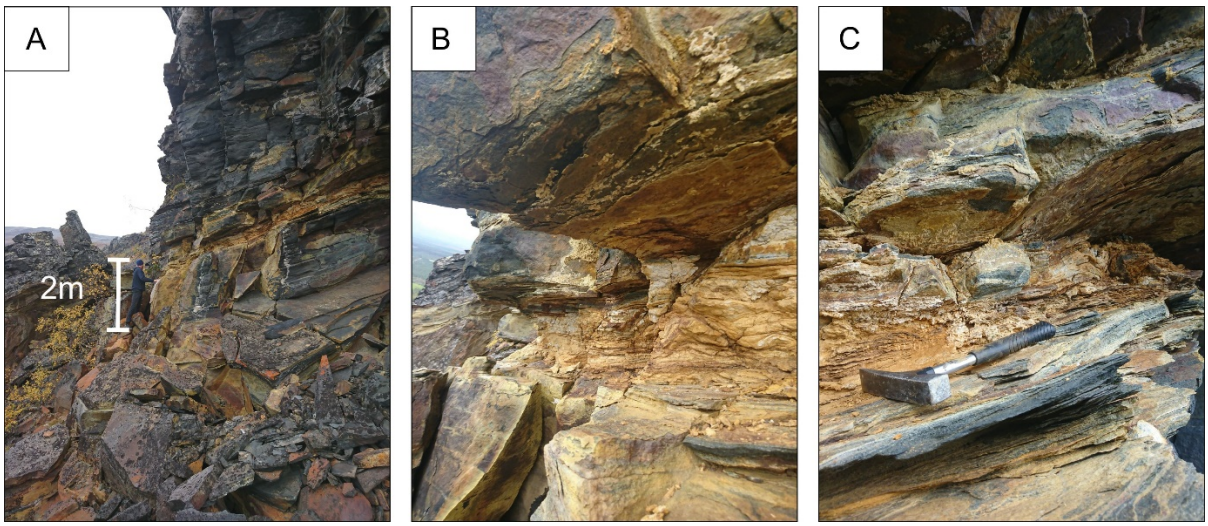

Figure 25 Pictures of the felsic intrusion. A – Displaying that the layer is foliation-parallel. Photo taken towards north. B – Displaying the iron staining and leeching of minerals. C – Shearing texture in the layer and the surrounding rock. Hammer for scale.

4.1.4 Kinematic analysis

4.1.4.1 Mellomfjellet 1

The kinematic analysis at MF1 was analyzed for the average strike of the slope (170°) and using an average of a steep area in the slope (64°; Figure 26). The greatest uncertainty in the kinematic analysis are connected with the friction value (20°) as it limits the feasibility for both planar- and wedge-sliding. The average foliation is not a feasible failure mechanism for planar sliding, as it is gentler dipping than the friction value. However, the foliation variability cone falls within the critical zone for planar sliding. Wedge sliding is also not feasible based on the average orientations of the discontinuities. However, 18.6% if the intersections between discontinuities is located in the critical area for wedge sliding. The critical intersection origin from the intersection between the foliation and J2 and the foliation and J3 (Table 3). Flexural toppling is a partly possible failure mechanism as J1 is located between the 30° and 45° lateral limit (Figure 26).

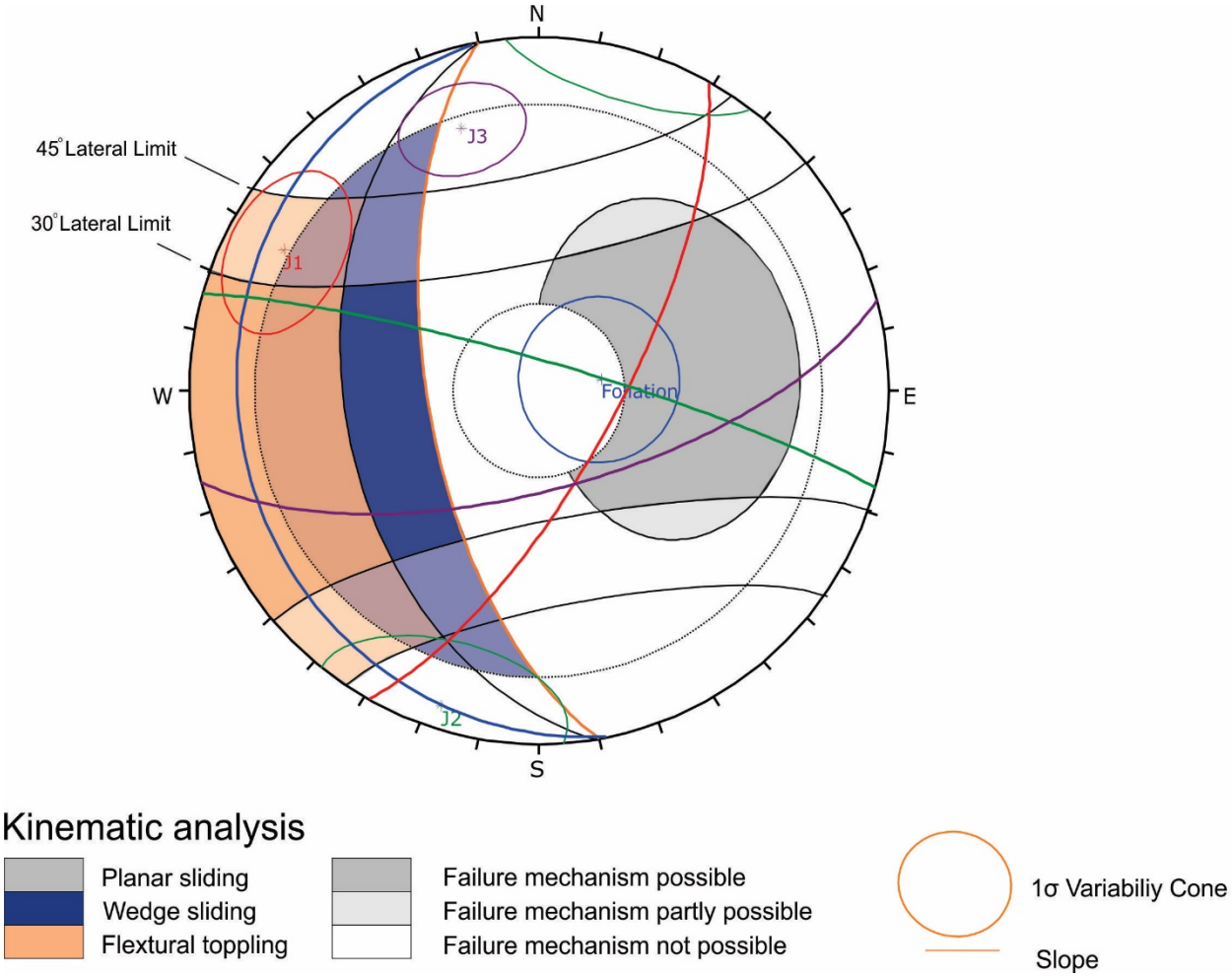

Figure 26 The kinematic analysis at MF1. The foliation is not steep enough to intersect in the critical area for wedge sliding. Parts of the foliation are located in the critical area for planar sliding.

Table 3 Kinematic analysis data from the analysis at MF1.

Mellomfjellet 1 (170°/64°)			
Failure Mechanism	**Intersections**		
	Total	**Critical**	**Percent Critical [%]**
Planar Sliding (All)	313	54	17.25
Planar Sliding (Foliation)	79	35	44.3
Wedge sliding	48819	9156	18.75
Flexural Toppling	313	62	19.81
Flexural Toppling (J1)	45	28	62.22

4.1.4.2 Mellomfjellet 2

The kinematic analysis at MF2 was analyzed for the average strike of 200° and for the slope dip of 72°. The used friction value is 20° and the lateral limits are 30°. Flexural toppling is a possible failure mechanism as J1 is located within the critical zone (Figure 27). As for MF1, the friction value governs the feasibility for the planar sliding. The average foliation is not feasible for planar sliding, but 29% of the measured foliations falls within the critical zone for planar sliding (Figure 27 and Table 4). The same applies for wedge sliding as none of the great circles intersects in the critical area for wedge sliding. Variations within the foliation measurements allows for 12% of the intersections falls within the critical area for wedge sliding (Table 4).

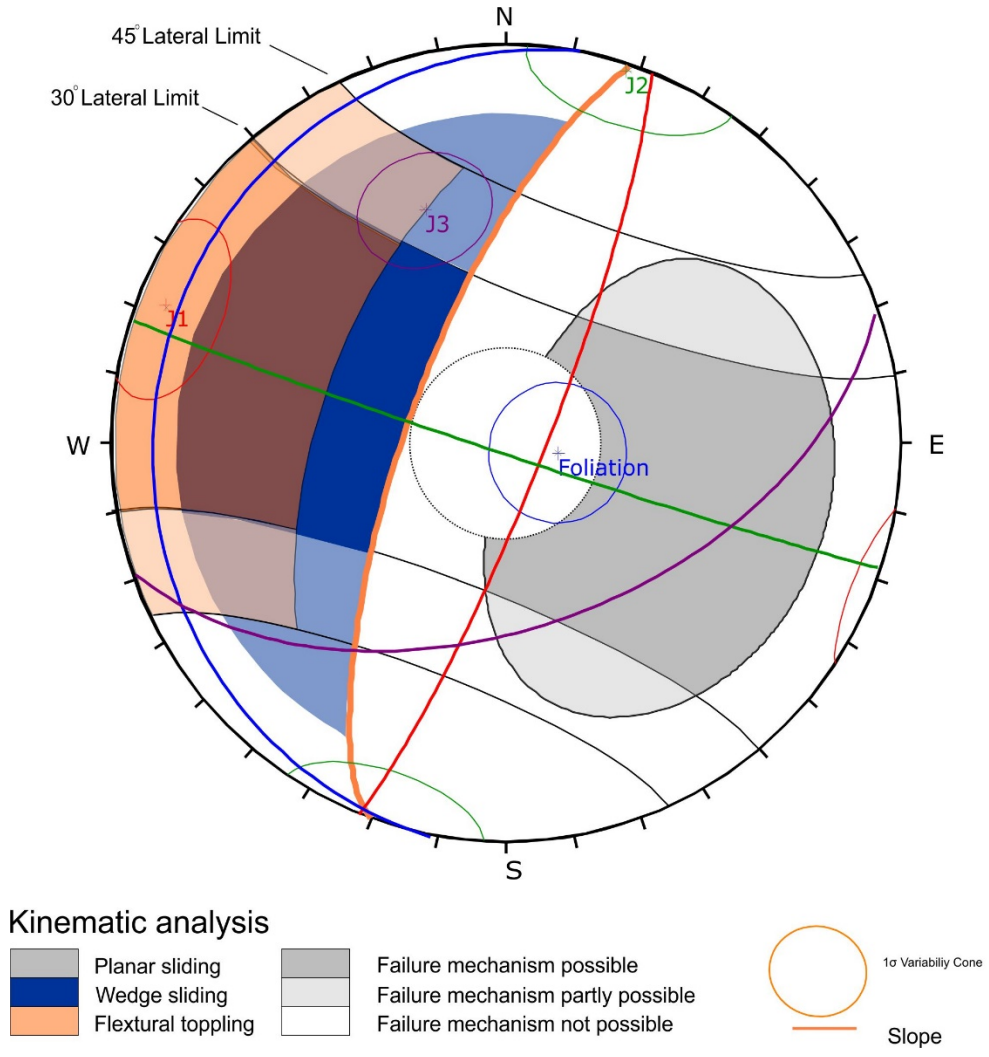

Figure 27 Kinematic analysis at MF2. J1 is fully enclosed in the possible failure mechanism for flexural toppling. Foliation dips to gentle to intersect with other joint sets in the critical area for wedge sliding.

Table 4 Kinematic analysis data from MF2. Obtained from Dips.

Mellomfjellet 2 (200°/72°)			
Failure Mechanism	**Intersections**		
	Total	**Critical**	**Percent Critical [%]**
Planar Sliding (All)	205	18	8.78
Planar Sliding (Foliation)	47	14	29.79
Wedge sliding	20900	2556	12.23
Flexural Toppling	205	49	23.9
Flexural Toppling (J1)	60	46	76.67

4.1.4.3 Field observation of failure mechanisms

Evidence of planar sliding was observed at MF1 (Figure 28). The fresh iron stained foliation surface observable Figure 28A has released blocks that is found in the immediate talus below (Figure 28B).

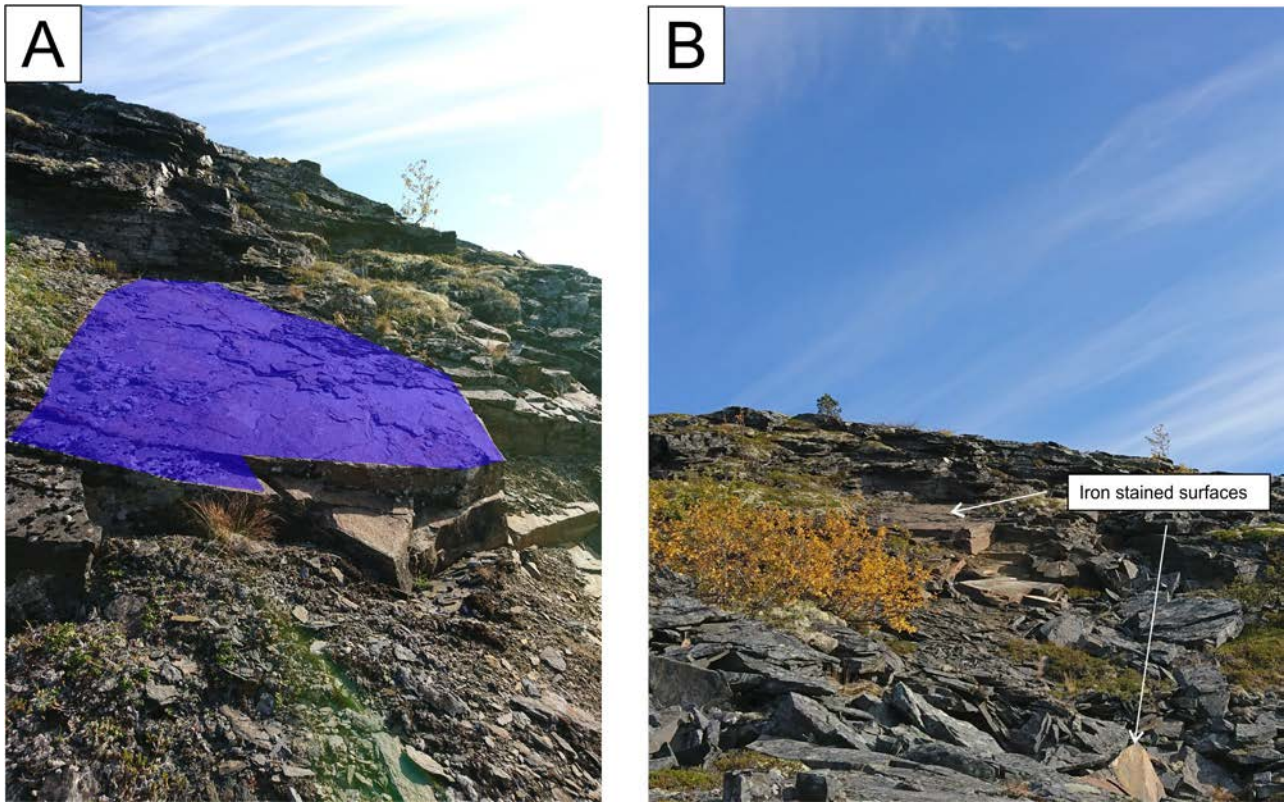

Figure 28 A – Planar sliding observed at MF1. Picture looking east-southeast. B – Fresh block with iron staining in the talus material from the planar sliding mechanism failure.

Toppling failure along J2 is observed in the field at the back-scarp of MF1 northeast of station 3 (Figure 29A). The local direction of the back-scarp puts J2 in the critical area for toppling failure in the kinematic analysis (Figure 26). In Figure 29B flexural toppling is evident along J1 at MF2.

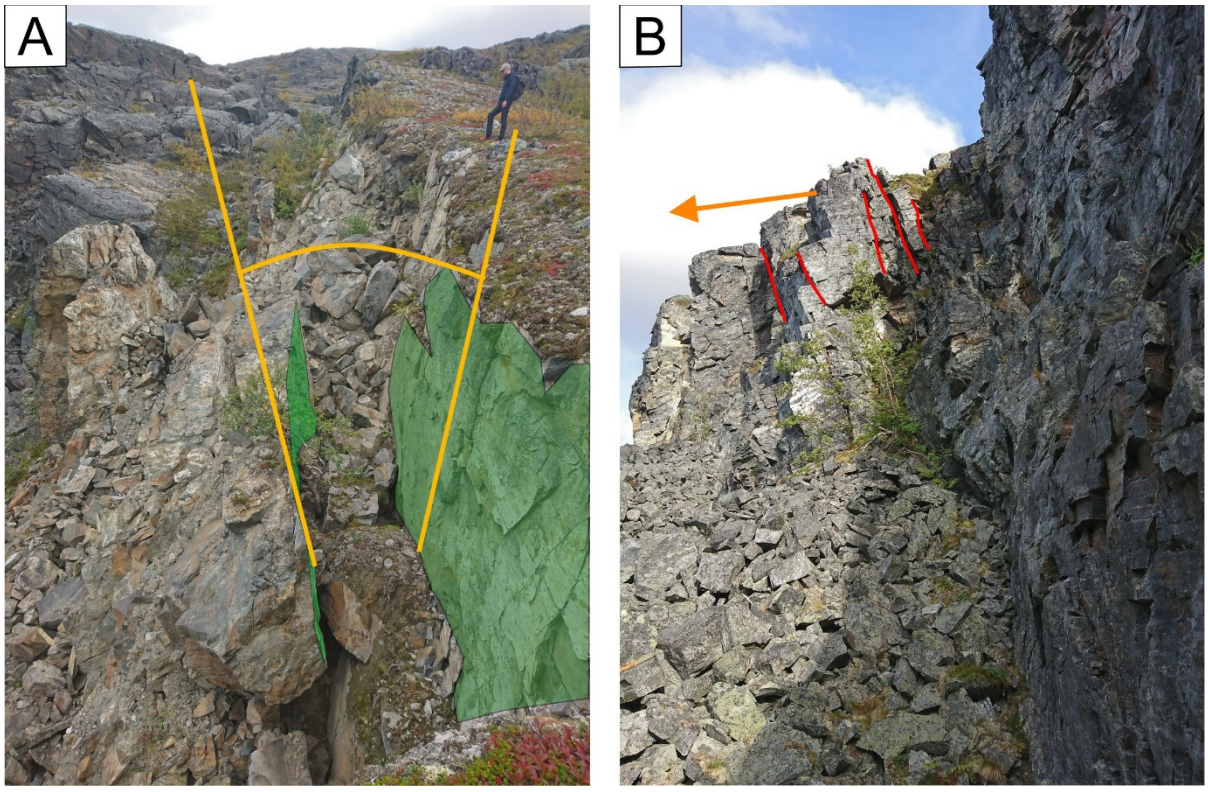

Figure 29 A – Toppling along J2 at back-scarp of MF1. Free hanging roots and loose sand in the ditch indicates quite recent activity. Picture towards east along J2. B – The structures allow for toppling in orange arrow direction from J1 (red) at the back-scarp of MF2. Picture towards north along back-scarp and J1.

4.2 Geological conditions

The 1:50 000-bedrock map presented in Figure 3 indicates two lithologies present at Mellomfjellet: amphibolite schist and calcitic marble. The 1:250 000 map indicated amphibolite and meta-diabase (Zwaan, 1988). Amphibolite and amphibolite schist were found, but no marble is found in the layer marked as marble in the geological map. There is a variation in how distinct the foliation is throughout the area from solid bedrock with few discontinuities to well-foliated rocks. The strength of the rock was observed by assigning a GSI-value following the method presented in Marinos and Hoek (2000) to the bedrock at a handful of the

stations. The rock mass varied from blocky or massive to blocky, and surface conditions from very good to good which led to a GSI-range of 60 to 80.

Thin section analyses of the main bedrock displayed presence of amphibolite (Figure 30A). The mineral composition was amphibole (70%), feldspar, zoisite and garnet. The felsic intrusion is comprised of feldspar, quartz, biotite and sulphides (Figure 30B). Thin-sections evidence of late-stage deformation with minerals dissected by quartz veins, and heavy weathering. SEM-analysis of the felsic material showed clay crystallography from physical structure and chemical signals (Figure 31). The geological setting and the implications related to the instability will be discussed in chapter 5.

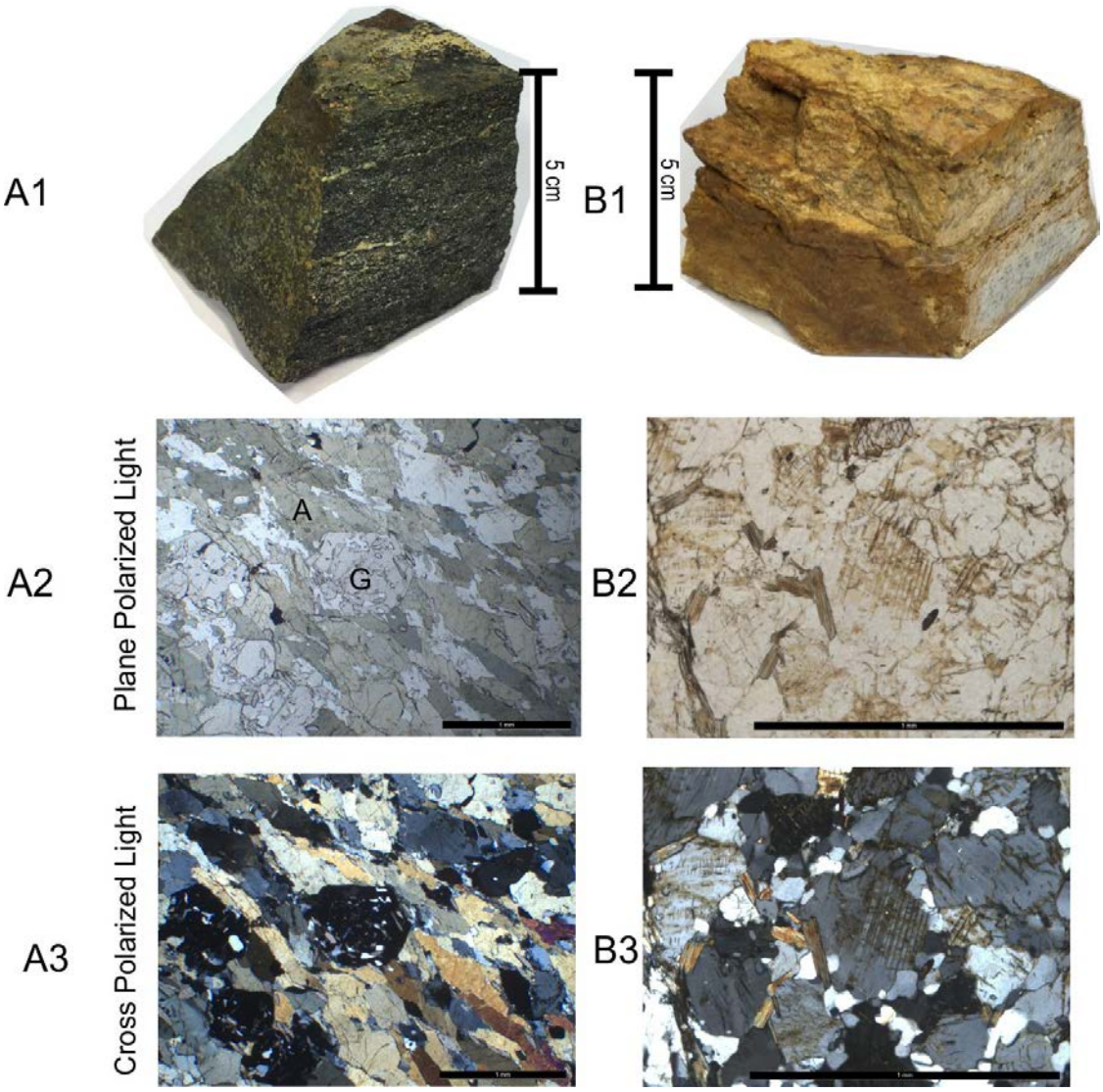

Figure 30 The bedrock of Mellomfjellet comprise of two lithologies represented in A and B. Scale is the black bar at 1 mm length. A1 – represent the amphibolite in hand-sample, A2 – thin section of the sample in plane polarized light, A3 – same orientation of the sample with cross polarized light. B1 – Hand sample of the felsic intrusion, B2 – felsic intrusion under plane polarized light and B3 felsic intrusion under cross-polarized light.

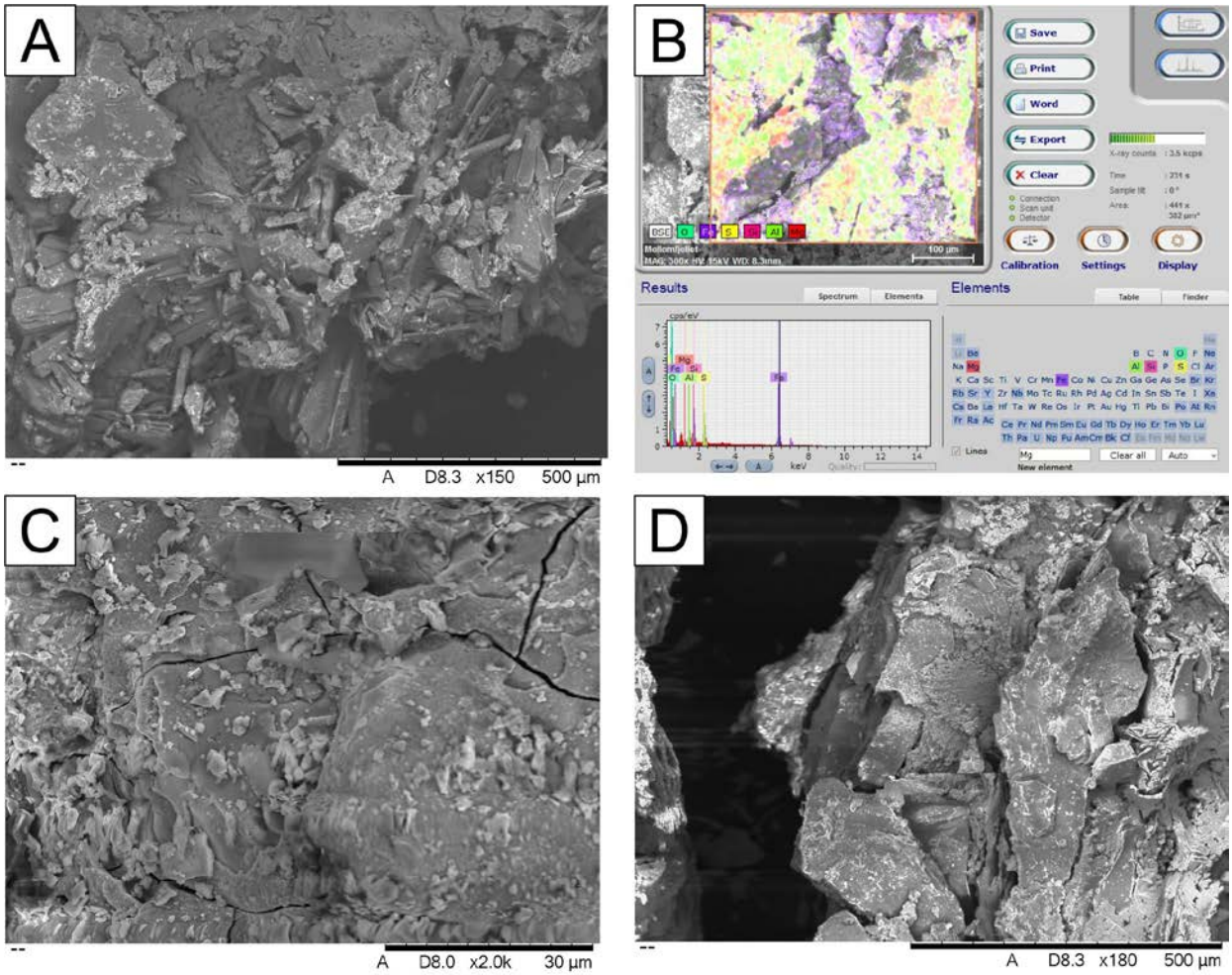

Figure 31 SEM-analysis of hand specimen from the felsic intrusion. A – Flaky texture observed in the SEM-microscope. B – Chemical signals from iron (Fe), magnesium (Mg), silicon (Si), Oxygen (O), sulfur (S) and Aluminum (Al). Chemical signal for typical clay aluminosilicates. C – Up-close picture, note the scale and the cracks. D – Flaky texture.

4.3 Geomorphology

A map displaying major lineaments and morphological and hydrogeological features is presented in Figure 32. The map uses symbols in accordance with NGU mapping procedure.

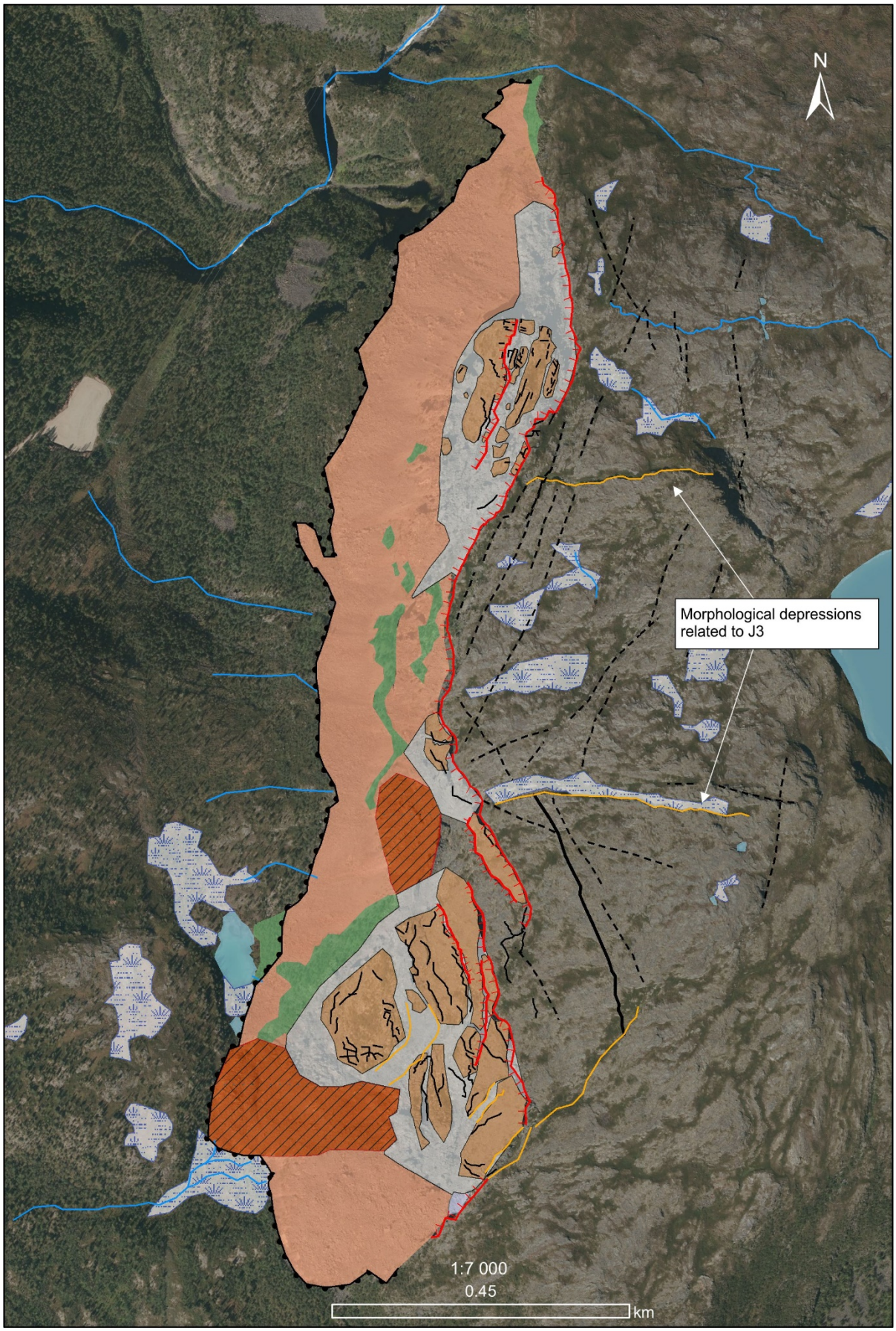
N
Morphological depressions related to J3
1:7 000
0.45
km

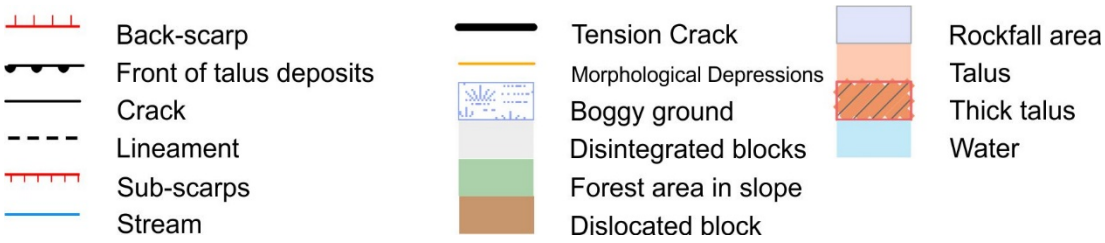

Figure 32 Map showing geomorphology and morphological structures as well as hydrogeological conditions.

4.3.1 Lobe-shaped talus

At the southern part of MF1, a lobe-shaped talus is observed (Figure 33). The front is over-steepened and recent rock falls are seen at the front. The frontal slope displays blocks along with gravel/sand that is iron stained (Figure 33C and D). Concentric ridges can be seen at the front of the northernmost lobe (Figure 33AB). The immediate ground in front of the over-steepened slope in Figure 33D display a lobe shaped feature. Trees growing on lobe-shaped feature are inclined (54°) and indicates rotation of the ground (Figure 33D).

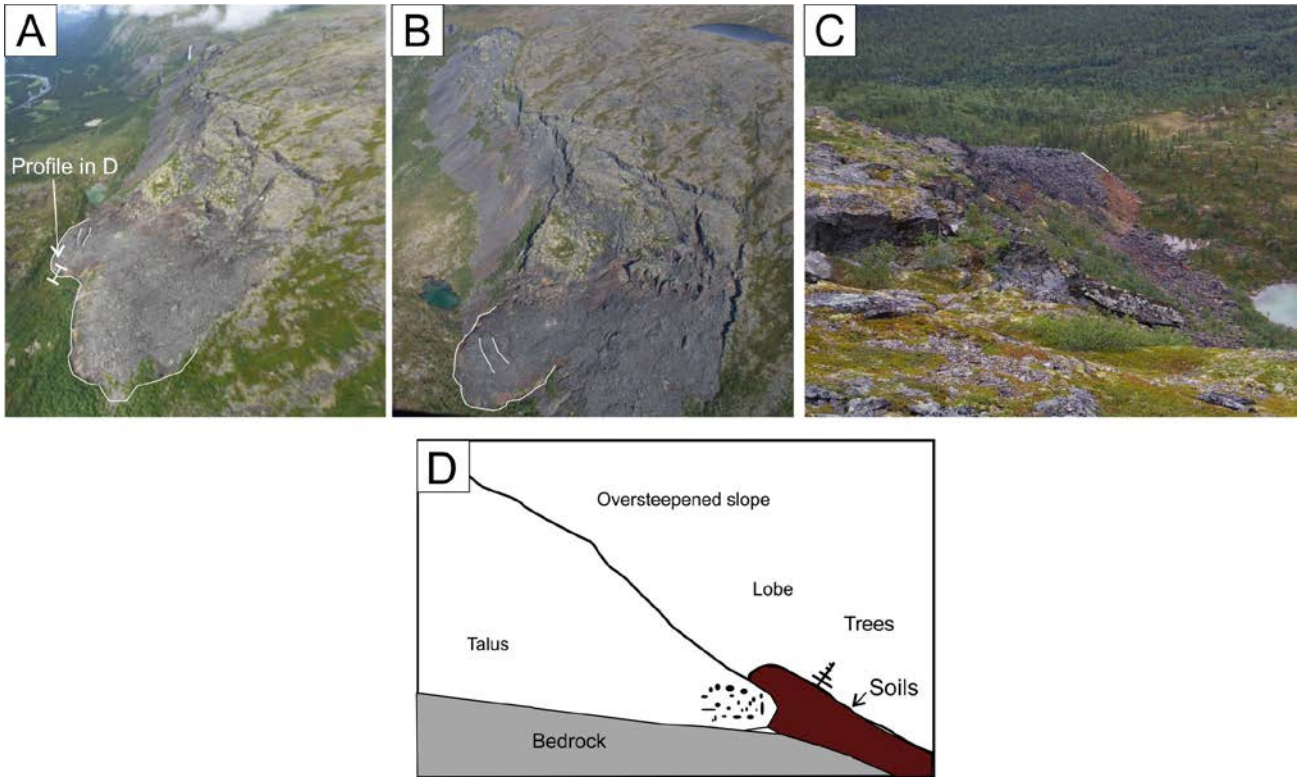

Figure 33 A – Lobe-shaped talus at MF1. B –Displays the flow like deposition of the lobe. C – The lobe seems to be progressing at the front. There are several recent rock-falls from the lobe and fresh surfaced blocks laying in the moss and heather. Iron stained rocks and loose material outcropping at the front of the lobe. D – Sketch of the immediate front of the lobe-shaped talus. The talus seem to push the soil and tilt the trees.

4.3.2 Back-scarp

The back-scarp at MF1 is defined by two scarps striking 025° and 345° that dip steeply towards the valley (Figure 32 and Figure 34). Opening along the back-scarp is observed for both striking directions. The back-scarp is made up of intersecting surfaces of foliation, J1 and J2. The two main segments of the back-scarps at MF1 do not connect and the back-scarp is therefore discontinuous. However, depressions connect the scarps and indicate developing conditions (Figure 34). The vertical displacement across the back-scarp is less than 10 m and the depth of the structures are uncertain due to blocks filling the trench and obscuring the surfaces.

The back-scarp at MF2 is fully developed. The overall strike of the back-scarp rotates from 025° in the south of the domain to 350° in the north of the domain. The back-scarp opens along a horizontal zigzagging pattern along J1, J2 and the foliation (Figure 22). The northernmost block displays little vertical displacement while the southernmost block indicates a vertical displacement of >10 m (Figure 34). The trench between the assumed in-situ bedrock and the northernmost blocks is up to 15 m wide and indicates horizontal displacement. Loose blocks in the trench introduce uncertainty on how the back-scarp propagates at depth.

A recent rock-fall was observed near station 10 from the back-scarp at MF2 (Figure 35). The fresh pale surfaces indicate newly exposed rock. A photograph from the 2009 NGU field campaign captured the back-scarp pre rock-fall and the 2018 campaign provided a photograph for comparison (Figure 35). The area was further investigated using photogrammetry.

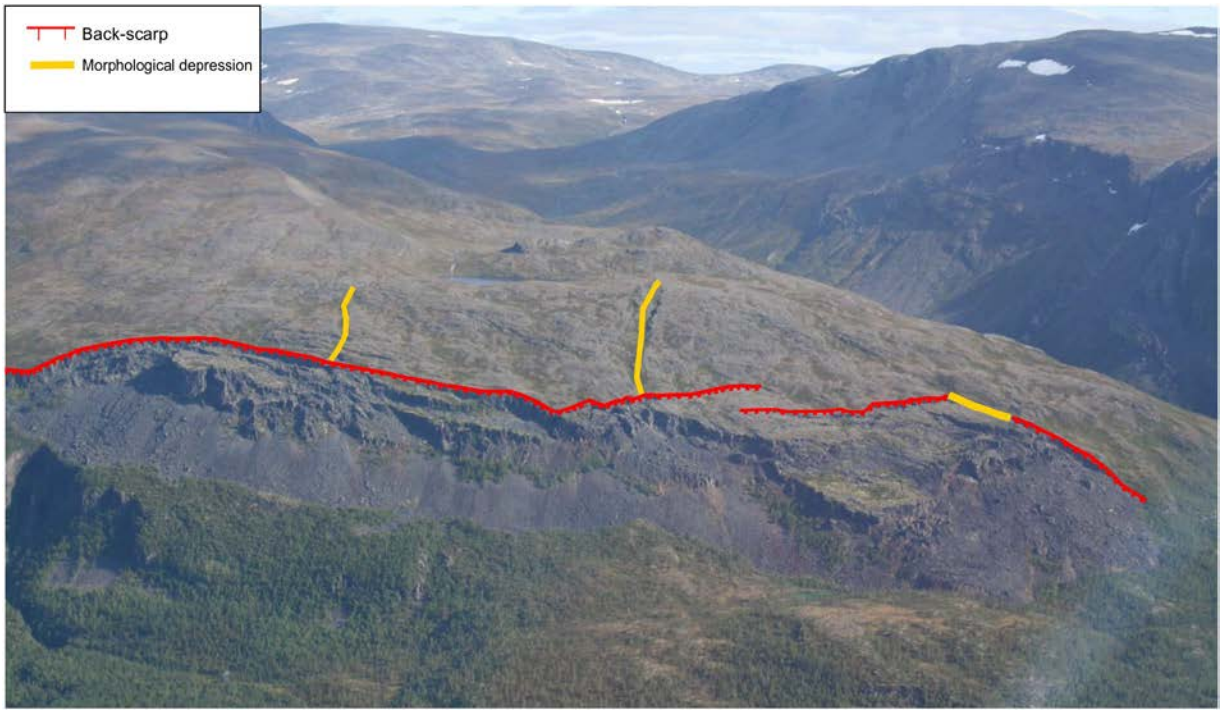

Figure 34 Aerial photo looking southeast at Mellomfjellet that display the continuous and discontinuous behavior of the back-scarp for MF2 and MF1 respectively.

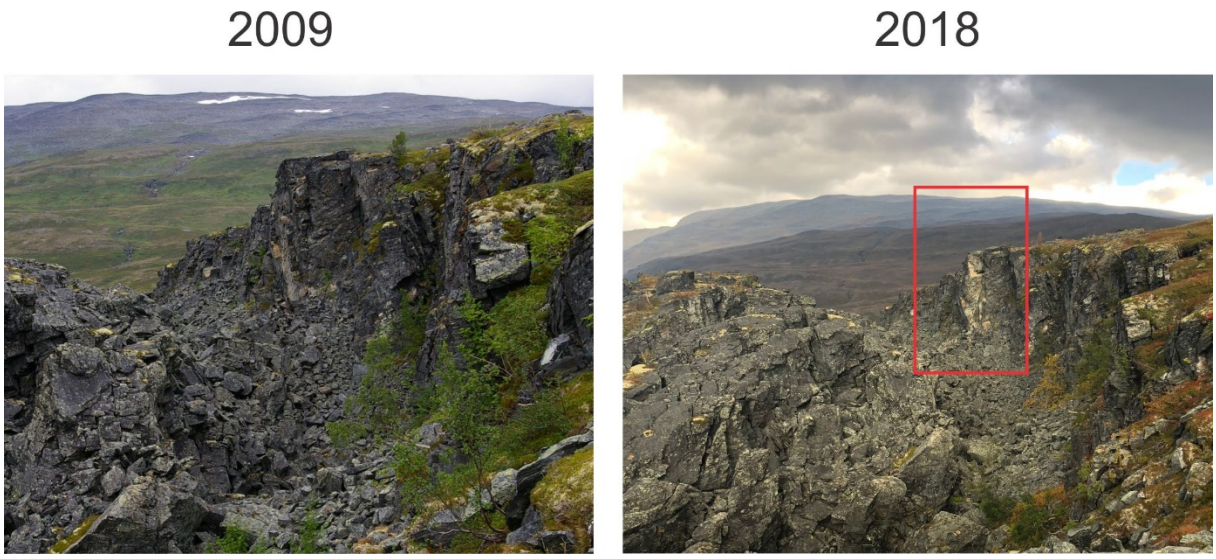

Figure 35 A recent rock-fall observed at the back-scarp at MF2. The release area is marked with the red rectangle. Bright colors indicate the fresh surfaces.

4.3.3 Tension crack

A tension crack is observed above MF1 that persists for >200 m horizontally (Figure 32 and Figure 36). The aperture ranges from cm to several meters and vertical displacement is not observed. The depth exceeds 30 m and the deepest parts are snow filled. The strike is parallel to the back-scarp and the tension crack walls consist of surfaces from J1, J2 and the foliation (Figure 36D).

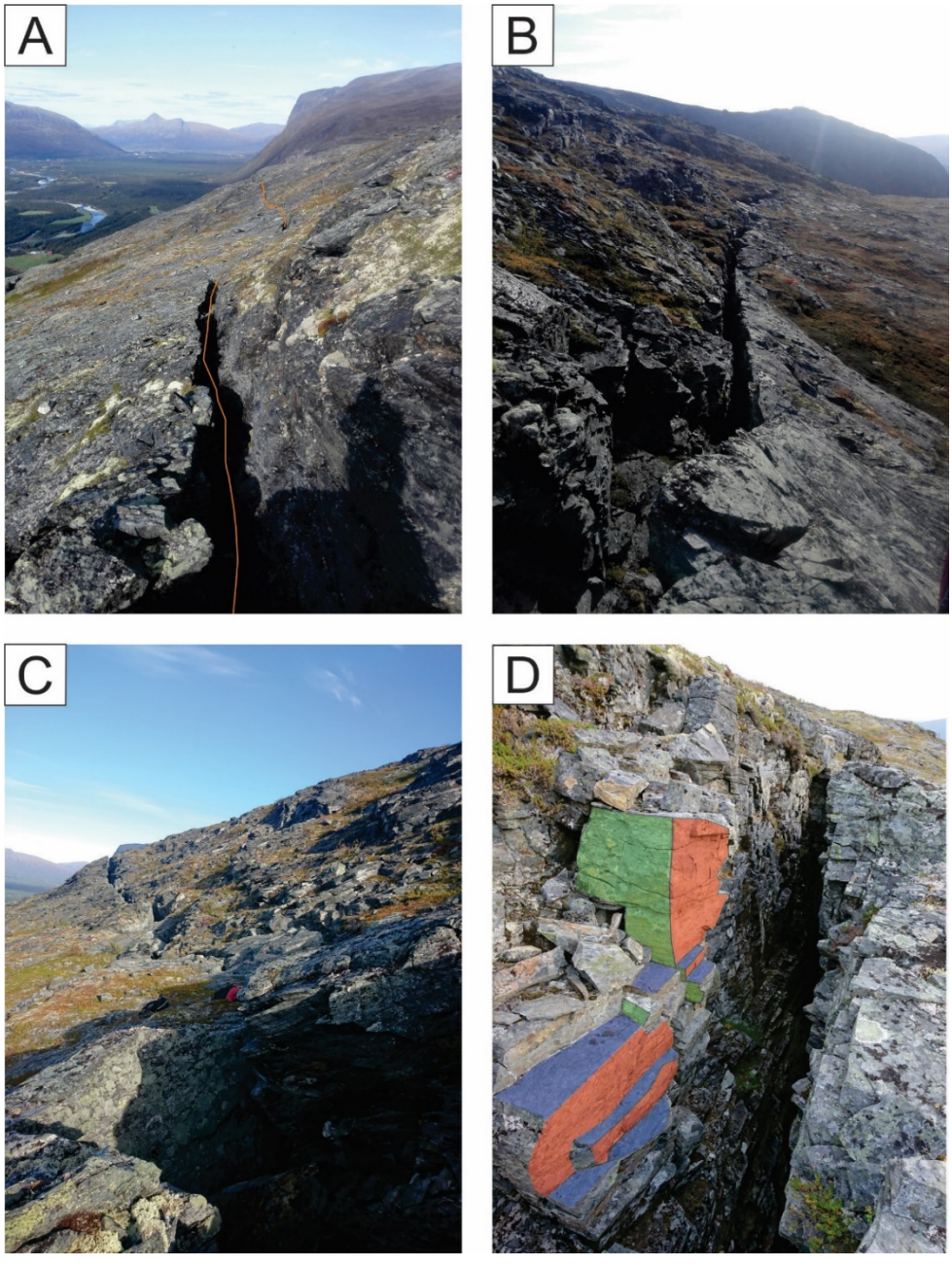

Figure 36 A - Displaying the tension crack trending northwards. B - South looking picture displaying tension and no vertical displacement. C – The tension crack persist through slope. Picture taken towards north. D - J1 in red, J2 in green and foliation in blue. The discontinuities make up the inclined back-scarp dipping into the slope.

4.3.4 Spatial distribution of displacement at MF1

The back-scarp and internal scarps at MF1 display difference in displacement along the scarps. The red lines in Figure 37 display how the scarps are more developed at one end than the other. The scarp to the left in Figure 37 display a vertical displacement of 2 m in the north and no vertical displacement in the south. The differential horizontal opening of the scarps indicate movement downslope in a generally clockwise direction.

Figure 37 Aerial photo looking southeast at MF1 displaying the spatial distribution of displacement.

4.4 Hydrogeological conditions

Water was observed in boggy ground above the back-scarp and in the streams coming out of the talus (Figure 32). Moist ground was observed within the sparsely forested area in the talus. There were a few streams observed above the unstable area. However, fieldwork was executed after some dry weeks and smaller streams may have been overlooked.

Snow filled cracks were observed within the unstable area as well as in the proximal tension crack. The temperature within the tension crack was low enough to create ice crystals on the rock walls of the crack. Deep open fractures combined with a complex fracture geometry and snow accumulation suggests that some sporadic permafrost can be expected.

4.5 InSAR results

4.5.1 Sentinel-1 data

The Sentinel-1 data was analyzed to find displacement patterns at Mellomfjellet (Figure 38). The displacements patterns are analyzed in combination with field observations to relate displacement with geological features (Figure 39). The geological features are delineated by polygons and displacement is averaged in each polygon (Figure 39). Polygon 1 – 3 are related to the blocks at MF2 and polygon 4 is located in assumed stable bedrock. Polygon 5 – 7 marks blocks at MF1 and polygon 8 is located west of the main tension crack.

The zonal statistics display variable rates of displacement depending on the location (Figure 39). The back-scarp controls the displacement where an increase in displacement from 0.26 mm/year in the assumed stable area of polygon 4 to - 1.2 mm/year (negative numbers mean downwards in the LOS) in polygon 2 at MF2. The same effect is seen at MF1 where polygon 8, above the back-scarp, shows a rate of -0.56 mm/year and polygon 7, the first block below the back-scarp, shows a displacement of - 1.4 mm/year.

There is a different displacement rate between polygon 1 (- 3.08 mm/year) and 2 (- 1.2 mm/year), showing individual blocks within the URS are moving separately. Polygons 1 and 2 (combined as Polygon 3) have the highest displacement rates, and form part of the worst-case scenario for MF2.

MF1 displays small displacement rates (< - 1.5 mm/year), except for polygon 5 (- 11.7 mm/year). An increase in displacement is observed between polygon 8 (- 0.58 mm/year), located in the area between the tension-crack and back-scarp at MF1, and the assumed stable area of polygon 4 (0.26 mm/year) at MF2.

The highest displacement rates observed in the Sentinel-1 analysis are located in the talus material directly below the blocks at MF1. The lack of point data in the talus area below may indicate high displacement rates.

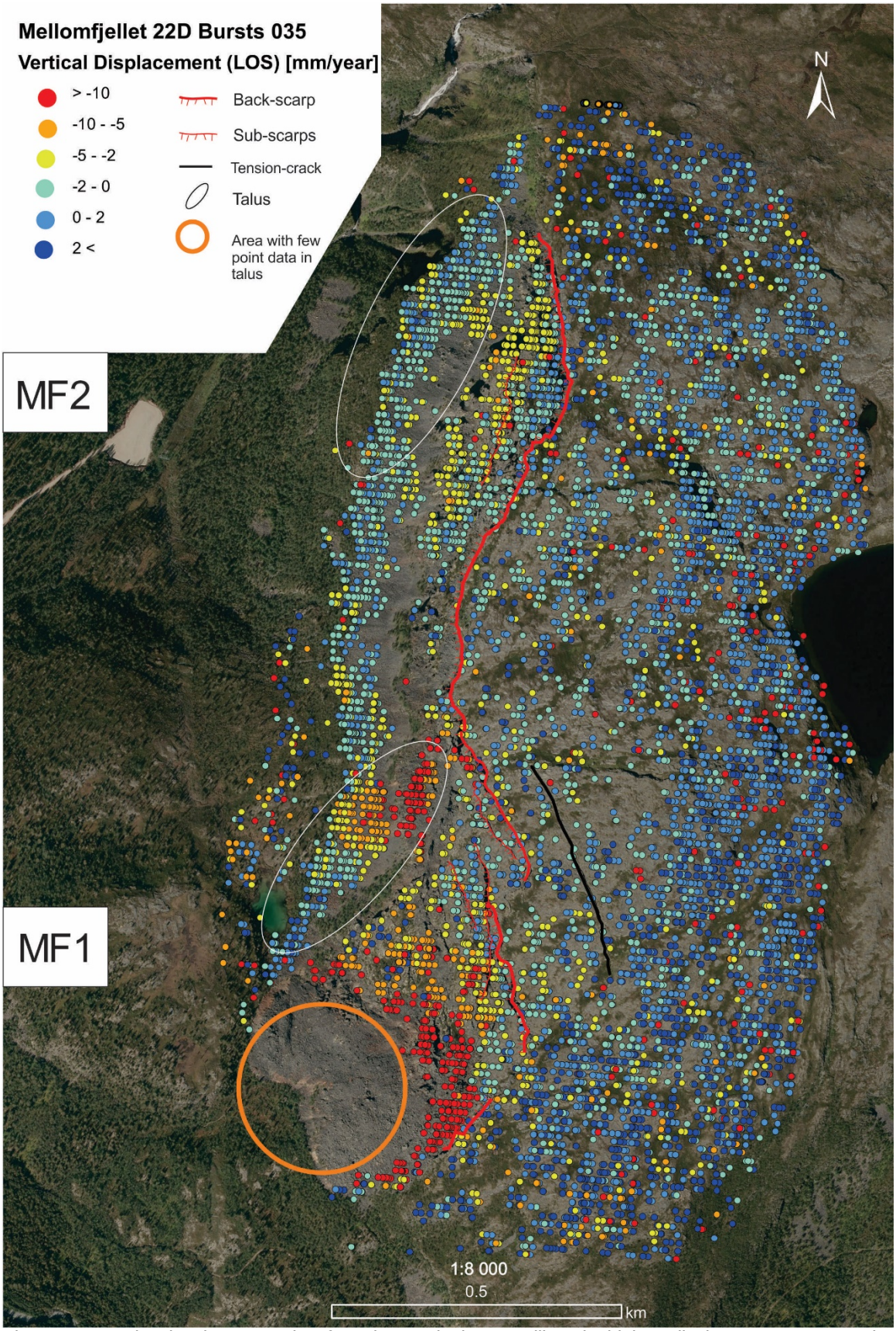

Figure 38 Map showing the InSAR data from the Sentinel – 1 satellite. The highest displacement rates are observed in the talus area at MF1.

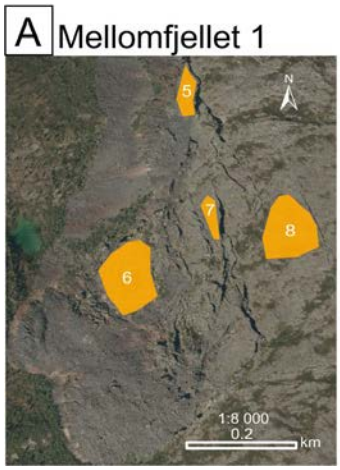

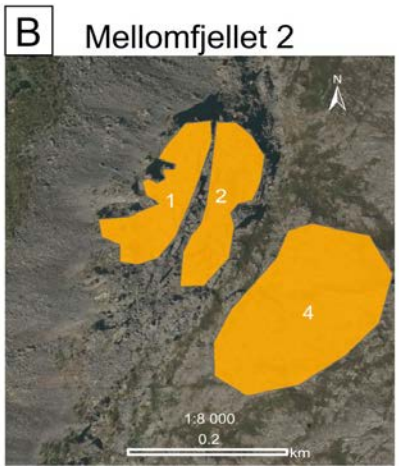

C

Polygon	Average velocity [mm/year]
1	-3.08
2	-1.2
1+2 = 3	-2.16
4	0.26
5	-11.7
6	-1.1
7	-1.4
8	-0.56

Figure 39 Zonal statistics of polygons surrounding blocks and assumed in-situ bedrock at Mellomfjellet (A and B). InSAR displacement displayed in mm/year (C). Negative values indicate movement away from the satellite (e.g. downwards within the LOS).

4.5.2 RSAT-2 data

The raster data from the RSAT-2 InSAR dataset is interpreted using four displacement profiles (Figure 40). The profiles strike over the key geological and morphological features used in the Sentinel-1 polygon analysis in an effort to compare the different datasets.

A – A' intersects the back-scarp and the unstable blocks at MF2. The displacement rate increases from - 0.3 mm/year in the in situ bedrock to - 2.5 mm/year in the main block and stable conditions are reached below the talus area.

B – B' is located over a smaller unstable block and talus area north in MF1. The highest velocity is found here, with up to 7 mm/year recorded.

C – C' crosses the main tension crack, back-scarp and blocks at MF1. The displacement is low close to the tension crack and is increasing up to 6 mm/year at the lowermost block. There is a color change from blue, east of the tension crack, to yellow at the back-scarp. The change is observed in C-C' as well.

D – D' is added to find the displacement rate in the assumed stable area. The displacement rate is roughly - 0.5 mm/year for the entire profile.

Blank spots in the InSAR-map might be due to large displacements, which are too high to be captured by the InSAR, or rapid changes in the surface expression from rock-fall processes.

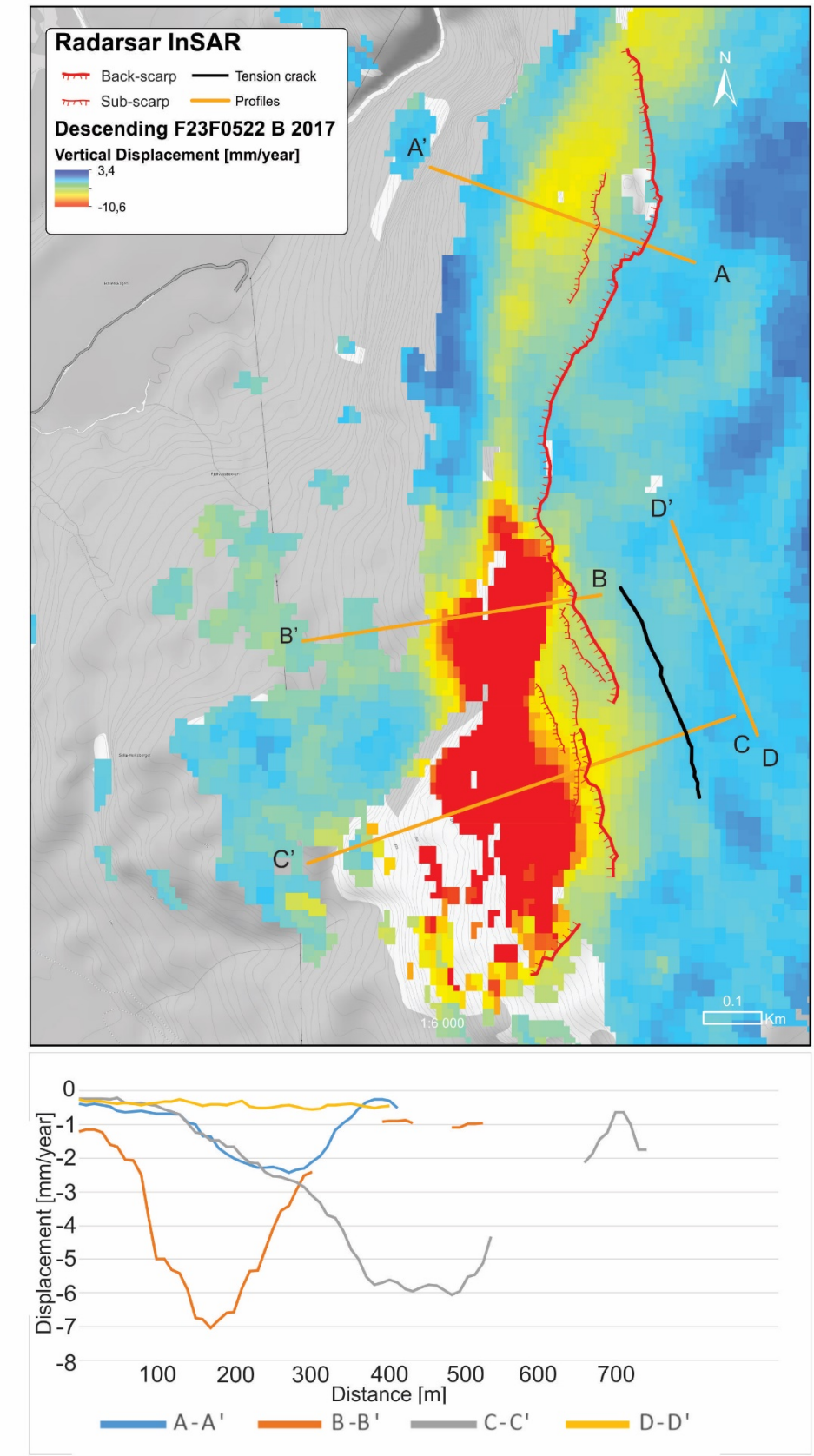

Figure 40 RSAT-2 data at Mellomfjellet. Displacement is displayed at different profiles through the area.

4.6 Scenario analysis

The scenarios presented are worst-case scenarios in order to find the maximum run-out from each domain. The scenarios are delineated by the back-scarp and include the blocks and some of the talus. A larger volume leads to a smaller angle of reach/longer runout to be used in the Flow-R analysis. The delineated scenarios are found in Appendix E.

The scenarios are analyzed with the aid of the NGU SLBL tool, which gives three different failure surfaces as basis for the analysis (Table 5). The angle of reach and run-out are based on the intermediate SLBL.

Table 5 Data from the scenario analyses at Mellomfjellet.

Scenario	Area [m2]	Estimated Volume [Mm3]			Angle of reach [°]	Run-out [m]
		Min. SLBL	Int. SLBL	Max. SLBL		
MF 1	113260	0.72	1.12	1.59	25.4	695
MF 2	159002	1.54	3.05	4.07	22.1	985

Flow-R run-out modelling results are presented in Figure 41. The run-out model at MF1 show a smaller run out distance than what is observed for MF2. There is a hill in front of the unstable rock slope (MF1) that limits the run-out and directs parts of the flow towards north. The flow stops close to the power line and does not threaten the nearby farms or the power line (Figure 41).

The run-out model for MF2 cross both the construction road and the power-line and Gæiraelva (Figure 41). The run-out approach the nearby farm and stops at the field's edge. Therefore, the

farm is not threatened by the run-out estimation. However, the newly built power-line and its access road is reached by the run-out analysis of the worst-case scenario.

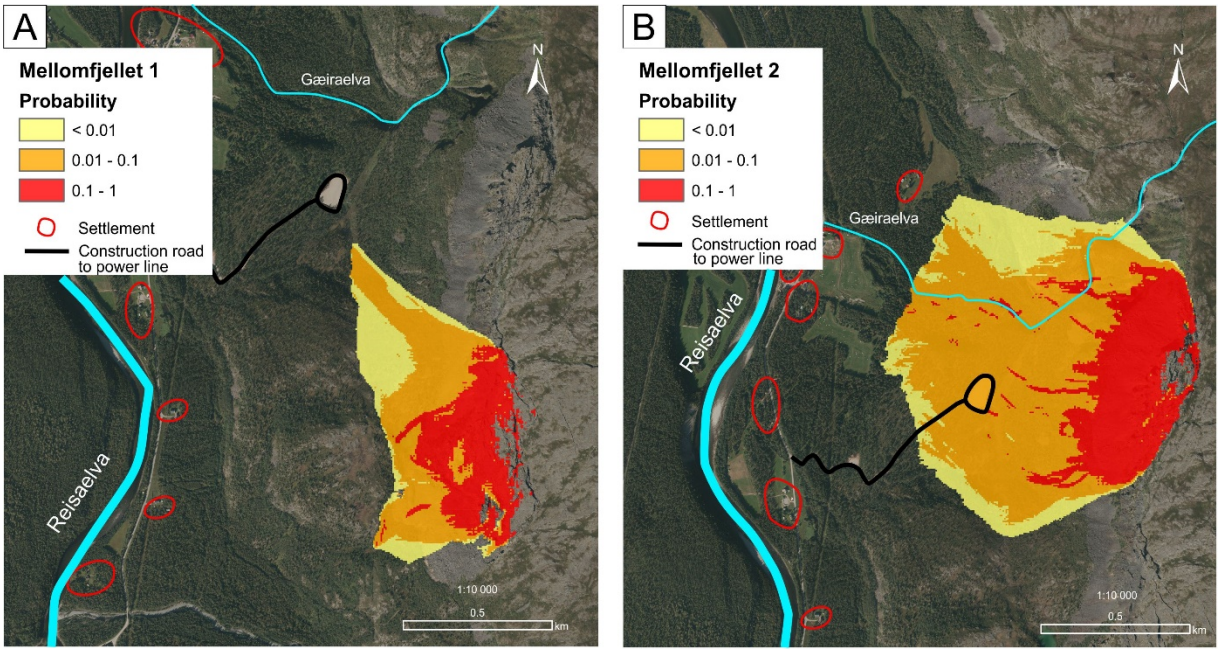

Figure 41 Flow-R modelling of the run-out at MF1 and MF2. Gentle slope dip and elevation in the terrain below MF1 constrains the run-out considerably.

4.7 Hazard assessment

The hazard is estimated using nine criteria following the NGU classification system and presented in section 3.5. The average score for MF1 is 5.3 and for MF2 it is 5.6, which place them both in the medium hazard class (Table 6). The risk matrices and the classification sheets with its justifications are presented in appendix F and Figure 55.

Table 6 Hazard scores from the hazard assessment.

Hazard Score	MF1	MF2
Minimum	5	5.5
Maximum	6	6
Average	5.3	5.6
Hazard Class	Medium	Medium

5 Discussion

This discussion chapter brings together key results from this study to present a conceptual overview model of the Mellomfjellet URS. The location of the geological profiles and main morphological features are presented in Figure 42.

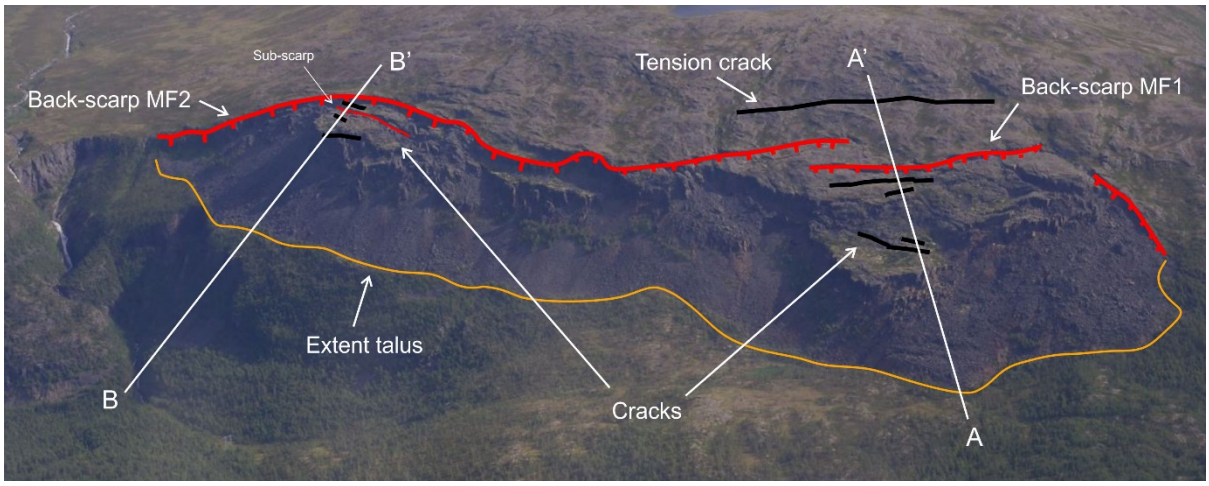

Figure 42 Aerial photo showing profiles A-A' and B-B' used for the geological profiles in Figure 44 and Figure 45 along with main morphological features.

5.1 Inherited bedrock structures

The regional geological history of the area, orogenesis and thrusting, followed by rifting extension of the passive margin (Andresen, 1988, Bergh et al., 2007, Faber and Stünitz, 2018, Indrevær et al., 2013, Zwaan, 1988), has led to the formation of many sets of structures that can be mapped on onshore northern Norway. The local structures at Mellomfjellet will be compared with the regional trends.

The bedrock hosts a westerly dipping and folded foliation and is similar to the large scale trends of the west-dipping nappe sequences formed in the Caledonian orogenesis (Figure 2). The folding of the foliation originates from ductile deformation during the orogeny. The foliation at Mellomfjellet is crosscut by a wide range of structures that indicate a post- Caledonian brittle deformation phase. The mapped joints that cross-cut the foliation are divided into three steeply dipping NNE – SSW (J1)-, WNW – ESE (J2) - and WSW – ENE (J3)-trending sets that align well with the mapped lineaments trending NNE – SSW, E – W and NW – SE (Figure 43). These mapped structures align with the post-Caledonian brittle structures described by

Indrevær et al. (2013) that formed due to multiple rifting events in the Late Paleozoic-Mesozoic. This tells us that the joints most likely formed during this post-Caledonian rifting event and the deformation at Mellomfjellet is controlled by pre-existing fractures.

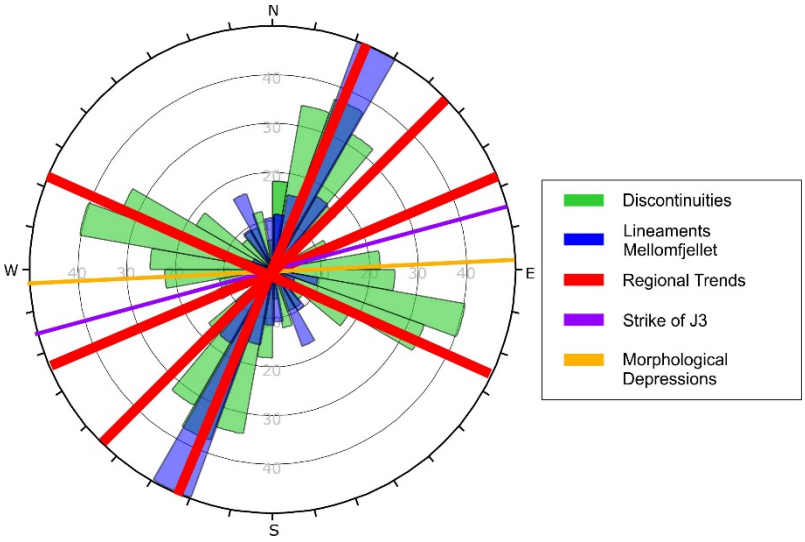

Figure 43 Rosette plot of mapped structures at Mellomfjellet along with the regional trends of the post-Caledonian brittle structures described by Indrevær et al. (2013). The figure highlights the alignment of mapped structures with the regional trends. The relationship between J3 and the morphological depressions will be discussed in section 5.2.3.

5.2 Structural analysis

5.2.1 Uncertainties in the structural data

When discussing structural data it is important to acknowledge that there may be errors in the analysis introduced by data uncertainty. Due to both the methodology of data acquisition and the natural variability of structures over a large site, the following needs to be considered:

- Data bias introduced by outcrop mapping on similar slope aspects;
- Difficulty in comparing domains due to different sample numbers;
- Data from the two domains varies slightly as a result of slightly different outcrop aspects between the two domains;
- Assigning sets;
- Fold axes measurement;
- Lack of information at depth.

The structural data was obtained predominantly from west-facing outcrops at Mellomfjellet. Sampling from mostly one slope aspect means that structures oriented parallel or subparallel to the outcrop may be overlooked. This may introduce a bias in the mapped structural data whereby those structures are underrepresented.

The number of measurements recorded at MF1 is higher (n = 310) than at MF2 (n = 263). The difference in sample numbers for each domain introduces uncertainties in the selection of statistical significant structures, especially when comparing cluster densities between the two domains. The higher number of measurements at MF1 may also be a reason for the increased variability in the discontinuity sets.

The predominant outcrop aspect at MF1 is different to that at MF2. This may have led to a slightly different sample between the two domains. For example, one limb of the foliation folding is overrepresented at MF2, because the slope orientation is not perpendicular to the fold axis, as it is for MF1 (Figure 16 and Figure 17).

The structural analysis groups the individual structural measurements into discontinuity sets and assigns each set an average value. This is generalizing the data and should be noted when discussing the results, as stability may be affected by structures striking or dipping within the variability bracket. For example, the foliation dip is close to the frictional value, which governs the feasibility for failure (Figure 26).

It is difficult to accurately measure fold axes in the field, and therefore the accuracy of the fold axes measurements in the data may be reduced. The fold axes can also be determined from statistical methods in Dips. This tool should be used alongside traditional measurements, to ensure the uncertainties from both methods are accounted for.

The main uncertainty connected to the geological models that will be presented is the lack of information about what is happening at depth. The geological models with the interpreted failure surfaces will be based on the structural data obtained at the surface.

5.2.2 Validation of photogrammetry data

Structural data acquired from Coltop3D analysis was included within the structural data set, in order to increase the number of structural measurements, and to sample the less reachable parts of the back-scarp. The joint sets determined from Coltop3D correlate well with the joint sets

from mapped discontinuity data. At MF2, the mapped J1 is oriented 022°/82°±14.7° and the Coltop3D derived J1 is 002°/72°±11.1°. J2 show a better correlation where the mapped data is oriented 108°/88°±15.3° and the Coltop3D data is 291°/88°±10.8°. However, there were some differences in the foliation orientation between the two methods. The difference in average foliation measured from Coltop (155°/22°±12.7°) and from the field (183°/11°±14.3°) was 28° in strike, and 11° in dip. There are some overlapping between the variability cones from the different foliation sets. The difference may be explained by user errors. Surfaces highlighted by the user as foliation in Coltop3D may in fact be a series of small foliation steps intersected by a steep joint set. The resultant structural measurement is taken as an average from a surface that interpolated between the steps and is therefore different from the actual foliation. Additionally, the foliation surface highlighted by the user may be folded, or the true orientation may be obscured by vegetation and therefore misread. However, the greatest uncertainty in the method was the use of a handheld GPS with a 2 m accuracy to mark the GCP's, and not the recommended high-accuracy GPS. Despite the uncertainties in the structural data, J1 and J2 display considerable similarities with the field data.

5.2.3 Structural control on mapped deformation features

Bedrock structure plays and important role in the deformation of URS (Wyllie and Mah, 2014). Failure surface development generally follows the path of least resistance and usually follows the anisotropic fabric of the bedrock (Wyllie and Mah, 2014). The assigned GSI value was 60 – 80, which is a strong to very strong rock, which states that the instability is likely due to tensile opening along joint sets. Mapped structures that have been placed in the regional geological context (Section 5.1) can be related to the mapped deformation features to draw conclusions about the control pre-existing discontinuities play on the development of failure surfaces.

This idea is well presented by the alignment of the back-scarps with the local joint sets/regional trends. The back-scarps at MF1 and MF2 are zigzag between NNE– and NNW– trending structures (Figure 32). At a local scale, the outcrops of the back-scarps are comprised of J1 and J2 surfaces. This tells us that the unstable area is controlled by pre-existing fractures and that the tensile component of the movement occurs along the mapped discontinuities (Figure 44).

The near-vertical sub-scarps at MF1 and MF2 are defined by J1 and J2 and comprise of the same structures as for the back-scarp (J1 and J2). At MF1 the sub-scarps strike NNW parallel

to the back-scarp and at MF2 the sub-scarp strike NNE parallel to the back-scarp and the strike of J1 (Figure 44). The sub-scarp at MF2 marks an increase in vertical displacement in the InSAR data (discussed in section 5.3) that shows different displacement rates for blocks within the URS.

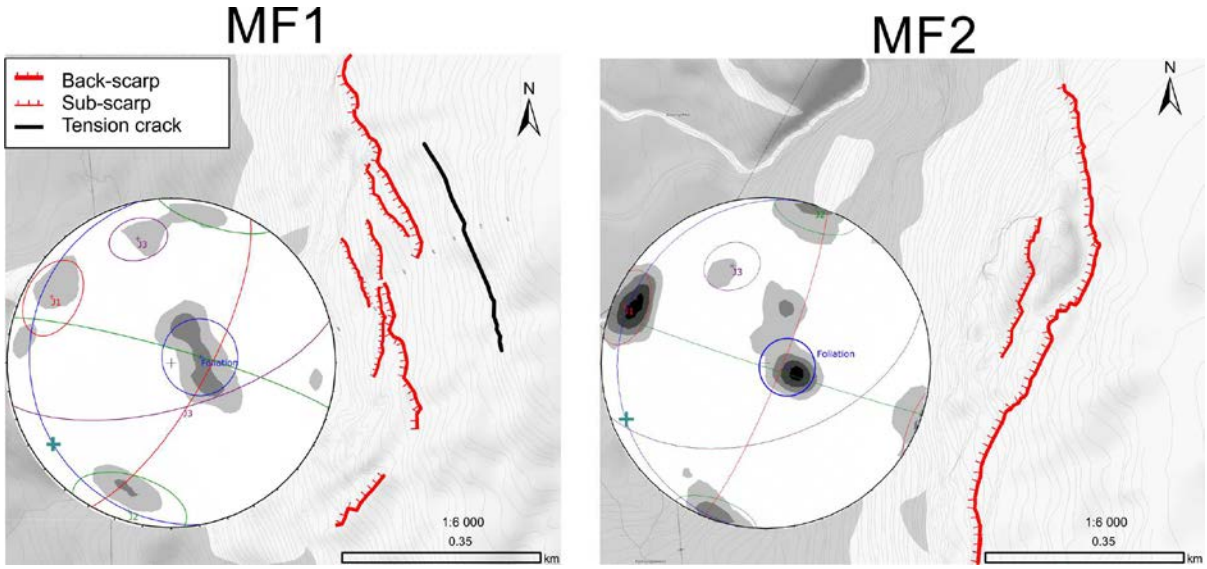

Figure 44 Map showing back-scarps, sub-scarps and tension crack along with Stereoplots of discontinuities.

The dip of the back-scarp appears overall vertical to steeply dipping westwards. However, in actuality the J1 component of the back-scarp dips eastward, into the slope. The sliding component of the movement is likely controlled by the foliation, and therefore the back-scarp is made up of a combination of J1, J2 and foliation surfaces and on average appears to be dipping to the west.

The tension crack observed above the back-scarp at MF1 aligns most closely with the trend of J1 (it is trending to the NNW), similarly to near-by sections of the back-scarp, and on a local scale the crack is comprised of J1, 2 and foliation surfaces (Figure 44). There is no observed vertical displacement across the tension crack, except for some localized sliding on foliation surfaces during opening. This observation may indicate several different development mechanisms at play at the site. One idea is that the tension crack indicates a retrogressive lengthening of the unstable area. Another explanation may be that the tension crack is not

connected to a failure surface at depth, but a relict tension crack from a previous event. These theories will be presented in detail in section 5.4.

The two east-west trending morphological depressions (presented in Figure 32) align well with regional fault trends (Figure 43). The presence of boggy ground within the depressions indicates that they have a component of fluid flow and may be inherited faults.

J3 is only mapped within the proximity (80 m) of these depressions, and generally aligns with the trend of the depression axes (ENE – WSW). It is possible that, if the depression represent fault surface traces, that J3 is linked to the faulting (Figure 32). The effects of J3 concerning stability should therefore be considered localized to those areas.

5.2.4 Kinematic analysis

The kinematic analysis provides insights as to which structures are problematic for failure, however it is important to validate the results rather than to simply accept and present what the Dips model shows. The results of the kinematic analysis should be considered carefully, as generalizations are made. The strike and dip of the slope are averages, there is variability in the structural data and the lateral limits as well as the friction value are estimates. The method only considers the geometrical conditions along each fracture set. It does not consider shear strength of rocks determined by e.g. lithology, fracture persistence and fracture density.

5.2.4.1 MF1

Kinematic analysis from domain MF1 shows that no structure set averages are in the critical zone for failure. However, visible displacement is mapped in the field and observed on InSAR, and therefore a more complex consideration of analysis results is required. Flexural toppling is considered a partly possible failure mechanism, along J1 (Figure 27), which is feasible as J1 is mapped as dipping in to the slope at MF1.

Planar sliding is not considered possible based on the average foliation measurement given a friction angle of 20°. However, 44% of the foliation measurements are steeper than the friction angle, and therefore the variability cone is partly located within the critical area for planar sliding.

Wedge sliding is not considered feasible based on set averages, but the variation within the foliation measurement puts 19% of intersections between foliation and J2 or foliation and J3 within the critical area for wedge failure.

5.2.4.2 MF2

Kinematic analysis for MF2 display that J1 is in the critical zone for flexural toppling with over 75% of the set located in the critical zone. J3 is located in the partly possible zone for flexural toppling.

Planar sliding is not considered possible, as the average foliation is gentler dipping than the friction angle. The variability cone is located within the critical area for planar sliding as 30% of the foliation measurements are steep enough to allow for failure.

Wedge sliding is not feasible as the intersection between J2 and the foliation and J3 and the foliation do not intersect in the critical area for wedge sliding. However, 12% of the mentioned intersection is located in the possible failure mechanism for wedge sliding.

The measured fold axes for MF1 plunge 15° to 21° and may be a main structure that allow for failure at MF1. However, the estimated fold axis based on the foliation data plunges 14°, which is not steep enough to allow for failure.

5.3 Relationship between displacement data, bedrock structures and morphological elements

The InSAR data show that the unstable rock slope at Mellomfjellet is active. Displacement show variable subsidence in the slope and that the mapped morphostructural elements delineate the unstable rock slope.

The InSAR data display changes in displacements that coincide with mapped morphostructural elements. The Sentinel-1 data and the RSAT-2 both display subsidence in the unstable area delineated by the back-scarp and the tension crack (Figure 38, Figure 39 and Figure 40). The back-scarp marks a distinct increase in displacement for both domains. Both datasets also indicate small amounts of displacement above the back-scarp, and below the tension crack, an area previously considered stable. At MF1 the tension crack marks a boundary for displacement as the area in between the back-scarp and the tension crack along C – C’ displays an increase

from - 0.5 mm/year to - 2.7 mm/year (Figure 45). The Sentinel-1 displays a small increase (0.7 mm/year) in displacement for the same area. This indicates instability above the back-scarp at MF1 and may lead to an interpretation of retrogressive failure (further described in 5.4).

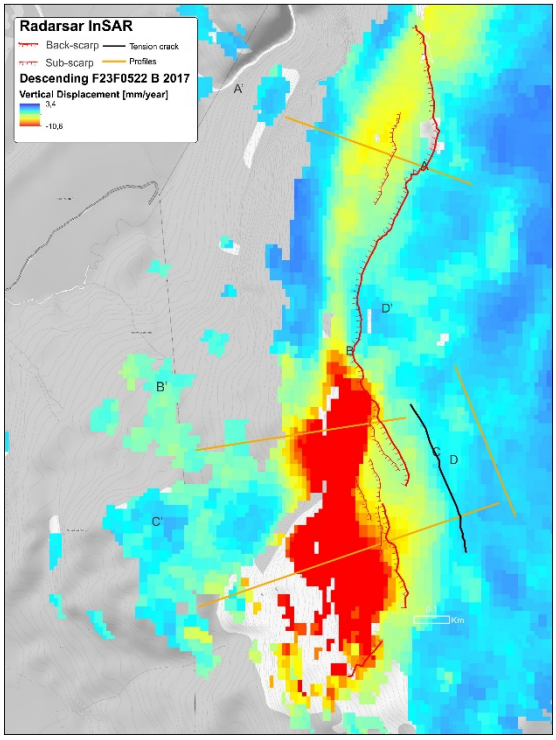

Figure 45 RSAT-2 InSAR data with back-scarp, sub-scarp and tension crack marked. Repeating of Figure 40 for easy reading.

By using a polygon analysis to interpret the Sentinel-1 data at MF2, it is possible to see that the outermost (downslope) block is displacing faster than the inner block (block located between the back-scarp and the outermost block) (Figure 39). The blocks at MF2 are moving with different rates, and this indicates a piece-by-piece failure, rather than a catastrophic large-scale failure. The confinement of the inner block restricts the displacement towards the free surface.

The different displacement rates for the Sentinel-1- and the RSAT-2 datasets may originate from the different processing methods, as well as the polygon vs profile analysis interpretive methods. The latter may have also included displacement data from talus deposits resulting in an artificially increased displacement rate. The ~10° difference in line of sight angle may also contribute to the differences in displacement rates. Displacement rates from both datasets are in millimeter scale, which is also within the potential range for error introduced by the method.

However, the two datasets are consistent with each other in that they both show displacements in the same areas, and therefore the displacement is interpreted to reflect actual displacement.

5.4 Geological model for MF1

In order to get a sense of how MF1 is failing, and what is happening at depth, all data interpretations have been implemented into a conceptual model and presented on a simplified cross section and cartoon illustration (Figure 46 and Figure 47).

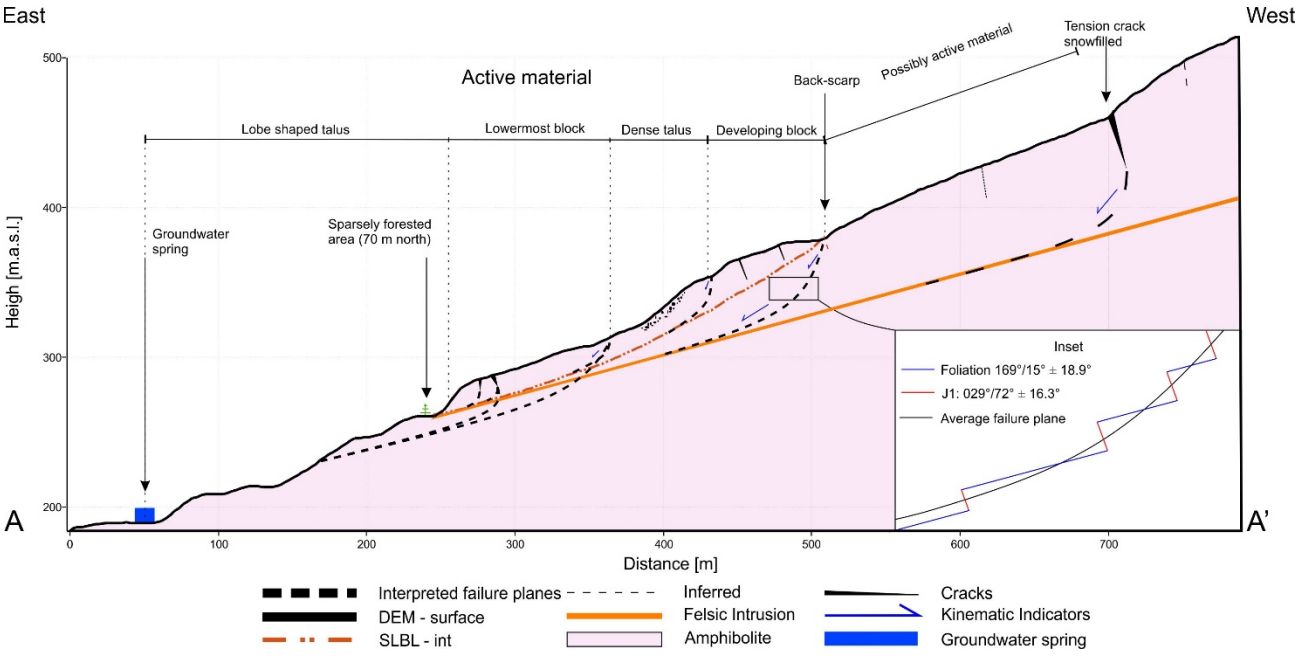

Figure 46 Geological profile over MF1. The intermediate SLBL from the analysis is included to represent a possible failure surface. Inset displaying a feasible mechanism of failure. J2 and J3 are omitted as J2 is parallel to the profile and J3 only is found in relation to the morphological depressions located away from A – A'.

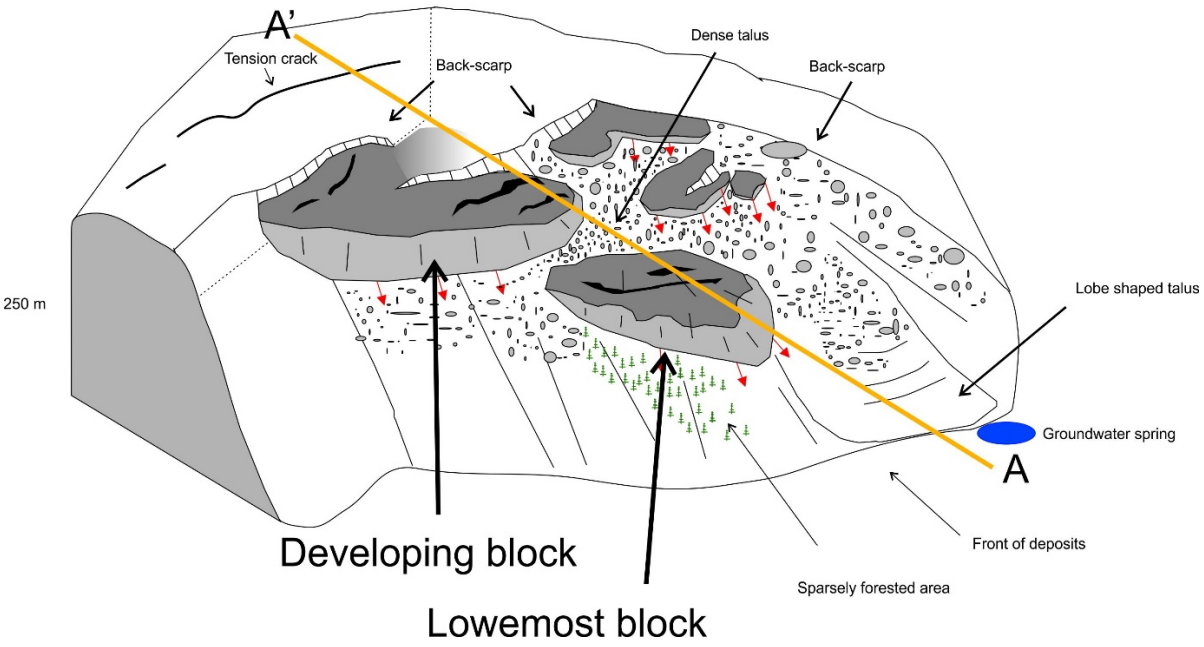

Figure 47 3D sketch of failure mechanism at MF1. Red arrows suggesting movement vectors. A – A' is the base for the profile in Figure 46. The blocks in the sketch is marked in the profile.

The unstable rock slope at MF1 is displacing as individual blocks. The instability is interpreted from the profile to be in the top 30 – 60 meters. The different blocks are separated by dense talus and disintegrated material (Figure 32, Figure 46 and Figure 47). The horizontal displacement between the different blocks and between the blocks and back-scarp indicate displacement along a basal failure surface. The profile highlights interpreted failure surfaces, the SLBL analysis and the felsic intrusion (Figure 46). The inset displays an interpreted bi-planar compound failure mechanism (Glastonbury and Fell, 2008) following the foliation and J1 as seen in Figure 48. The failure surface is interpreted to host a listric behavior at depth in order to daylight near the toe of the slope. The kinematic analysis showed that the average foliation is too gentle dipping to be kinematically feasible for sliding, therefore a bi-planar compound slide comprised of J1 and the foliation could provide a kinematically feasible failure surface that would allow for the observed displacements (Figure 48 and Figure 53). This requires a complex system of interconnected discontinuities and extensive damage throughout the rock mass. Although the roughness of the foliation surfaces is the lowest of all the discontinuity sets, which would lower the shear strength of the foliation surface and potentially allow for sliding, the folding of the foliation adds to the complexity of the failure surface.

The spatial distribution of the displacement (section 4.3) may origin from the difference in constraining throughout the URS. The lack of lateral limit/free surface to the left in Figure 47 allows for different displacement rates and difference development of the scarps and cracks.

Figure 48 Back-scarp at MF1 display a bi-planar compound failure in the stepwise failure along J1 and the foliation (Glastonbury and Fell, 2008).

There are two leading interpretations on the failure mechanisms at MF1. The first interpretation is simply that the listric failure surface is made up of J1 and the foliation, and foliation accommodates sliding. The second interpretation is that the basal failure surface follows the foliation-parallel felsic intrusion. Observations concerning the felsic intrusion indicate factors

that may influence the unstable rock slope. The intrusion marks a change in lithology and may create a boundary for groundwater flow and the observed seepage at the (assumed) toe of the rockslide may come from this horizon. The presence of clay and fine-grained soils within the intrusion may create higher water pressures at the boundary on top of the felsic intrusion, leading to a lower effective shear strength at the boundary of the felsic intrusion zone (Wyllie and Mah, 2014). However, there are some large assumptions made for this theory to be correct, including the nature of the layer at depth and the persistence of the layer throughout the URS (as it was only mapped at the toe). The fact that it outcrops above the base of the lowermost block in the toe area questions the role of the layer to be the main failure surface.

The main conceptual model at MF1 uses retrogressing failure as the main explanation for the failure observed at MF1 (Figure 49). The slope-parallel displacement of the lowermost block allows for further displacement upslope. The uppermost blocks have yet to develop a continuous back-scarp and the tension crack might indicate the next back-scarp.

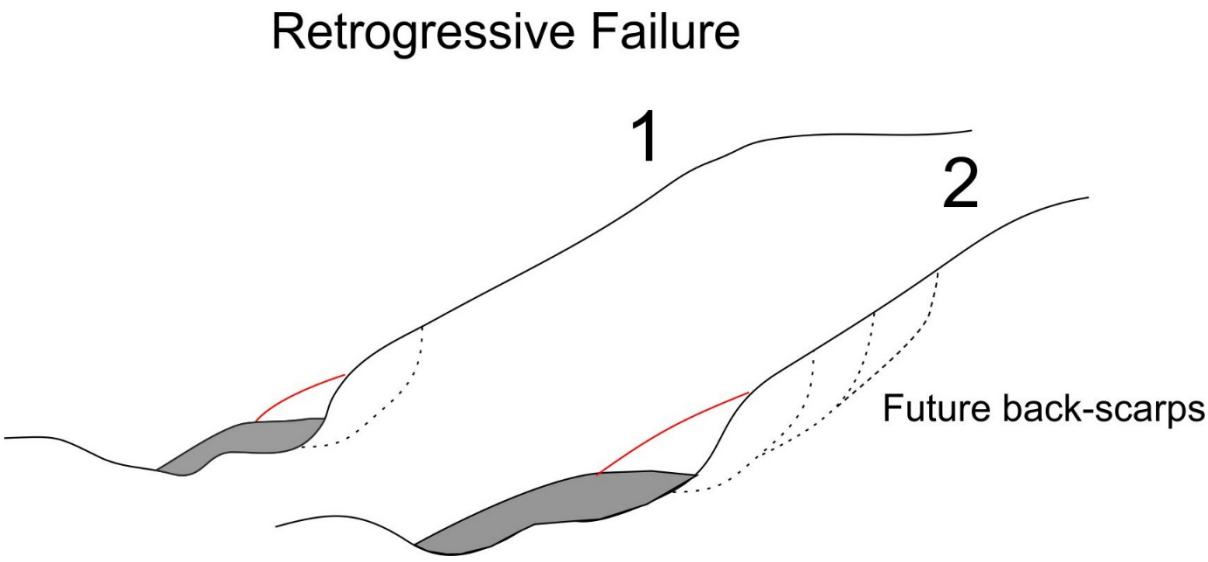

Figure 49 Sketch of a retrogressive failure. Based on Cruden and Varnes (1996) where displaced material are grey, previous slopes in red and failure planes are stippled.

The low displacement rates in between the back-scarp and tension crack may be interpreted to indicate that this area is stable. If so, the development of the main tension crack could be explained differently. A study by Böhme et al. (2013) at the unstable rock slope Stampa presents

interesting results that could be applied to MF1. The stress distribution at the slope was investigated to see how it would change after a rockslide. They conclude that weakness zones have already developed prior to the slope failure, and thus are present now only as remnants of the former instability. If this theory is applied to MF1, the tension crack could be interpreted as originating during a different stress regime prior to a rock slope failure.

Below the active area a talus lobe is mapped. This talus lobe has a different morphology than talus elsewhere at the URS (Figure 47). The lobe-shape with radial ridges and over-steepened front may originate from creeping of the talus (Figure 33). The lobe could be a rock glacier, but it is located at 200 m asl, which is significantly below the present permafrost limit for the area and thus it may be an old/extinct rock glacier.

The areas of disintegrating blocks in the slope show highly fractured blocks that disintegrates and display that deformation takes place. The steep front of the blocks and the near-vertical back-scarp provides feasibility for rock-falls that may describe the extent of the talus. Rock-falls from the blocks and from the disintegrating blocks area may be interpreted to be the source of the thick talus at MF1. The disintegrating blocks may also indicate that blocks do not fail catastrophically, but disintegrate in the slope.

5.5 Geological model for MF2

The conceptual model of MF2 is presented on a cross-section and a cartoon illustration (Figure 50 and Figure 51).

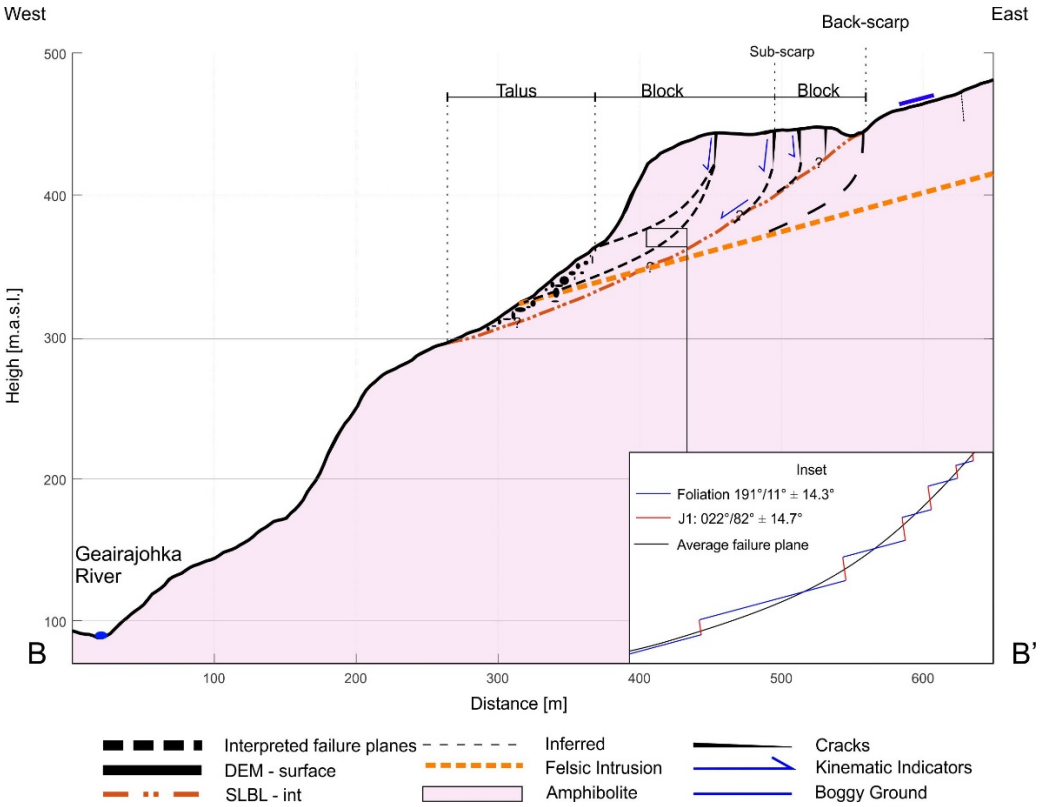

Figure 50 Profile perpendicular to the back-scarp at MF2. The intermediate SLBL-surface and interpreted failure surfaces are included. Inset displaying a feasible failure mechanism. J2 and J3 are omitted as J2 is parallel to the profile and J3 only is found in relation to the morphological depressions located away from B – B'.

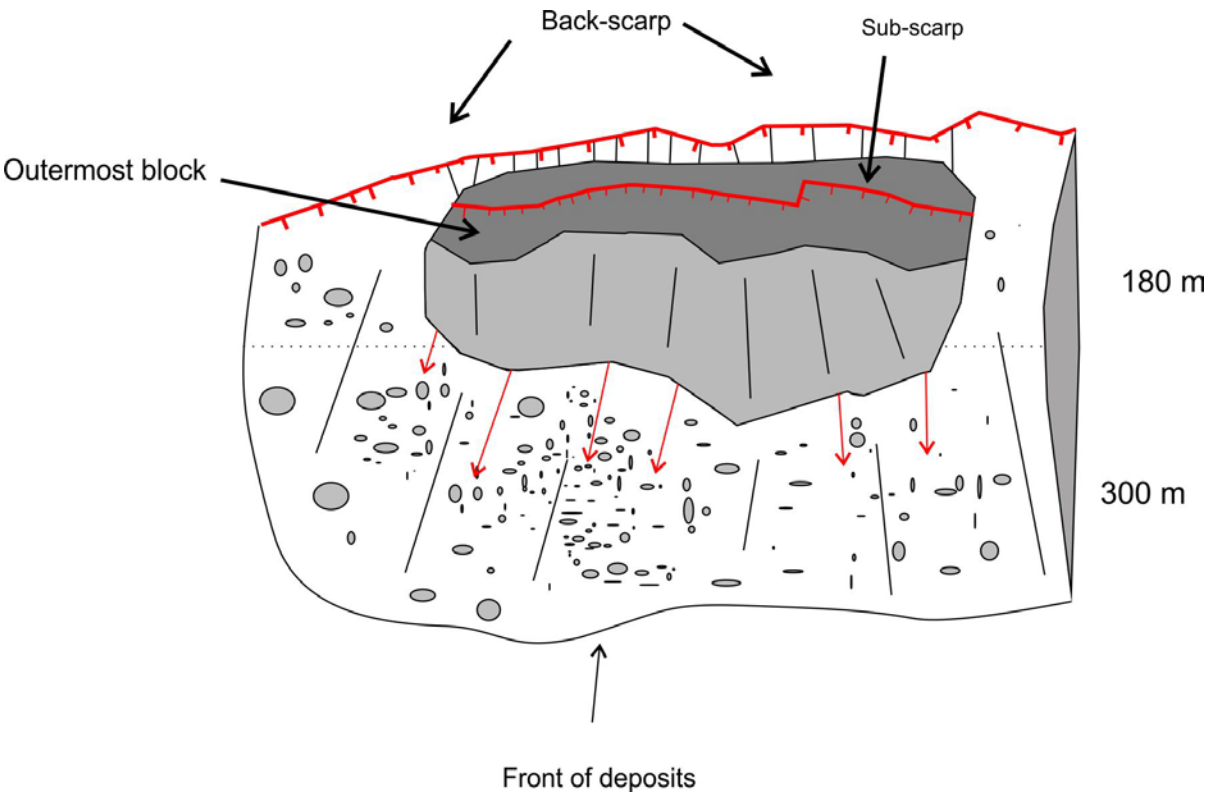

Figure 51 A 3D schematic sketch focusing on the unstable blocks at the URS at MF2 (block seen in morphological map; Figure 32). Red arrows are indicating displacement directions.

The unstable rock slope at MF2 is characterized by two large blocks separated by a sub-scarp (Figure 51). The failure surface is interpreted to be listric and daylight in the talus. This leads to an interpreted depth of 80 m of the instability.

The two leading interpretations on failure mechanisms at MF1 apply to MF2. The gentle foliation does not allow for planar failure and therefore a bi-planar compound slide mechanism is proposed where the foliation accommodates the sliding. The second interpretation where the basal failure surface follows the foliation-parallel felsic intrusion may also apply. The felsic intrusion is not observed in the unstable slope of MF2 as talus deposits cover the bedrock. Therefore, the felsic intrusion is interpolated to outcrop below the blocks of MF2 which leads to a degree of uncertainty for the failure mechanism.

A third interpretation is proposed, as the kinematic analysis displays feasibility for flexural toppling. Joint set 1 allows a toppling mechanism to develop and may control the deformation (Figure 52). The feasibility for flexural toppling questions the role of a basal failure surface as

the observed displacement may come from rotation of individual blocks. However, flexural toppling may occur on top of a basal failure surface as shown by the slide topple by Hermanns and Longva (2012) in Figure 53C.

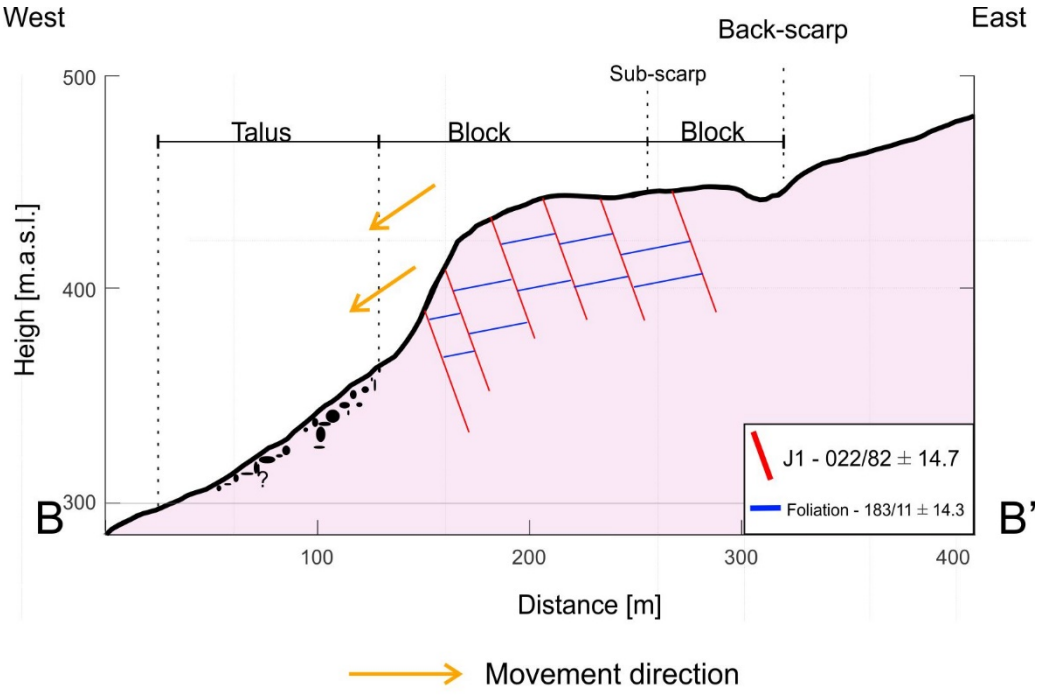

Figure 52 Sketch of a flexural toppling mechanism at MF2. The exaggerated discontinuities show the feasibility for J1 to allow for flexural toppling. The foliation allows for block flexural toppling as well.

The InSAR data shows a higher displacement for the outermost blocks for both domains and indicates a block-by-block failure rather than a large-scale catastrophic failure. However, a collapse of smaller blocks will not rule out a large-scale failure, as it could destabilize the upper part of the instability, which could then collapse as a large-scale failure.

If the failure mechanism at MF2 is flexural toppling, the displacement vector for toppling blocks will have a horizontal component. The line of sight measurement in the InSAR data is therefore not optimal for capturing the displacement. The acquired displacement would only be a fraction of the actual displacement, which adds uncertainty to the displacement observed at MF2.

5.6 Classification

The URS at Mellomfjellet share a wide range of features that are used to describe deep-seated gravitational slope deformations (DSGSD), such as surface deformation features (e.g. scarps) that are of a gravitational origin which coincide with inherited tectonic fractures and the location in metamorphic foliated rock in a glaciated valley (Agliardi et al., 2012). However, the size of the unstable rock slope at MF1 (1.59 Mm^3) and MF2 (3.05 Mm^3) is a fraction of what is common for most DSGSD (commonly > 500 Mm^3). Poorly defined lateral boundaries and bulging at the toe are also common features for DSGD, but MF1 and MF2 display clearly defined boundaries and no bulging at the toe is evident. The interpreted shallow failures with a continuous and well-defined sliding surface do not characterize as DSGSD (Soldati, 2013).

Structural scenarios that can lead to catastrophic failure are presented in Figure 53 (Hermanns and Longva, 2012). The proposed conceptual geological model for MF1 shows similarities with the bi-planar compound slide (Glastonbury and Fell, 2008). At MF2 the flexural toppling mechanism and the interpretation of a basal failure surface shows striking similarities with the slide topple model in Figure 53B, which is the model proposed in Figure 54C in Braathen et al. (2004).

MF1 display similarities to ‘rockslide areas’ described in Braathen et al. (2004; Figure 54B). This is based on the volume, area, style of deformation, slope gradient, and structural geometry: the volumes do not exceed 10 Mm^3, the areas cover less than 1 km^2, the detachment is a surface parallel to foliation that is ‘oriented sub-parallel to the slope and blocks are bounded by steep to vertical extension fractures and joints and gentle slope dip’.

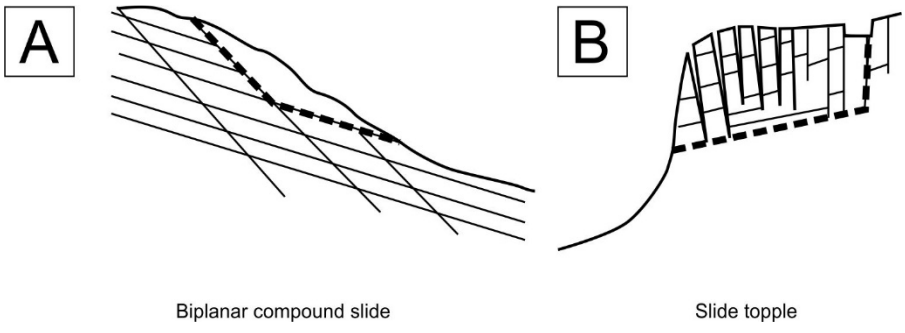

Figure 53 A selection of relevant structural environments where catastrophic slope failures have occurred in the past. Obtained from Hermanns and Longva (2012).

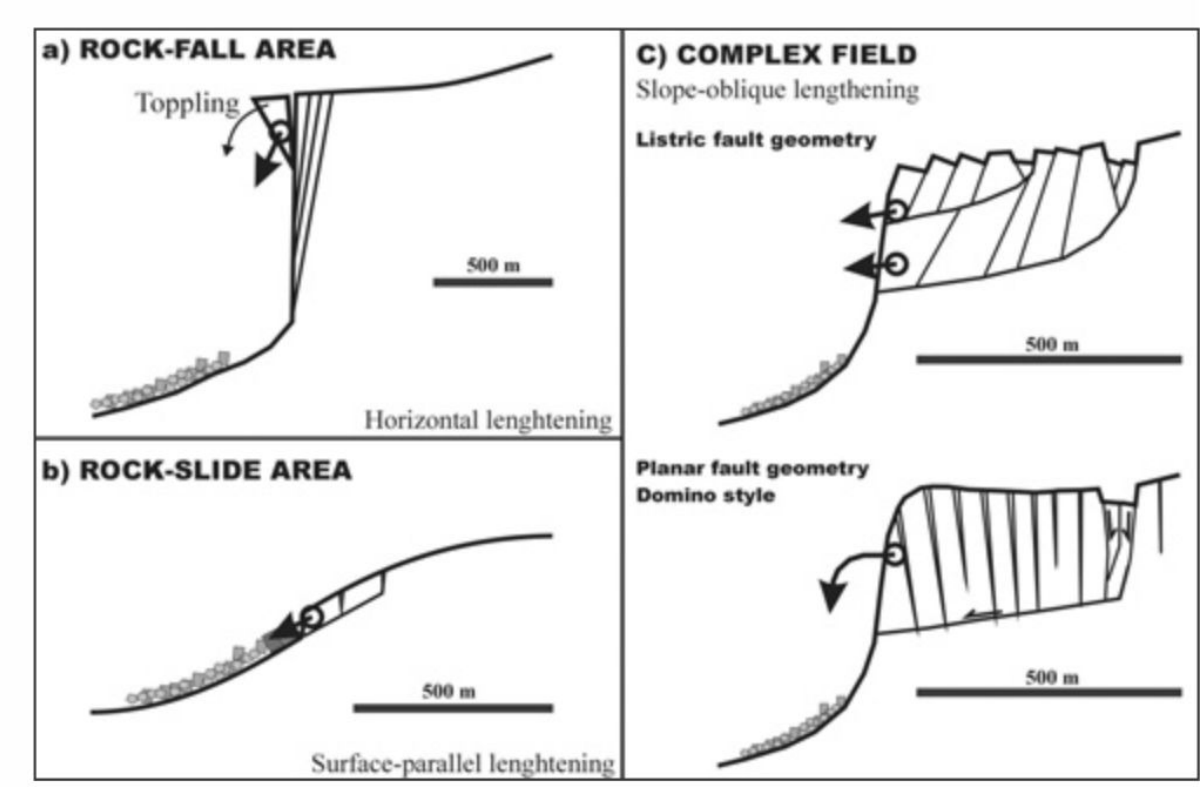

Figure 54 Geometric model for rock-slope failures. Obtained from Braathen et al. (2004).

5.7 Development of the URS

Factors that may have started the initial displacement at Mellomfjellet will be discussed in this section.

5.7.1 Glacial processes and rebound

Reisadalen is a glaciated valley and ice front delta deposits are found at the base of Mellomfjellet (NGU, 2019). The bedrock at Mellomfjellet may therefore be affected by periglacial mechanisms such as weakening of valley walls by stress release that results in the propagation of internal jointing following the debuttressing, as well as seismic activity due to differential glacio-isostatic rebound (Ballantyne, 2002). However, the amount of influence these processes have is controlled by lithology, structure and possibly seismicity (Bovis, 1982). These glacial related factors may have led to the original development of the URS and continue to influence the present day displacement due to the weakened bedrock.

5.7.2 Seismic activity

Seismic activity is a known trigger for rock avalanches and earthquakes and events of magnitude 6.0 are regarded as a minimum for triggering rock avalanches (Keefer, 1984). Dehls et al. (2000) propose that there seems to have been major earthquakes in the order of 6.0 after the last glaciation in the area. Evidence of major earthquakes ($M_w \geq 7.0$) and faulting has been reported at several spots in Fennoscandia during late- or post Weichselian recession (Lagerbäck and Sundh, 2008, Mörner, 2004). Large earthquakes directly after deglaciation may have triggered the initial development of the URS at Mellomfjellet.

Earthquakes larger than magnitude (M) 5.5 are rare in Norway and occur along certain major structures (Braathen et al., 2004). Therefore, the likelihood of a seismic triggered present day failure is low, but present.

5.8 Controlling factors

The processes for the present day displacement of the URS at Mellomfjellet will be discussed in this section.

5.8.1 Water and permafrost

Groundwater and drainage have a crucial effect on slope stability. Groundwater in the bedrock reduces the stability of discontinuities by reducing the effective shear strength of potential failure surfaces. Water pressure in tension cracks increase the forces that induce sliding. Boggy ground and small streams infiltrating the fracture system are the main observations of water above the back-scarp. Streams coming out of the talus indicate ground water present at the slope and that there is a system of cracks leading water through the unstable area. The loosely forested area in the talus may indicate seepage of the groundwater in the slope. However, the vegetated area may not come from seepage of the groundwater, but due to more suitable growth conditions at this particular location. No major river is flowing directly into the slope and indicates that the main water source is precipitation and meltwater from snow and ice during the spring and summer. This will probably lead to a seasonality of the displacement with an acceleration during the warmer months.

The deep open fractures at Mellomfjellet allow cold air accumulation to occur and enables ice rich permafrost to develop in the fractures and possibly along active sliding planes. The

permafrost controlled rockslide deformation model presented in Blikra and Christiansen (2014) proposes that the ice rich permafrost along with meltwater drainage in spring is the major rockslide-controlling factor. The same style of deformation may occur at Mellomfjellet, even though it is located well below the regional permafrost limit, sporadic permafrost may exist down to sea level in deep-seated rockslide terrain (Blikra and Christiansen, 2014).

The role of snow and ice may also be a requisite for the development of the unstable rock slope in order to reduce the shear strength sufficiently to drive the displacement (Blikra and Christiansen, 2014). Freezing may block drainage paths and build up the water pressure in the slope that could lead to a decrease in stability (Wyllie and Mah, 2014).

5.8.2 The felsic intrusion

As discussed in section 5.4 the felsic intrusion may be a failure surface for the URS at Mellomfjellet. The intrusion marks a change in lithology, and may create a boundary for groundwater flow, along with clay and fine-grained soils, which typically display very low hydraulic conductivities. This may create higher water pressures at the boundary on top of the felsic intrusion, leading to a lower effective shear strength at the boundary of the felsic intrusion zone (Wyllie and Mah, 2014). This could be a controlling factor for the displacement at Mellomfjellet.

5.9 Scenario analysis and hazard and risk assessment

NGUs workflow for risk assessment of URS in Norway has been applied. Failure scenarios are based on the structural site investigation and displacement rates and worst-case scenarios were delineated (see Appendix E). The volume estimation provided input to the estimation of runout, which showed that there are no expected consequences from damming of a river (Figure 41). The main river in Reisadalen, Reisaelva, is not reachable by the deposits of Mellomfjellet and the smaller Gæiraelva that is covered by deposits of MF2, will not form a dam, and probably divert the river based on the topography of the river canyon in relation to the form of the deposits. The run-out modelling shows that no settlement is reached by a catastrophic failure at either MF1 or 2. The consequence class (potential loss of human life) is therefore zero according to the NGU risk classification system. However, the newly built power line is located in the 1% – 10% probability zone that could be reached by a catastrophic failure of the MF2

scenario. This is important for the power-line company and the inhabitants of Alta, who rely on a stable power supply.

There is uncertainty connected to the volume estimation, especially in the extent of surface (area) and depth of the delineated scenarios. The felsic intrusion that may be the basal failure surface would change the scenario by increasing the volume estimated for MF1 and MF2. An increase in volume would increase run-out length, however the volume would have to be increased to c. 20 – 35 Mm^3 to have a run-out distance of 1300 m in order to reach the nearest farm, when estimating with the Scheidegger curve. That is at least 5 times as large as the maximum SLBL volume estimate and volume estimates using one of the other basal failure surfaces from the geological profile would not be that large (Figure 50). The volumes for both scenarios could also be overestimated due to a possible piece-by-piece failure. This could increase the angle of reach and maybe not even reach the power-line. However, the Scheidegger curve is, as mentioned, a conservative approach for maximum run-out length for landslides in Norway and therefore the run-out is interpreted to not reach settlement.

The volumes presented in this thesis are smaller than the estimations by Henderson et al. (2010). They estimated a volume of 8 Mm^3 at MF1 and 9 Mm^3 at MF2 which is twice as large as the intermediate SLBL estimations of 1.12Mm^3 at MF1 and 3.05 Mm^3 at MF2 (Table 5). The main reason for the differences in estimations is the depth of the failure surface as the SLBL was shallower than what was estimated by Henderson et al. (2010).

There are limitations to the hazard analysis as generalizations and assumptions are made for the input data. The morphological features indicating failure surface may be covered by talus-deposits and there may be a possible acceleration that is not observed in the current data set. This increases the range of possible hazard-scores and the total uncertainty connected to the method.

The hazard analysis puts both scenarios in the medium hazard class, and together with no consequences, the risk is plotted in the low risk area (blue area; Figure 55). Hermanns et al. (2012) recommends no follow up for low risk objects except a routine scanning in the field or based on remote sensing data (air photos, satellite data) every 10 – 20 years. The team from NGU decided that the site does not need to be followed up, because it has no consequences.

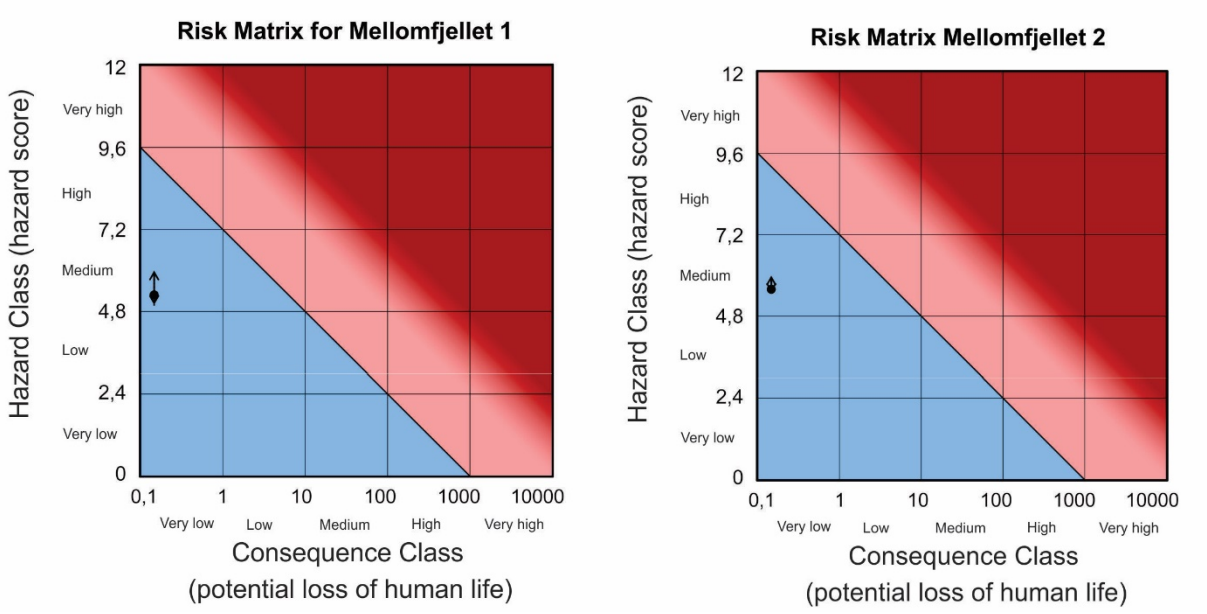

Figure 55 The risk matrices for MF1 and MF2. Note that both plot in the low risk class.

5.10 Further work

Based on the NGU risk classification system no further investigations are recommended, except for a routine scanning every 10 – 20 years, as there are no consequences related to a catastrophic failure of the URS.

However, further investigations are interesting from a scientific point of view. The uncertainties in the geological model could be reduced with the aid of borehole data and a proper monitoring program. The main uncertainties are connected to lack of data from depth and from the one directional displacement data. A borehole campaign could identify the role of the felsic intrusion in the unstable rock slope and piezometric data could reveal the hydrogeological conditions. Geophysics could improve the interpretation on what is happening at depth.

6 Conclusions

The structural assessment and characterization of the URS at Mellomfjellet may be summarized as follows:

- The Caledonian bedrock of Mellomfjellet is comprised of an amphibolite and a foliation parallel felsic intrusion that outcrops below the lowermost blocks.
- Based on the mapped structural data and the photogrammetry data the URS was divided into two domains. Joint set 3 was found in relation to morphological depressions, had a limited spatial distribution, and therefore only influences stability on a local scale.
    - MF1: Foliation (strike/dip; 169°/15°±18.9°), J1 (029°/72°±16. 3°) J2 (286°/83°±21.8°) and J3 (075°/67°±12.3°).
    - MF2: Foliation (183°/11°±14.3°), J1 (022°/82°±14.7°), J2 (108°/88°±15.3°) and J3 (071°/52°±12.7°).
- Kinematic analysis of the discontinuities showed that failure is kinematically possible.
    - MF1: Planar failure is possible for 40% of the foliation measurements and is therefore restricted by friction angle set to 20°. Flexural toppling is partly possible along J1.
    - MF2: Flexural toppling is possible along J1, and 30% of the foliation measurements allow for planar sliding.
- The detected InSAR displacement is localized to the unstable area delineated by the bedrock structures and morphological elements mapped at Mellomfjellet.
- The interpreted geological profiles for MF1 and MF2 proposes basal failure surfaces comprising of the foliation and J1 as a bi-planar compound slide and failure surface along the foliation parallel felsic intrusion. The feasibility for flexural toppling at MF2 with the foliation as basal surface show similarities with slide topple.
- The URS is controlled by pre-existing joints that coincides with regional lineaments trending NNE-SSW and ENE-WSW.
- The hazard classification puts the worst-case scenarios at Mellomfjellet in the medium hazard class and as no settlement is reached by the estimated run-out the risk is ranked as low. However, block-by-block displacement and active disintegration in the URS indicates that the estimated scenario will be smaller than the worst case since block-by-block failure is more likely.

- The instability at Mellomfjellet may originate from the over-steepening of the slope by glaciation. Driving mechanisms for the displacement may be water pressures and frost/permafrost related mechanisms.
- The URS shares common features that can be described to a deep-seated gravitational slope failure (DSGSD), however the volume and extent is smaller than what is common for DSGSD. The scenario at MF1 may be described as a bi-planar compound slide and the MF2 scenario display similarities with slide topple.
- No further investigations are recommended except for a routine scanning every 10 – 20 years, as there are no consequences related to a catastrophic failure (Hermanns et al., 2012). However, further investigations are interesting from a scientific point of view, e.g. find out what is happening at depth.

Works cited

AGLIARDI, F., CROSTA, G. B. & FRATTINI, P. 2012. Slow rock-slope deformation. *Landslides: Types, mechanisms and modeling***,** 207.

ANDRESEN, A. 1988. Caledonian terranes of northern Norway and their characteristics. *Trabajos de Geologia - Universidad de Oviedo,* 17**,** 103-117.

BAKKHAUG, I. 2015. *Undersøkelse av ustabilt fjellparti ved Adjet, Storfjord, Troms. Betydningen av ulike kategorier av glideplan i berggrunnen og mekanismer for utglidning.* University of Tromsø.

BALLANTYNE, C. 2002. Paraglacial geomorphology. 21**,** 1935-2017.

BAMLER, R. & HARTL, P. 1998. Synthetic aperture radar interferometry. *Inverse Problems,* 14**,** 1-54.

BEMIS, S. P., MICKLETHWAITE, S., TURNER, D., JAMES, M. R., AKCIZ, S., THIELE, S. T. & BANGASH, H. A. 2014. Ground-based and UAV-based photogrammetry: A multi-scale, high-resolution mapping tool for structural geology and paleoseismology. *Journal of Structural Geology,* 69**,** 163-178.

BERGH, S. G., EIG, K., KLØVJAN, O. S., HENNINGSEN, T., OLESEN, O. & HANSEN, J.-A. 2007. The Lofoten-Vesterålen continental margin: a multiphase Mesozoic-Palaeogene rifted shelf as shown by offshore-onshore brittle fault-fracture analysis. *Norwegian Journal of Geology/Norsk Geologisk Forening,* 87**,** 29-58.

BERGSTRØM, B. 1983. Deglaciation of the Reisa Valley, northern Norway, and studies of glacial deposits and dispersal processes. *Acta geológica hispánica,* 18**,** 161-167.

BJØRKLID, E. 2017. *Strukturgeologisk og geomorfologisk studium av fjellskred ved Skredan, Tromsø kommune.* University of Tromsø.

BLIKRA, L. H., BRAATHEN, A. & SKURTVEIT, E. 2001. Hazard evaluation of rock avalanches; the Baraldsnes–Oterøya area. *NGU Rapport 2001.108***,** 33.

BLIKRA, L. H. & CHRISTIANSEN, H. H. 2014. A field-based model of permafrost-controlled rockslide deformation in northern Norway. *Geomorphology,* 208**,** 34-49.

BOVIS, M. J. 1982. Uphill-facing (antislope) scarps in the Coast Mountains, southwest British Columbia. *Geological Society of America Bulletin,* 93**,** 804-812.

BRAATHEN, A., BLIKRA, L. H., BERG, S. S. & KARLSEN, F. 2004. Rock-slope failures in Norway; type, geometry, deformation mechanisms and stability. *Norwegian Journal of Geology/Norsk Geologisk Forening,* 84**,** 67-88.

BREDAL, M. 2016. *A structural, geomorphological and InSAR study of the unstable rock slope in Oksfjellet, Kåfjord, Troms.* University of Tromsø.

BUNKHOLT, H., REDFIELD, T., OSMUNDSEN, P., OPPIKOFER, T., HERMANNS, R. & DEHLS, J. 2012. Landslide processes in hard rock in Troms, Norway. *Conference: Landslides and Engineered Slopes: Protecting Society through Improved Understanding, At London***,** 855-861.

BÖHME, M., BUNKHOLT, H., OPPIKOFER, T., DEHLS, J., HERMANNS, R., ERIKSEN, H., LAUKNES, T. & EIKEN, T. Using 2D InSAR, dGNSS and structural field data to understand the deformation mechanism of the unstable rock slope Gamanjunni 3, northern Norway. Landslides and Engineered Slopes: Experience, Theory and Practice: Proceedings of the 12th International Symposium on Landslides (Napoli, Italy, 12–19 June 2016): Rome, Associazione Geotecnica Italiana, 2016. 443-449.

BÖHME, M., HERMANNS, R., OPPIKOFER, T., FISCHER, L., BUNKHOLT, H., EIKEN, T., PEDRAZZINI, A., DERRON, M., JABOYEDOFF, M. & BLIKRA, L. 2013. Analyzing complex rock slope deformation at Stampa, western Norway, by integrating geomorphology, kinematics and numerical modeling. *Engineering Geology,* 154**,** 116-130.

COLTOP3D. 2016. *The Alpine Railway: a step by step study, Coltop3D Beginner's Support Courses.* [Online]. Bussigny, Switzerland: Terranum: Rock- solid Geosciences and Software solution. . [Accessed 05.10.2018].

CRUDEN, D. M. & VARNES, D. J. 1996. Landslides: investigation and mitigation. Chapter 3-Landslide types and processes. *Transportation research board special report*.

DEHLS, J. F., OLESEN, O., OLSEN, L. & BLIKRA, L. H. 2000. Neotectonic faulting in northern Norway; the Stuoragurra and Nordmannvikdalen postglacial faults. *Quaternary Science Reviews,* 19**,** 1447-1460.

EKLIMA 2018. eKlima -Free access to weather- and climate data from Norwegian Meteorological Institute from historical data to real time observations. eklima.met.no/: Norwegian Meteorological Institute.

ERIKSEN, H. Ø. 2013. *Slope displacement patterns observed using satellite InSAR data in the Storfjord-Kåfjord-Lyngen region, Troms.* Universitetet i Tromsø.

ERIKSEN, H. Ø., BERGH, S. G., LARSEN, Y., SKREDE, I., KRISTENSEN, L., LAUKNES, T. R., BLIKRA, L. H. & KIERULF, H. P. 2017. Relating 3D surface displacement from satellite-and ground-based InSAR to structures and geomorphology of the Jettan rockslide, northern Norway. *Norsk Geologisk Tidsskrift,* 97**,** 283-303.

FABER, C. & STÜNITZ, H. 2018. Mountain building processes in the northern Norwegian Caledonides - Examining Caledonian continental collision using a combination of structural mapping, phase equilibrium modelling and geochronology. UiT Norges arktiske universitet.

FERRETTI, A., MONTI-GUARNIERI, A., PRATI, C., ROCCA, F. & MASSONNET, D. 2007. *InSAR Principles: Guidelines for SAR Interferometry Processing and Interpretation.* ESA publications.

FISCHER, L., RUBENSDOTTER, L. & STALSBERG, K. 2014. Aktsomhetskart jord-og flomskred: Metodeutvikling og landsdekkende modellering. *NGU rapport 2014.019***,** 72.

FURSETH, A. 2006. *Skredulykker i norge,* Tun.

GLASTONBURY, J. & FELL, R. 2008. A decision analysis framework for the assessment of likely post-failure velocity of translational and compound natural rock slope landslides. *Canadian Geotechnical Journal,* 45**,** 329-350.

GRUMSTAD, A. 2017. *Geomorfologisk og strukturgeologisk undersøkelse av ustabile skråninger og skredavsetninger i fjellområdet mellom Tromsøysundet og Ullsfjorden i Tromsf.* UiT Norges arktiske universitet.

HANNUS, M. 2012. *Structural geometry and controlling factors for a rock slope failure area at Hompen/Váráš, Signaldalen, Troms, North Norway.* Universitetet i Tromsø.

HENDERSON, I., OSMUNDSEN, P. T. & REDFIELD, T. 2010. ROS Fjellskred i Troms: Status og planer 2010. *NGU rapport 2010.021***,** 84.

HERMANNS, R. & LONGVA, O. 2012. Rapid rock-slope failures. *Landslides: types, mechanisms and modeling***,** 59-70.

HERMANNS, R., OPPIKOFER, T., ANDA, E., BLIKRA, L. H., BÖHME, M., BUNKHOLT, H., CROSTA, G. B., DAHLE, H., DEVOLI, G., FISCHER, L.,

JABOYEDOFF, M., LOEW, S., SÆTRE, S. & YUGSI MOLINA, F. 2012. Recommended hazard and risk classification system for large unstable rock slopes in Norway. *NGU-Report 2012.029.* Geological Survey of Norway.

HERNES, I. 2014. *Fjellskred ved Indre Nordnes, Nordnesfjellet, Lyngen, Troms-Berggrunnens indre struktur og bevegelsesmekanismer basert på strukturell analyse og overvakingsdata.* UiT Norges arktiske universitet.

HOEK, E. & BRAY, J. D. 2014. *Rock slope engineering,* CRC Press.

HOLMGREN, P. 1994. Multiple flow direction algorithms for runoff modelling in grid based elevation models: An empirical evaluation. *Hydrological Processes,* 8**,** 327-334.

HORTON, P. 2014. Implementation of rock avalanches assessment in Flow-R. *Report no.2014-PH01.* Terranum sàrl, Bussigny, Switzerland.

HORTON, P., JABOYEDOFF, M., RUDAZ, B. & ZIMMERMANN, M. 2013. Flow-R, a model for susceptibility mapping of debris flows and other gravitational hazards at a regional scale. *Nat. Hazards Earth Syst. Sci.,* 13**,** 869-885.

HUSBY, E. D. 2011. *Fjellskred i Nomedalstinden: en strukturstyrt masseutglidning på et underliggende storskala glideplan.* Universitetet i Tromsø.

INDREVÆR, K. & BERGH, S. 2014. Linking onshore-offshore basement rock architecture and brittle faults on the submerged strandflat along the SW Barents Sea margin, using high-resolution (5 x 5 m) bathymetry data. *Norsk Geologisk Tidsskrift- Norwegian Journal of Geology,* 94**,** 1-34.

INDREVÆR, K., BERGH, S. G., KOEHL, J.-B., HANSEN, J.-A., SCHERMER, E. R. & INGEBRIGTSEN, A. 2013. Post-Caledonian brittle fault zones on the hyperextended SW Barents Sea margin: New insights into onshore and offshore margin architecture. *Norwegian Journal of Geology,* 93.

JABOYEDOFF, M., BAILLIFARD, F., COUTURE, R., LOCAT, J. & LOCAT, P. 2004a. Toward preliminary hazard assessment using DEM topographic analysis and simple mechanical modeling by means of sloping local base level. *Landslides evaluation and stabilization. Balkema***,** 199-205.

JABOYEDOFF, M., BARDOU, E. & DERRON, M. Sloping local base level: a tool to estimate potential erodible volume and infilling alluvial sediment of glacial valleys. Swiss Geo-Scientists meeting, 2004b.

JABOYEDOFF, M., CROSTA, G. B. & STEAD, D. 2011. Slope tectonics: a short introduction. *Geological Society, London, Special Publications,* 351**,** 1-10.

JABOYEDOFF, M., DERRON, M., RUDAZ, B., OPPIKOFER, T., PENNA, I. & DAICZ, S. A review of geometrical methods for determination of landslide volume and failure surface geometry. Proceedings of the 68th Canadian Geotechnical Conference GEOQuébec 2015-Challenges from North to South, 2015.

JABOYEDOFF, M., METZGER, R., OPPIKOFER, T., COUTURE, R., DERRON, M. H., LOCAT, J. & TURMEL, D. 2007. New Insight Techniques to Analyze Rock-slope Relief Using DEM And 3Dimaging Cloud Points: COLTOP-3D Software. *1st Canada - U.S. Rock Mechanics Symposium.* Vancouver, Canada: American Rock Mechanics Association.

KEEFER, D. K. 1984. Landslides caused by earthquakes. *Geological Society of America Bulletin,* 95**,** 406-421.

KOEHL, J.-B., BERGH, S. G., HENNINGSEN, T. & FALEIDE, J.-I. 2017. Mid/Late Devonian-Carboniferous collapse basins on the Finnmark Platform and in the southwesternmost Nordkapp basin, SW Barents Sea. *Solid Earth Discussions***,** 1-68.

LAGERBÄCK, R. & SUNDH, M. 2008. Early Holocene faulting and paleoseismicity in northern Sweden: Research Paper C 836. *Geological Survey of Sweden: Uppsala,* 84.

LARSEN, O. P. E. 2014. *Geomorfologisk og strukturgeologisk studium av fjellskredet ved Falsnesfjellet, Storfjord, Troms.* UiT Norges arktiske universitet.

MARINOS, P. & HOEK, E. GSI: a geologically friendly tool for rock mass strength estimation. ISRM international symposium, 2000. International Society for Rock Mechanics and Rock Engineering.

MICHELETTI, N., CHANDLER, J. H. & LANE, S. N. 2015. Structure from motion (SFM) photogrammetry. *British Society for Geomorphology.*

MÖRNER, N.-A. 2004. Active faults and paleoseismicity in Fennoscandia, especially Sweden. Primary structures and secondary effects. *Tectonophysics,* 380**,** 139-157.

NGU. 2018. *Nasjonal database for ustabile fjellparti* [Online]. Available: http://geo.ngu.no/kart/ustabilefjellparti_mobil/ [Accessed 15.10. 2019].

NGU. 2019. *Løsmasser Nasjonal løsmassedatabase* [Online]. Available: http://geo.ngu.no/kart/losmasse/ [Accessed 14.05. 2019].

NOPPER, H. 2015. *Geomorphological study of the rock-slope failure at Adjet, Storfjord, Troms.* UiT Norges arktiske universitet.

NZGS. 2005. *Field description of soil and rock - field sheet* [Online]. New Zealand Geotechnical Society Guidelines. Available: http://www.nzgs.org/library/field-description-of-soil-and-rock-field-sheet/ [Accessed 06.06.2018].

OPPIKOFER, T., BÖHME, M., NICOLET, P., PENNA, I. & HERMANNS, R. L. 2016. Metodikk for konsekvensanalyse av fjellskred. *NGU rapport 2016.047.* Geological survey of Norway, Trondheim.

PEPE, A. & CALÒ, F. 2017. A Review of Interferometric Synthetic Aperture RADAR (InSAR) Multi-Track Approaches for the Retrieval of Earth's Surface Displacements. *Applied Sciences,* 7**,** 1264.

PORTER, C., MORIN, P., CLOUTIER, M., HOWAT, I., NOH, M.-J., WILLIS, M., BATES, B., WILLAMSON, C. & PETERMAN, K. ArcticDEM; a publically available, high resolution elevation model of the Arctic. EGU General Assembly Conference Abstracts, 2016. 8396.

RASMUSSEN, E. 2011. *Fjellskred i Laksvatnfjellet, Balsfjord, Troms: indre struktur, morfologi og skredmekanismer.* Universitetet i Tromsø.

ROCSCIENCE. 2018. *Tutorial 04 - Toppling, Planar and Wedge Sliding* [Online]. Available: https://www.rocscience.com/help/dips/pdf_files/tutorials/Tutorial_04_Toppling_Planar_and_Wedge_Sliding.pdf [Accessed 04.12 2018].

ROMANOVSKY, V. E., SMITH, S. L. & CHRISTIANSEN, H. H. 2010. Permafrost thermal state in the polar Northern Hemisphere during the international polar year 2007–2009: a synthesis. *Permafrost and Periglacial Processes,* 21**,** 106-116.

SANDNES, G. H. 2017. *Geomorfologisk og strukturgeologisk undersøking av ustabile skråningar og skredavsettingar. Regional analyse av fjellområdet mellom Tromsøysundet og Ullsfjorden-Troms, Norge.* UiT Norges arktiske universitet.

SCHEIDEGGER, A. E. 1973. On the prediction of the reach and velocity of catastrophic landslides. *Rock Mechanics,* 5**,** 231-236.

SKREDE, I. 2013. *Jettan, Nordnesfjellet, Kåfjord, Troms–indre geometri og struktur, kinematikk og styrande faktorar av eit ustabilt fjellparti, basert på strukturellanalyse, geomorfologi og overvakingsdata.* UiT Norges arktiske universitet.

SOLDATI, M. 2013. Deep-seated Gravitational Slope Deformation. *In:* BOBROWSKY, P. T. (ed.) *Encyclopedia of Natural Hazards.* Dordrecht: Springer Netherlands.

WESTOBY, M. J., BRASINGTON, J., GLASSER, N. F., HAMBREY, M. J. & REYNOLDS, J. 2012. 'Structure-from-Motion'photogrammetry: A low-cost, effective tool for geoscience applications. *Geomorphology,* 179**,** 300-314.

WYLLIE, D. C. & MAH, C. 2014. *Rock slope engineering,* CRC Press.

WYRWOLL, K. H. 1977. Causes of rock-slope failure in a cold area; Labrador-Ungava. *Reviews in Engineering Geology***,** 59-67.

ZWAAN, K. B. 1988. *Nordreisa. Berggrunnskart Nordreisa M 1:250 000; trykt i farger*. NGU-distribusjonen.

ZWAAN, K. B. & RYGHAUG, P. 1984. *Reisadalen. Berggrunnskart; Reisadalen; 17343; 1:50 000; sort/hvitt;*. NGU-distribusjonen.

Appendix

A. Bedrock map

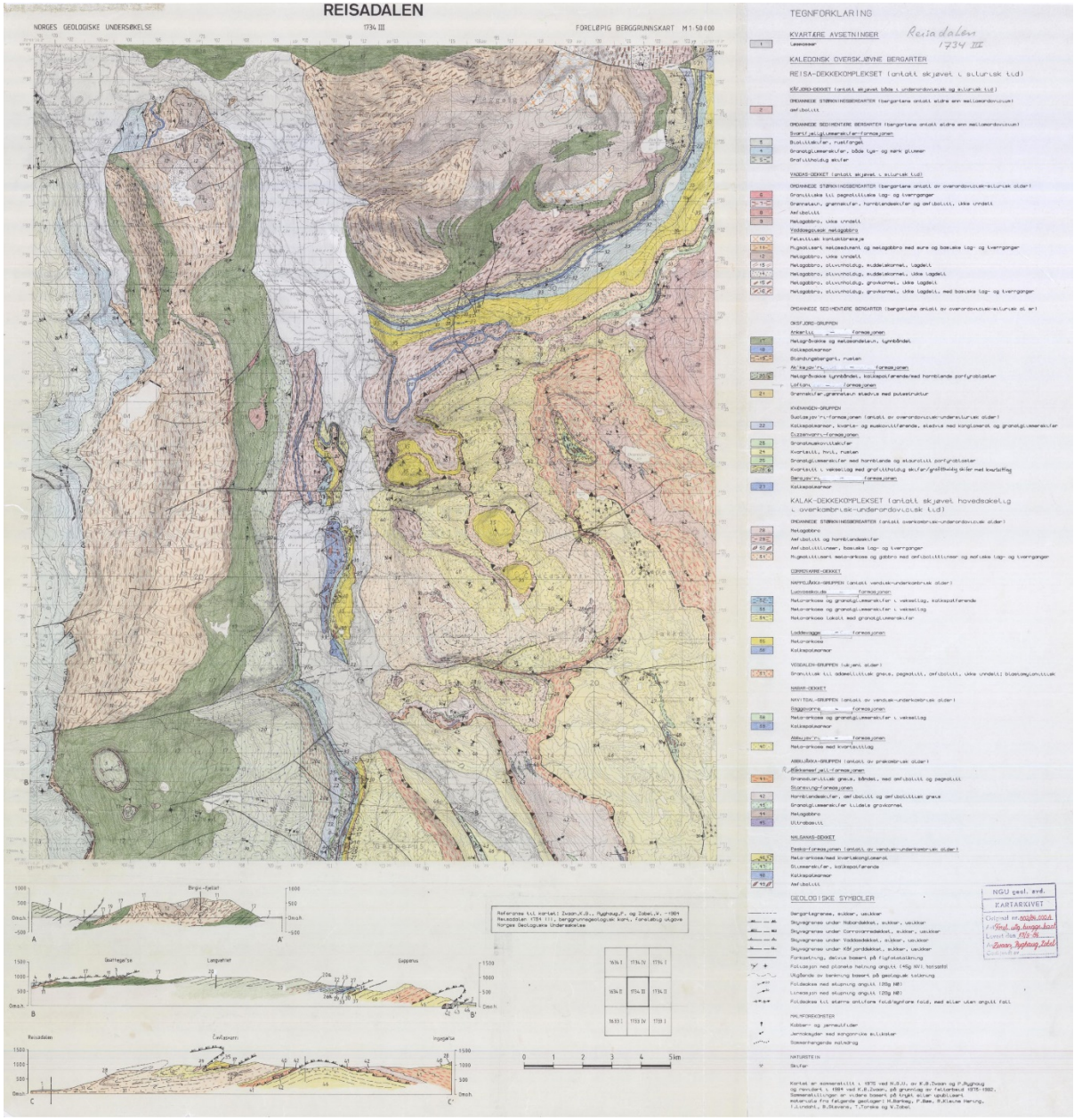

Bedrock map from NGU(Zwaan and Ryghaug, 1984).

B. Weather data

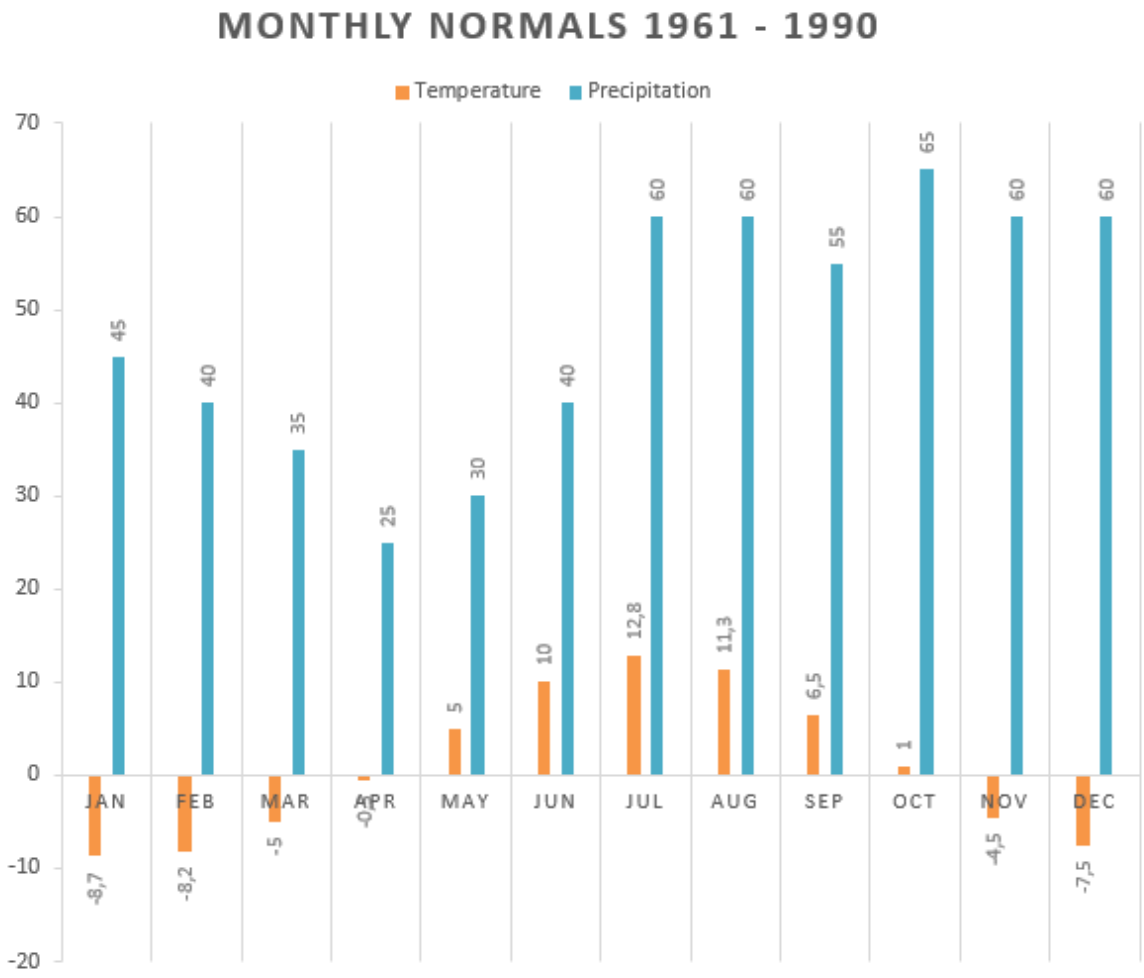

Temperature and precipitation at Øyeng in Reisadalen. Data obtained from (eKlima, 2018)

C. Agisoft photoscan

Image capture

Flight plan

Flights conducted at Mellomfjellet

Flight	Height above starting point [m]	Angles (Down is 0 degrees)
1	20	90 and 45
2	2	0, 45 and 70
3	30 to 40	70 and 90

Ground control points

GCP	WGS 84	WGS 84 [Decimal degrees]	Altitude [m]
1	N 69' 39.026' E 021, 20.318'	21,33863800 69,65043300	431,734192
2	N 69' 39.051' E 021, 20.329	21,33882300 69,65085000	432,277191
3	N 69, 39.071' E 021, 20.326'	21,33876900 69,65118300	435,571838
4	N 69, 39.030' E 021, 20.348'	21,33913600 69,65050300	447,553650
5	N 69, 39.040' E 021, 20.369'	21,33947700 69,65067100	451,681702
6	N 69, 39.081' E 021, 20.364'	21,33938700 69,65134400	452,516205

Agisoft workflow

1. Importing the pictures to the software in one chunk. Aligning the cameras with adaptive camera fitting is on.
2. Erasing tie points that have a low likelihood of being in the right place. With the feature ‘gradual selection’ the user can select points based on reconstruction uncertainty (10), re-projection error (0.5) and projection accuracy (8).The tie point cloud was reduced from 1 256 575 points to 250 000 points. Optimize cameras.
3. Importing the GCP coordinates into Agisoft using the WGS84 UTM 33N coordinate system, and cross-referencing them with the GCP markers visible in each picture. The alignment is then optimized based on the GCPs.
4. Building dense cloud, mesh, DEM and orthomosaic.
5. Exporting the dense cloud for use in other applications.

Agisoft PhotoScan

Processing Report

30 October 2018

Survey Data

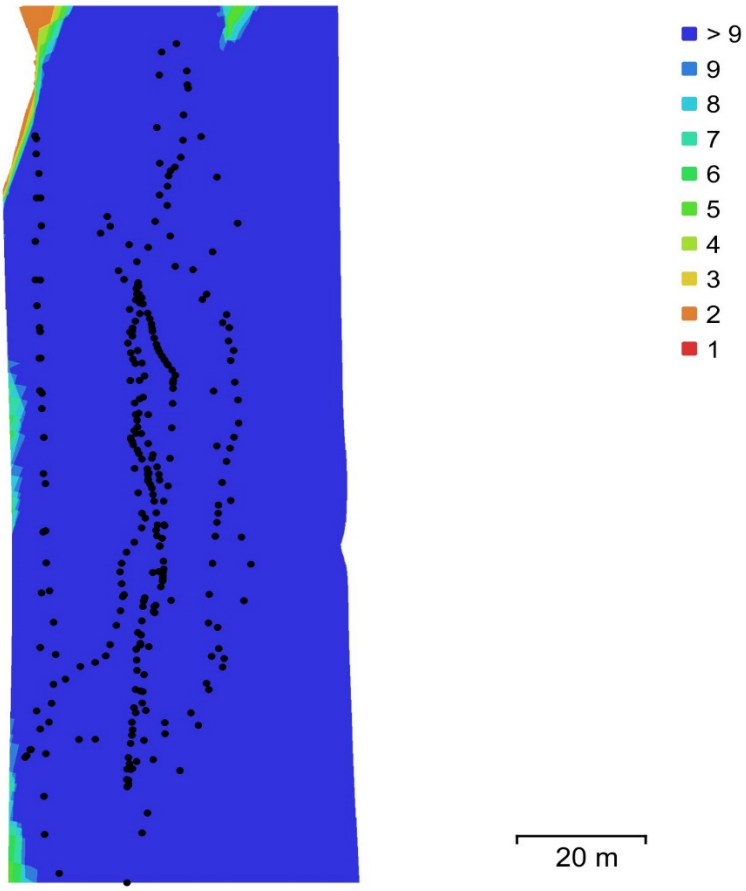

Fig. 1. Camera locations and image overlap.

Number of images:	288	Camera stations:	288
Flying altitude:	23.1 m	Tie points:	258,910
Ground resolution:	9.51 mm/pix	Projections:	1,152,922
Coverage area:	7.7e+03 m²	Reprojection error:	0.725 pix

Camera Model	Resolution	Focal Length	Pixel Size	Precalibrated
FC350 (3.61mm)	4000 x 3000	3.61 mm	1.56 x 1.56 µm	No

Table 1. Cameras.

Camera Calibration

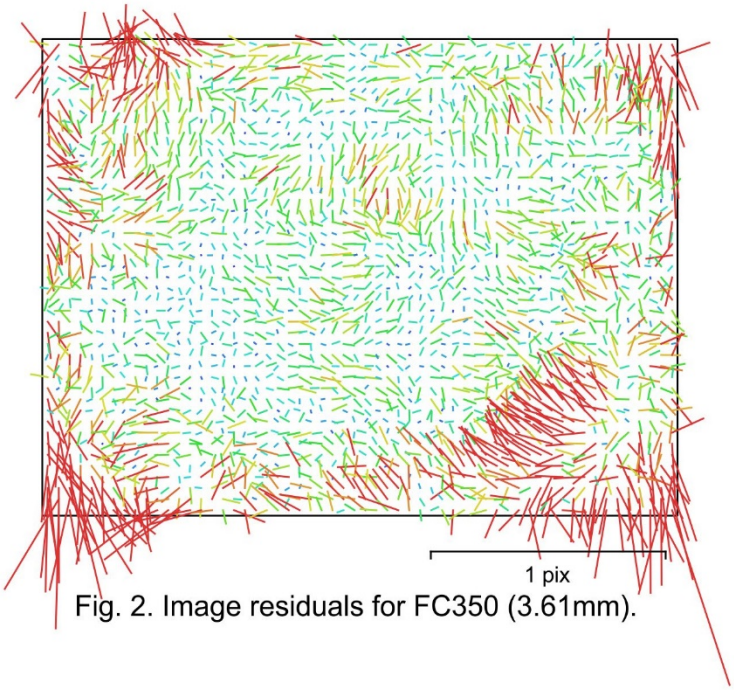

Fig. 2. Image residuals for FC350 (3.61mm).

FC350 (3.61mm)
288 images

Type	Resolution	Focal Length	Pixel Size	
Frame	4000 x 3000	3.61 mm	1.56 x 1.56	µm

	Value	Error	F	Cx	Cy	B1	B2	K1	K2	K3	K4	P1	P2
F	2319.05	0.037	1.00	0.07	-0.11	-0.01	0.01	-0.31	0.29	-0.24	0.23	0.01	-0.28
Cx	26.1936	0.027		1.00	0.06	-0.05	-0.08	-0.01	0.02	-0.02	0.02	0.57	0.02
Cy	-8.24415	0.035			1.00	0.31	-0.01	0.01	-0.01	0.01	-0.02	0.01	0.66
B1	5.26827	0.021				1.00	-0.11	-0.01	-0.01	0.02	-0.02	0.21	0.17
B2	-1.52476	0.018					1.00	0.00	-0.00	-0.00	0.00	-0.22	0.18
K1	-0.13547	5e-05						1.00	-0.97	0.92	-0.87	0.01	0.00
K2	0.128828	0.00017							1.00	-0.99	0.95	0.01	0.00
K3	-0.0427795	0.00024								1.00	-0.99	-0.00	-0.00
K4	0.0128017	0.00011									1.00	0.00	-0.00
P1	0.00025268	3.1e-06										1.00	0.05
P2	-0.000709369	3.3e-06											1.00

Table 2. Calibration coefficients and correlation matrix.

Ground Control Points

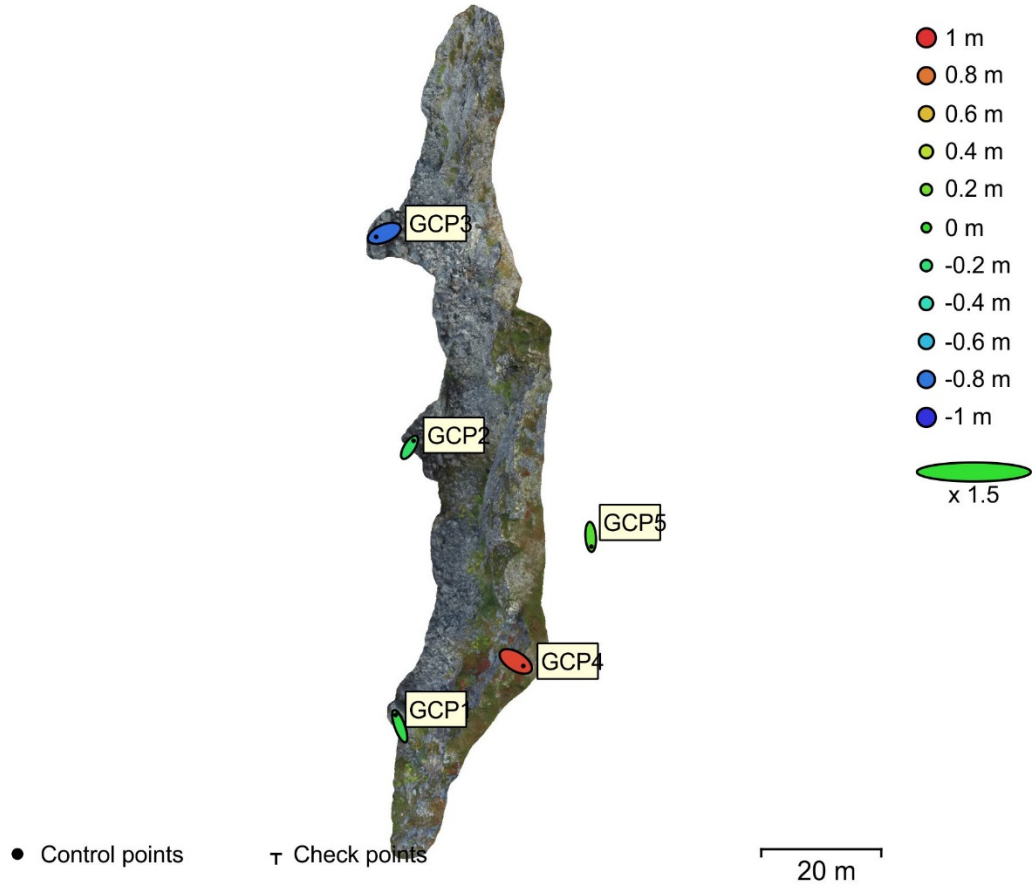

Fig. 3. GCP locations and error estimates.
Z error is represented by ellipse color. X,Y errors are represented by ellipse shape.
Estimated GCP locations are marked with a dot or crossing.

Count	X error (m)	Y error (m)	Z error (m)	XY error (m)	Total (m)
5	1.24731	1.71741	0.570399	2.12256	2.19787

Table 3. Control points RMSE.
X - Easting, Y - Northing, Z - Altitude.

Label	X error (m)	Y error (m)	Z error (m)	Total (m)	Image (pix)
GCP1	-0.911322	2.5033	-0.0698508	2.66494	0.464 (57)
GCP2	0.916574	1.46523	-0.153793	1.73513	0.591 (68)
GCP3	-1.81986	-0.782766	-0.830183	2.14798	0.720 (42)
GCP4	1.66561	-1.0242	0.947486	2.17278	0.849 (61)
GCP5	0.148988	-2.16156	0.106339	2.16929	0.013 (2)
Total	1.24731	1.71741	0.570399	2.19787	0.665

Table 4. Control points.

X - Easting, Y - Northing, Z - Altitude.

Digital Elevation Model

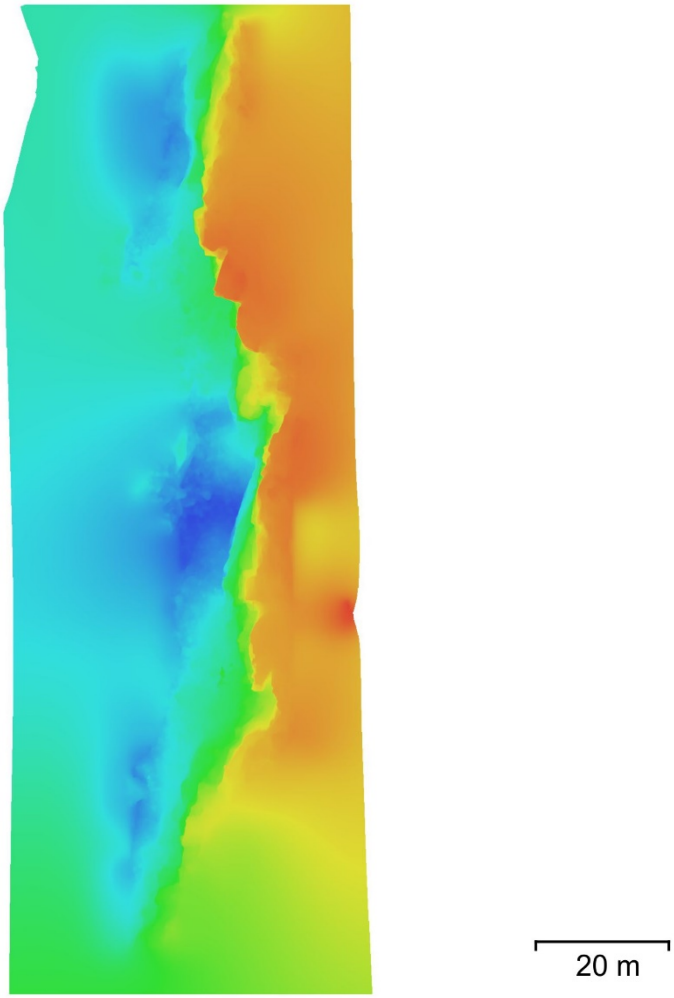

Fig. 4. Reconstructed digital elevation model.

Resolution:	1.9 cm/pix
Point density:	0.277 points/cm²

Processing Parameters

General	
Cameras	288
Aligned cameras	288
Markers	5
Coordinate system	WGS 84 / UTM zone 33N (EPSG::32633)
Rotation angles	Yaw, Pitch, Roll
Point Cloud	
Points	258,910 of 1,447,293
RMS reprojection error	0.219877 (0.724634 pix)
Max reprojection error	3.11953 (14.0158 pix)
Mean key point size	3.28736 pix
Point colors	3 bands, uint8
Key points	No
Average tie point multiplicity	3.7415
Alignment parameters	
Accuracy	High
Generic preselection	Yes
Reference preselection	Yes
Key point limit	60,000
Tie point limit	0
Adaptive camera model fitting	Yes
Matching time	50 minutes 15 seconds
Alignment time	25 minutes 52 seconds
Optimization parameters	
Parameters	f, b1, b2, cx, cy, k1-k4, p1, p2
Adaptive camera model fitting	Yes
Optimization time	32 seconds
Dense Point Cloud	
Points	21,527,475
Point colors	3 bands, uint8
Reconstruction parameters	
Quality	High
Depth filtering	Aggressive
Depth maps generation time	1 days 17 hours
Dense cloud generation time	11 hours 52 minutes
Model	
Faces	4,302,414
Vertices	2,154,066
Vertex colors	3 bands, uint8
Texture	4,096 x 4,096, 4 bands, uint8
Reconstruction parameters	
Surface type	Arbitrary
Source data	Dense
Interpolation	Enabled
Quality	High
Depth filtering	Aggressive
Face count	4,305,495
Processing time	3 hours 51 minutes
Texturing parameters	
Mapping mode	Generic
Blending mode	Mosaic
Texture size	4,096 x 4,096
Enable hole filling	Yes
Enable ghosting filter	Yes
UV mapping time	1 minutes 5 seconds

Blending time	17 minutes 18 seconds
DEM	
Size	3,421 x 8,732
Coordinate system	WGS 84 / UTM zone 33N (EPSG::32633)
Reconstruction parameters	
Source data	Dense cloud
Interpolation	Enabled
Processing time	49 seconds
Software	
Version	1.4.4 build 6848
Platform	Windows 64

D. Structural data

Foliation and fold axes

Mellomfjellet 1

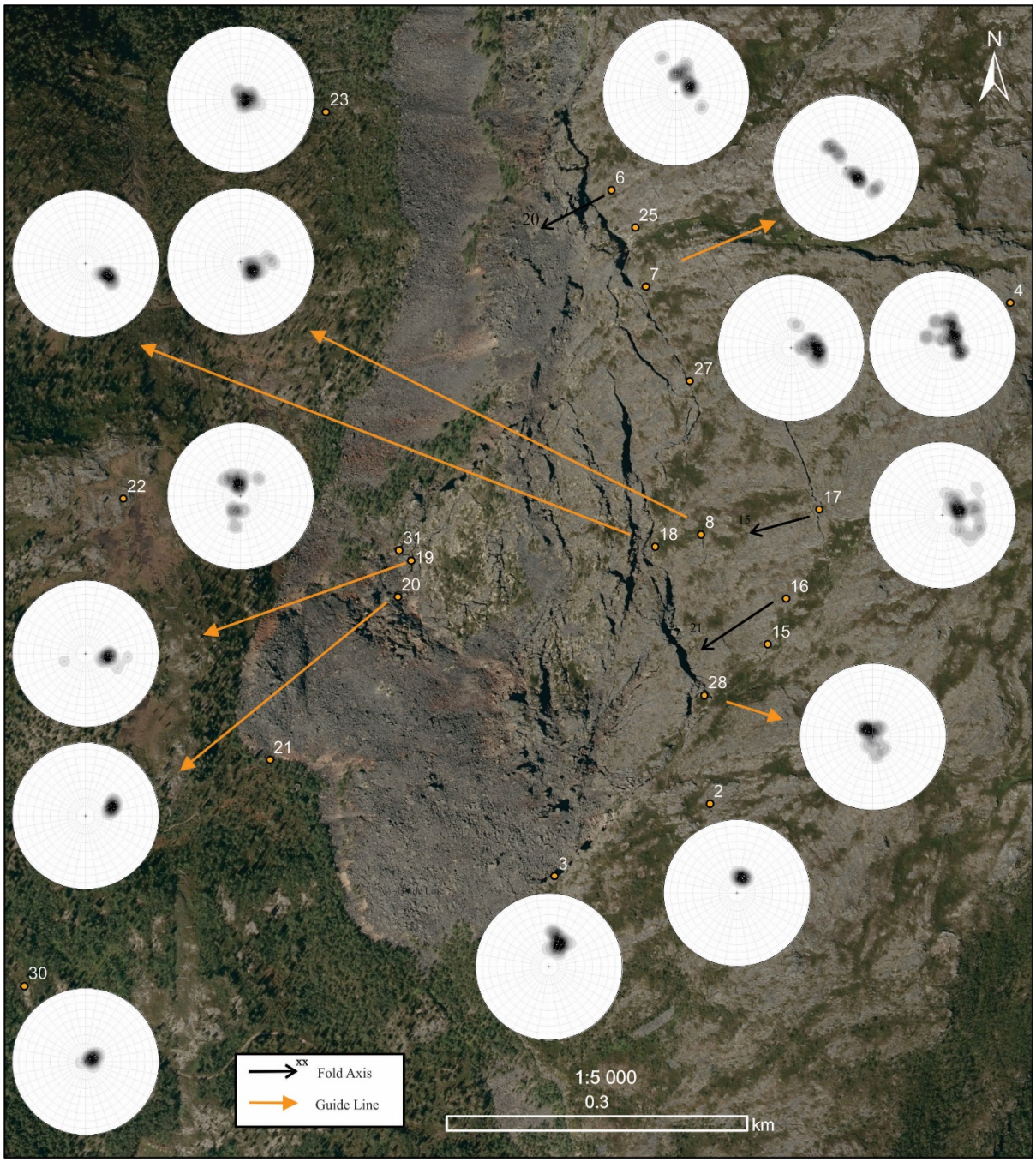

Mellomfjellet 2

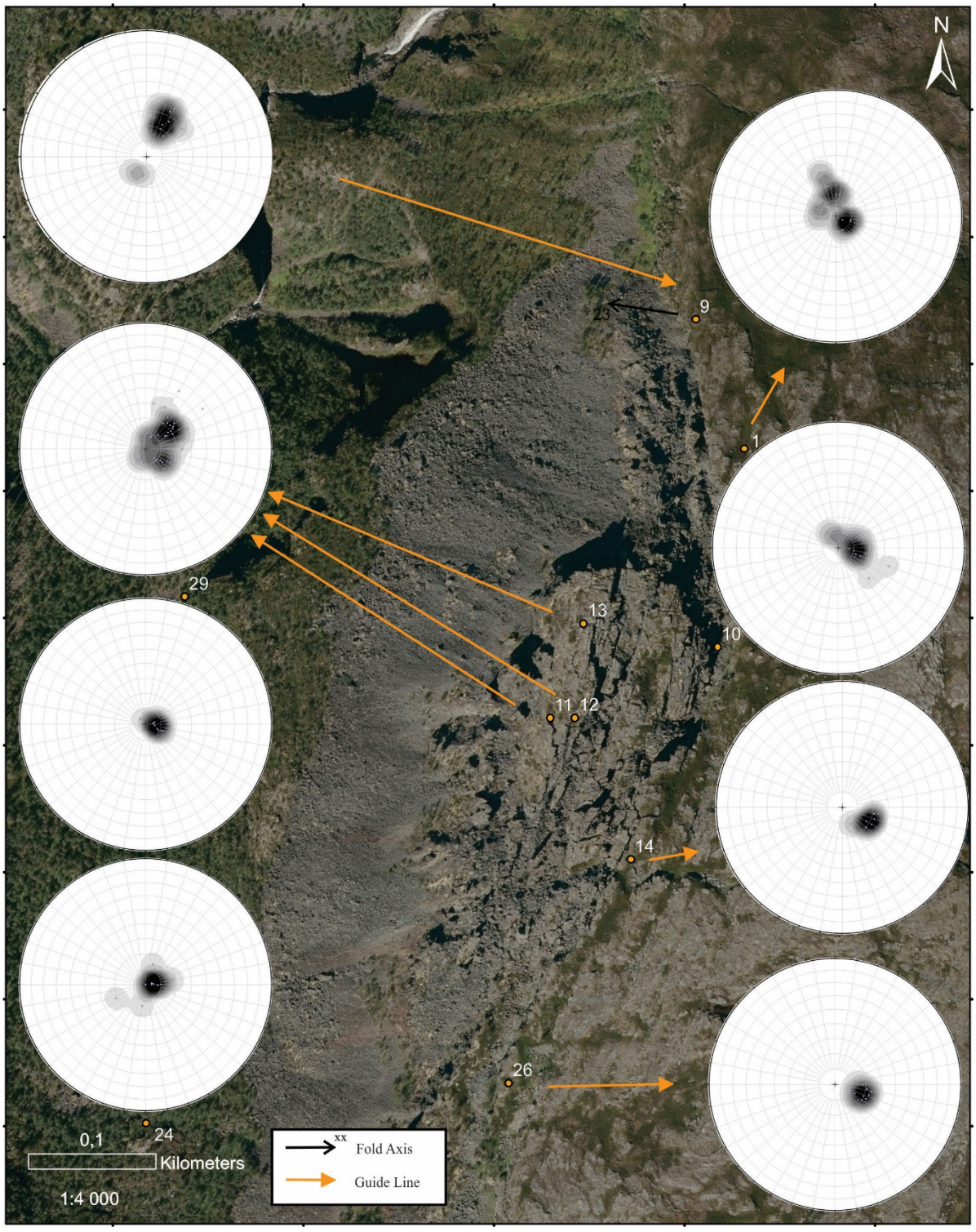

Joints

Mellomfjellet 1

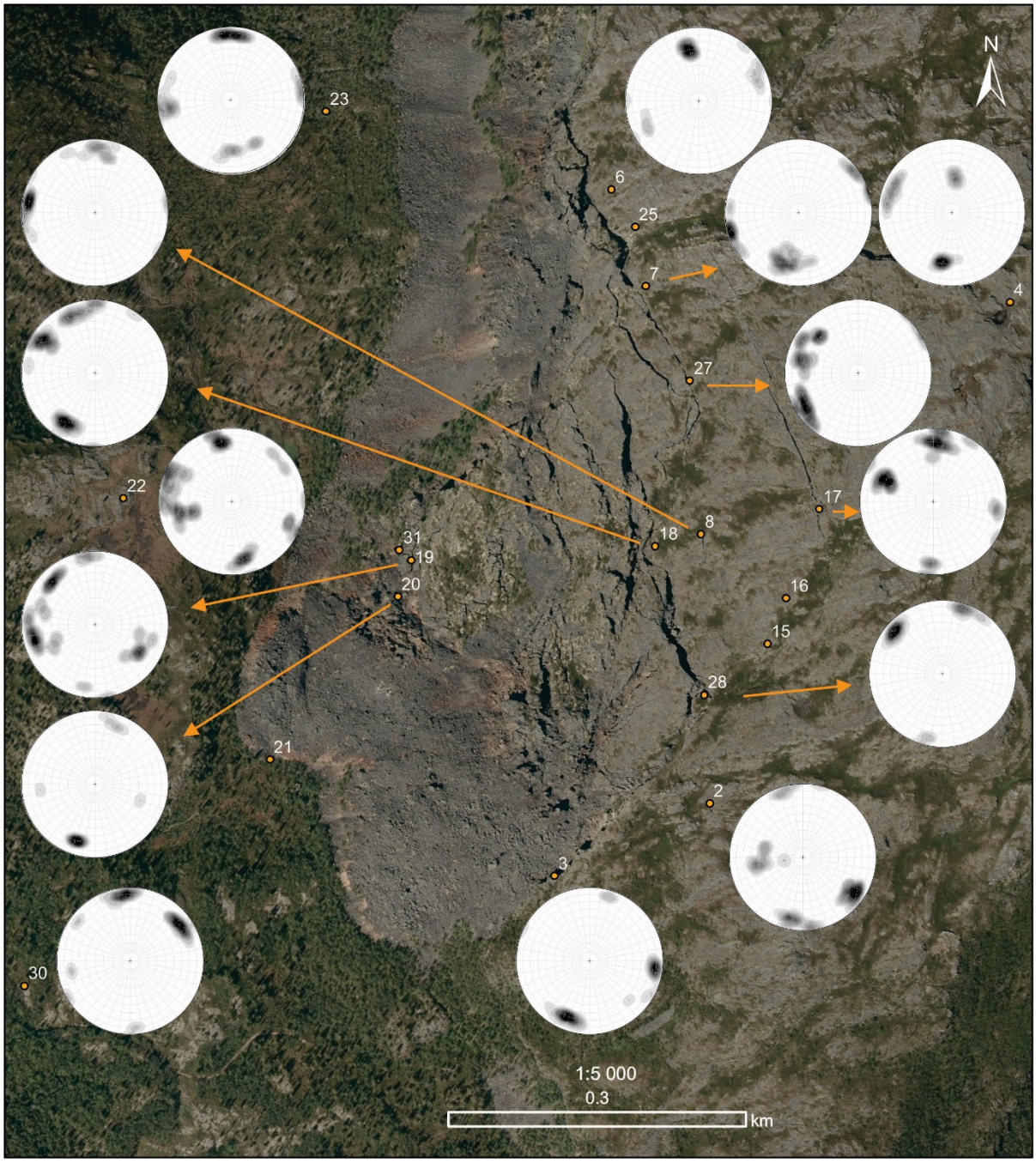

Mellomfjellet 2

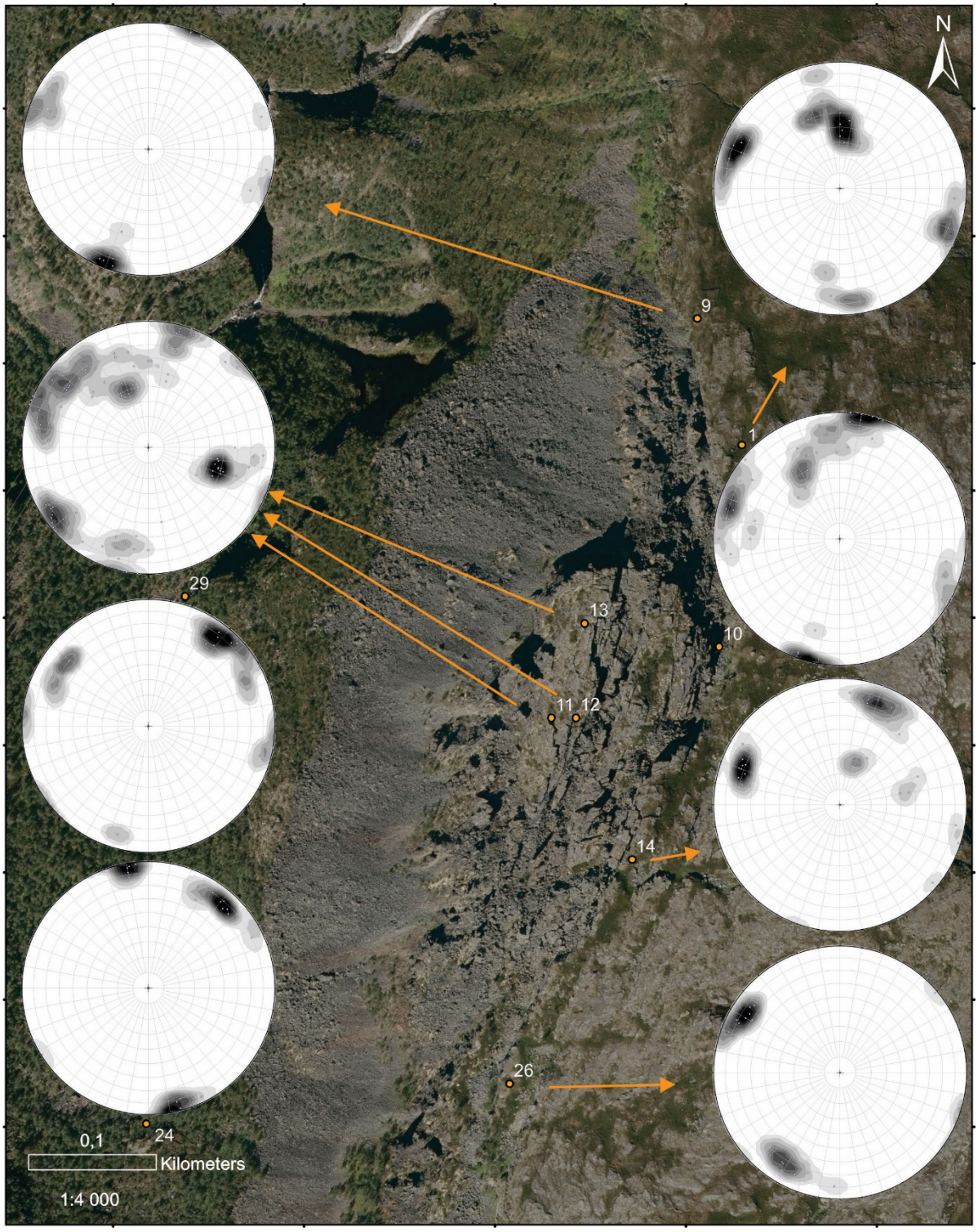

E. Failure scenarios

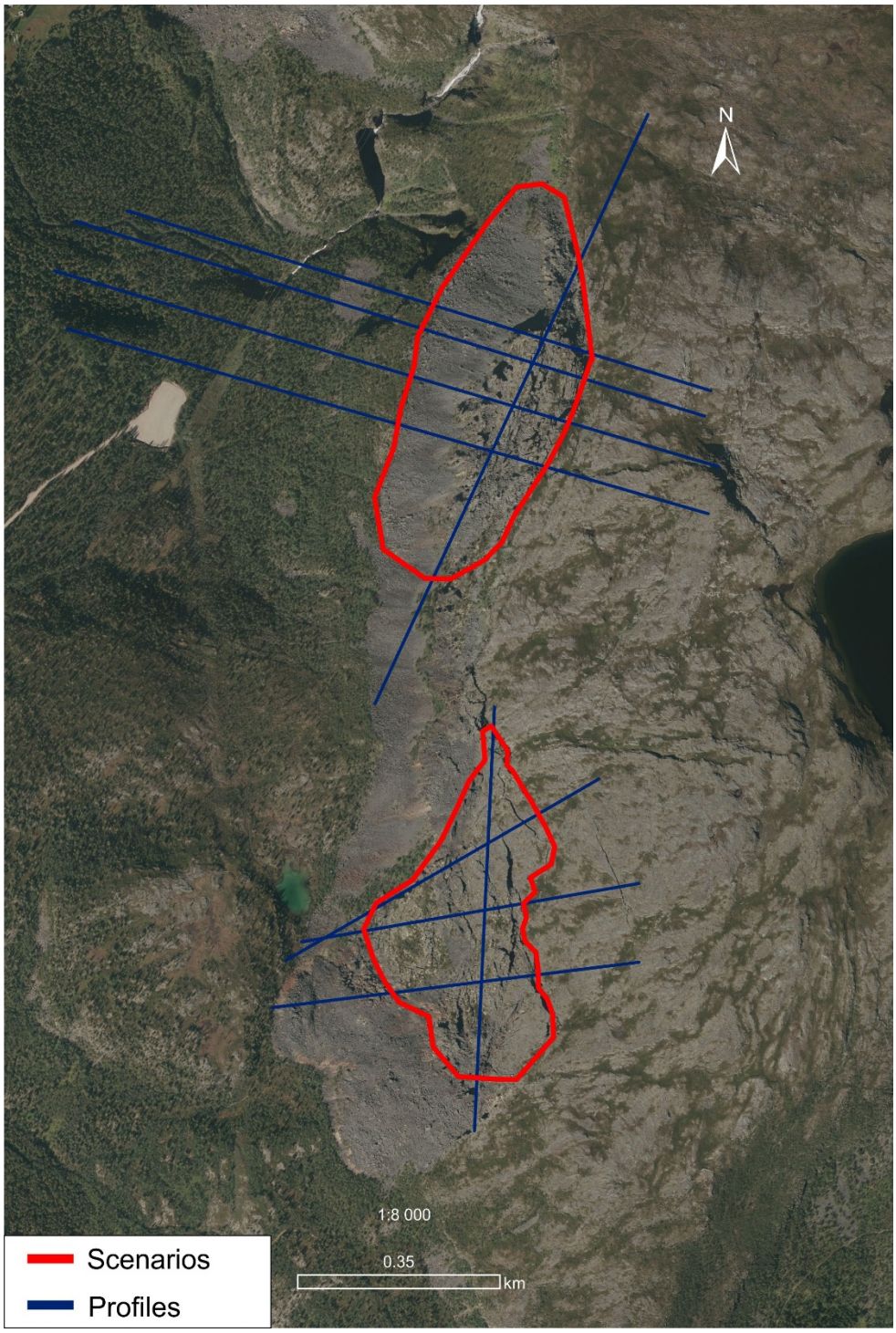

F. Hazard analysis

Hazard analysis of unstable rock slopes in Norway

Locality name: Mellomfjellet **Scenario:** Mellomfjellet 1 **Executed by:** Bernt Kristian Vik **Date:** 20.03.2019

Hazard class	Probabiliy	Cumulated prob.
Meget lav	0.0 %	0.0 %
Lav	0.0 %	0.0 %
Middels	100.0 %	100.0 %
Høy	0.0 %	100.0 %
Meget høy	0.0 %	100.0 %

Hazard score	
Mimimum	5.0
Maximum	6.0
Modus	5.0
Average	5.3
5% percentile	5.0
95% percentile	6.0

1.Back-scarp	**Points**	**Norm. prob.**
Not developped	0	0.0 %
Partly open over width of slide body (few cm to m)	0.5	75.0 %
Fully open over width of slide body (few cm to m)	1	25.0 %
Comment: Discontinous back-scarp. In between the offsets depressions might indicate a developed back-scarp.		

2. Potential gliding surfaces	**Points**	**Norm. prob.**
No penetrative structures dip out of the slope	0	0.0 %
Penetrative structures dip on average < 20 degree or steeper than the slope	0.5	66.7 %
Penetrative structures dip on average > 20 degree and daylight with the slope	1	33.3 %
Comment: The average foliation is below 20 degrees. However, many of the foliation measurements are over 20 degrees and the measured fold axes are plunging up to 23 degrees downslope. Uncertainty is here added for the possibility of sliding on foliation and fold axes.		

3. Flanks	**Points**	**Norm. prob.**
Not developped	0	0.0 %
Partly developped on 1 side	0.25	0.0 %
Fully developped or free slope on 1 side or partly developped on 2 sides	0.5	0.0 %
Fully developped or free slope on 1 side and partly developped on 1 side	0.75	0.0 %
Fully developped or free slope on 2 sides	1	100.0 %
Comment: Open flanks on both sides of the unstable area.		

4. Kinematic analysis	**Points**	**Norm. prob.**
Kinematic feasibility test does not allow for planar sliding, wedge sliding or toppling	0	0.0 %
Failure is partly feasible kinematically (movement direction is more than ±30° to slope orientation)	0.5	0.0 %
Failure is feasible kinematically (movement direction is less than ±30° to slope orientation)	0.75	0.0 %
Failure is partly feasible kinematically on persistent discontinuities (movement direction is more than ±30° to slope orientation)	0.75	0.0 %
Failure is feasible kinematically on persistent discontinuities (movement direction is less than ±30° to slope orientation)	1	100.0 %
Comment: Planar sliding is relevant since it is within the lateral limits of the failure. The foliation willl then be the sliding plane for the failure mechainsm. The average foliation is not steep enough, but many of the foliation measurements are steep enough for failure. Some of the fold axes are steep enough for sliding to happen along the folded foliation.		

5. Morphological features indicating failure surface	**Points**	**Norm. prob.**
No indication on slope morphology	0	100.0 %
Slope morphology suggests formation of a rupture surface (bulging, concavity-convexity, springs)	0.5	0.0 %
Continuous rupture surface is suggested by slope morphology and can be mapped out	1	0.0 %
Comment: No observation of morphological features indicating a failure plane. Assumptions of a failure plane below the deposits are present, but it is not observed.		

6. Displacement	**Points**	**Norm. prob.**
No significant movement	0	0.0 %
>0 - 0.5 cm/year	1	100.0 %
0.5 - 1 cm/year	2	0.0 %
1 - 4 cm/year	3	0.0 %
4 - 10 cm/year	4	0.0 %
> 10 cm/year	5	0.0 %
Comment: Up to 6 mm/year observed in the RSAT2 data.		

7. Acceleration (if displacement is >0.5 cm/year and <10 cm/year)	**Points**	**Norm. prob.**
No acceleration or change in displacement rates	0	80.0 %
Increase in displacement rates	1	20.0 %
Comment: Too few data to find an possible acceleration.		

8. Increase of rock-fall activity	**Points**	**Norm. prob.**
No increase of rock fall activity	0	0.0 %
Increase of rock fall activity	1	100.0 %
Comment: Too few data to state increase.		

9. Previous landslides	**Points**	**Norm. prob.**
No post-glacial events of similar size	0	100.0 %
One or several events older than 5000 years of similar size	0.5	0.0 %
One or several events younger than 5000 years of similar size	1	0.0 %
Comment: No previous scenarios of same size.		

Hazard analysis of unstable rock slopes in Norway

Locality name: Mellomfjellet **Scenario:** Mellomfjellet 2 **Executed by:** Bernt Kristian Vik **Date:** 20.03.2019

Hazard class	Probabiliy	Cumulated prob.
Very low	0.0 %	0.0 %
Low	0.0 %	0.0 %
Medium	100.0 %	100.0 %
High	0.0 %	100.0 %
Very high	0.0 %	100.0 %

Hazard score	
Mimimum	5.5
Maximum	6.0
Modus	5.5
Average	5.6
5% percentile	5.5
95% percentile	6.0

1.Back-scarp	**Points**	**Norm. prob.**
Not developped	0	0.0 %
Partly open over width of slide body (few cm to m)	0.5	75.0 %
Fully open over width of slide body (few cm to m)	1	25.0 %
Comment: Fully developed back-scarp.		

2. Potential gliding surfaces	**Points**	**Norm. prob.**
No penetrative structures dip out of the slope	0	0.0 %
Penetrative structures dip on average < 20 degree or steeper than the slope	0.5	66.7 %
Penetrative structures dip on average > 20 degree and daylight with the slope	1	33.3 %
Comment: Foliation and fold axes might be potential gliding surfaces. Average foliation dips less than 20		

3. Flanks	**Points**	**Norm. prob.**
Not developped	0	0.0 %
Partly developped on 1 side	0.25	0.0 %
Fully developped or free slope on 1 side or partly developped on 2 sides	0.5	0.0 %
Fully developped or free slope on 1 side and partly developped on 1 side	0.75	0.0 %
Fully developped or free slope on 2 sides	1	100.0 %
Comment: Well developed.		

4. Kinematic analysis	**Points**	**Norm. prob.**
Kinematic feasibility test does not allow for planar sliding, wedge sliding or toppling	0	0.0 %
Failure is partly feasible kinematically (movement direction is more than ±30° to slope orientation)	0.5	0.0 %
Failure is feasible kinematically (movement direction is less than ±30° to slope orientation)	0.75	0.0 %
Failure is partly feasible kinematically on persistent discontinuities (movement direction is more than ±30° to slope orientation)	0.75	0.0 %
Failure is feasible kinematically on persistent discontinuities (movement direction is less than ±30° to slope orientation)	1	100.0 %
Comment: Toppling is feasbile with J1 is located in the critical area for flexural toppling at MF2. The foliation is a feasible failure mechanism as well.		

5. Morphological features indicating failure surface	**Points**	**Norm. prob.**
No indication on slope morphology	0	100.0 %
Slope morphology suggests formation of a rupture surface (bulging, concavity-convexity, springs)	0.5	0.0 %
Continuous rupture surface is suggested by slope morphology and can be mapped out	1	0.0 %
Comment: No sign of a failure surface in the morphology. Only assumptions.		

6. Displacement	**Points**	**Norm. prob.**
No significant movement	0	0.0 %
>0 - 0.5 cm/year	1	100.0 %
0.5 - 1 cm/year	2	0.0 %
1 - 4 cm/year	3	0.0 %
4 - 10 cm/year	4	0.0 %
> 10 cm/year	5	0.0 %
Comment: Displacement is up to 3 mm/year.		

7. Acceleration (if displacement is >0.5 cm/year and <10 cm/year)	**Points**	**Norm. prob.**
No acceleration or change in displacement rates	0	80.0 %
Increase in displacement rates	1	20.0 %
Comment: Not observed		

8. Increase of rock-fall activity	**Points**	**Norm. prob.**
No increase of rock fall activity	0	0.0 %
Increase of rock fall activity	1	100.0 %
Comment: Not observed		

9. Previous landslides	**Points**	**Norm. prob.**
No post-glacial events of similar size	0	100.0 %
One or several events older than 5000 years of similar size	0.5	0.0 %
One or several events younger than 5000 years of similar size	1	0.0 %
Comment: Not observed		

G.Field guide

NZ GEOTECHNICAL SOCIETY INC

ROCK > field guide sheet

FIELD DESCRIPTION OF ROCK

SEQUENCE OF TERMS – weathering – colour – fabric – rock name – strength – discontinuities – additional

SCALE OF ROCK MASS WEATHERING

Term	Grade	Abbreviation	Description
Unweathered (fresh rock)	I	UW	Rock mass shows no loss of strength, discolouration or other effects due to weathering. There may be slight discolouration on major rock mass defect surfaces or on clasts.
Slightly Weathered	II	SW	The rock mass is not significantly weaker than when fresh. Rock may be discoloured along defects, some of which may have been opened slightly.
Moderately Weathered	III	MW	The rock mass is significantly weaker than the fresh rock and part of the rock mass may have been changed to a soil. Rock material may be discoloured and defect and clast surfaces will have a greater discolouration, which also penetrates slightly into the rock material. Increase in density of defects due to physical disintegration.
Highly Weathered	IV	HW	Most of the original rock mass strength is lost. Material is discoloured and more than half the mass is changed to a soil by chemical decomposition or disintegration (increase in density of defects/fractures). Decomposition adjacent to defects and at the surface of clasts penetrates deeply into the rock material. Lithorelicts or corestones of unweathered or slightly weathered rock may be present.
Completely Weathered	V	CW	Original rock strength is lost and the rock mass changed to a soil either by decomposition (with some rock fabric preserved) or by physical disintegration.
Residual Soil	VI	RS	Rock is completely changed to a soil with the original fabric destroyed (pedological soil).

ROCK STRENGTH TERMS

Term	Field Identification of Specimen	Unconfined uniaxial compressive strength q_u (MPa)	Point load strength $I_{s(50)}$ (MPa)
Extremely strong	Can only be chipped with geological hammer	> 250	>10
Very strong	Requires many blows of geological hammer to break it	100 – 250	5 – 10
Strong	Requires more than one blow of geological hammer to fracture it	50 – 100	2 – 5
Moderately strong	Cannot be scraped or peeled with a pocket knife. Can be fractured with single firm blow of geological hammer	20 – 50	1 – 2
Weak	Can be peeled by a pocket knife with difficulty. Shallow indentations made by firm blow with point of geological hammer	5 – 20	<1
Very weak	Crumbles under firm blows with point of geological hammer. Can be peeled by a pocket knife	1 – 5	
Extremely weak (soil description required)	Indented by thumb nail or other lesser strength terms used for soils	<1	

Note: • No correlation is implied between q_u and $I_{s(50)}$

SPACING OF DEFECTS/ DISCONTINUITIES

Term	Spacing
Very widely spaced	>2 m
Widely spaced	600 mm – 2 m
Moderately widely spaced	200 mm – 600 mm
Closely spaced	60 mm – 200 mm
Very closely spaced	20 mm – 60 mm
Extremely closely spaced	<20 mm

APERTURE OF DISCONTINUITY SURFACES

Term	Aperture (mm)	Description
Tight	Nil	Closed
Very Narrow	> 0 – 2	
Narrow	2 – 6	
Moderately Narrow	6 – 20	Gapped
Moderately Wide	20 – 60	Open
Wide	60 – 200	
Very Wide	> 200	

BEDDING THICKNESS TERMS

Term	Bed Thickness
Thinly laminated	< 2 mm
Laminated	2 mm - 6 mm
Very thin	6 mm - 20 mm
Thin	20 mm - 60 mm
Moderately thin	60 mm - 200 mm
Moderately thick	0.2 m - 0.6 m
Thick	0.6 m - 2 m
Very thick	> 2 m

BEDDING INCLINATION TERMS

Term	Inclination (from horizontal)
Sub-horizontal	0° – 5°
Gently inclined	6° – 15°
Moderately inclined	16° – 30°
Steeply inclined	31° – 60°
Very steeply inclined	61° – 80°
Sub-vertical	81° – 90°

ROUGHNESS AND APERTURE

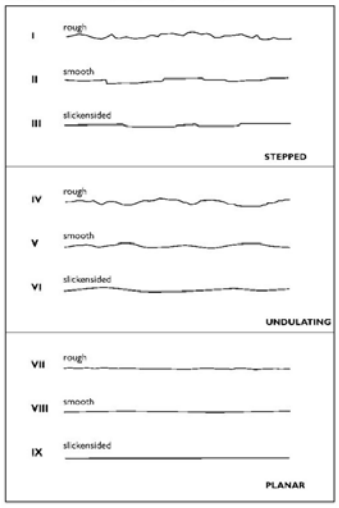

compiled by KATE WILLIAMS design KARRYN MUSCHAMP

NZ GEOTECHNICAL SOCIETY INC

This field sheet has been taken from and should be used and read with reference to the document FIELD DESCRIPTION OF SOIL AND ROCK. Guideline For the Field Classification and Description of Soil and Rock for Engineering Purposes. NZ Geotechnical Society Inc, December 2005. **www.nzgeotechsoc.org.nz**

New Zealand Geotechnical Society Inc field guide Sheet (NZGS, 2005).